VOLUME 5 NUMBER 2 2018 ISSN 2409-6121; eISSN 2522-1361

Physical Sciences and Technology

National Nanotechnological Laboratory of Open Type
Institute of Experimental and Theoretical Physics

Physical Sciences and Technology is publishing two number in a year by al-Farabi Kazakh National University, al-Farabi ave., 71, 050040, Almaty, the Republic of Kazakhstan
website: http://phst.kaznu.kz/

Any inquiry for subscriptions should be send to:
Gauhar Mussabek, al-Farabi Kazakh National University
al-Farabi ave., 71, 050040, Almaty, the Republic of Kazakhstan
e-mail: gauharmussabek@gmail.com

SCOPE AND AIM

Physical Sciences and Technology provides an original paperback for the publication of peerreviewed research and review articles in all fields of Physics and related Technology. The topics, included in the scope, especially emphasize understanding of the physics underlying modern technology.

Subject areas may include, but are not limited to the following fields: Astronomy and Space Research, Theoretical Physics and Astrophysics, Plasma Physics and Related Technology, Chemical Physics and Related Technology, Condensed Matter Physics and Related Technology, Thermal physics and Related Technology, Nuclear Physics and Related Technology, Nanomaterials and Nanotechnology, Applied Atomic and Molecular Physics, Material Sciences and Related Technology, Electronics and Related Technology, Instrumentation, Photonics and Quantum Electronics, Signal processing.

The Journal is issued under the auspices of the National Nanotechnological Laboratory of Open Type and Institute of Experimental and Theoretical Physics and is published two times a year by the «Kazakh University» Publishing House. The International Editorial Board of the Journal consists of leading researchers from different countries of the world. The Journal is wide open for contributions that both lie at the far frontiers of contemporary physics and are particularly aimed at applications of the scientific principles of physics to modern technological problems.

IRSTI 29.27.51

Etching characteristics of diamond-like carbon in fluorocarbon plasmas

K. Takahashi[1,*] and R. Takahashi[2]

[1]*Faculty of Electrical Engineering and Electronics,*
Kyoto Institute of Technology, Matsugasaki, Sakyo-ku, Kyoto 606-8585, Japan
[2]*Department of Electronics and Information Science,*
Kyoto Institute of Technology, Matsugasaki, Sakyo-ku, Kyoto 606-8585, Japan
[*]*e-mail: takahash@kit.jp*

Diamond-like carbon (DLC) is one of the promising materials with biocompatibility. Applications for medical coating, biochip, and so on, have been widely expected in this decade. Fabrication process of biochips such as etching and removing requires patterning of the DLC to give surface of the chips functions for medical diagnostics. The present study reports etching characteristics of the DLC in fluorocarbon plasmas, comparing with those of Si and SiO_2. In the plasmas, F radical was found to be an etchant for the DLC, the same as etching of Si and SiO_2. The O radical is well known to be so reactive on the DLC. The O_2-addition to the plasmas was obviously effective in the DLC etching, and making balance of the radicals of F and O, resulting in changing etch rate of the DLC and morphology of surface. The etch rate could be controlled in changing gas flow rate of CF_4 to O_2 with Ar dilution. The morphology, which is indispensable to determine the characteristics on the surface of the biochip and so on, showed that fluorine-content plasmas suppressed roughness compared with pure-O_2 plasmas.

Key words: Diamond-like carbon, plasma etching, fluorocarbon, plasma.
PACS numbers: 52.77.-j, 52.77.Bn, 81.05.U-, 81.65.Cf

1 Introduction

Diamond-like carbon (DLC) has been focused attention on in many technological fields. The properties of electron emission, low friction, wear resistance, high hardness, chemical stability, and biocompatibility make it useful for applications of hard coating, semiconductor process, micro-electro-mechanical system, microfluidic channel, surgical implant, food, beverage, and so on [1-4]. Transparent glass and plastics have been commonly used as substrate materials of chemical/biochemical analysis chips since light is used for detection and observation of samples [5]. The DLC is one of the promising materials for the chips since it gives its excellent properties to surfaces of the glass and plastics substrates [6, 7]. In use of the DLC for the chips, patterning and removal processes are required to fabricate highly functional bio-analysis systems. Plasma etching can be widely used for the processes [8]. The DLC and its related materials are usually etched in oxygen- and hydrogen-content plasmas [9-11]. This paper presents results of the etching of DLC thin films on Si substrates in inductively coupled fluorocarbon plasmas. Then we discuss performance of fluorocarbon plasmas in etching of the DLC, and try to understand etching mechanism by comparing with those of Si and SiO_2 well known in previous works [12-15].

2 Experimental

Samples for etching were 1000-nm-thick DLC films on Si substrates prepared by chemical vapor deposition (CVD), SiO_2 films formed by thermal oxidation, and bare Si. The samples were cleaved into 2 cm^2 pieces and attached on 2-inch-diameter Si wafer, which was then clamped on to a wafer stage. Etching experiments were performed in a low-pressure inductively coupled plasma (ICP) reactor supplied with 13.56-MHz powers [16, 17]. An rf power supply was coupled to plasmas via three-turn planar rf induction coil of 15 cm in outer diameter, positioned on the quartz window located at the top of the reactor. The distance from the bottom edge of the rf coupling window to a wafer stage was 5 cm. Gas-

mixtures of CF_4, O_2, and Ar were introduced into the reactor evacuated to a base pressure $< 4\times10^{-4}$ Pa, and gas pressure was typically maintained at 3 Pa. The total gas flow rate was 40 sccm (sccm denotes cubic centimeter per minute at the standard conditions). The discharge was established at a nominal rf power of 300 W, corresponding to net powers to the π-type matching circuit driving the induction coil. The wafer stage was capacitively coupled to another 13.56-MHz rf power supply for additional biasing; the rf bias power was varied between 0 and 20 W (net power), resulting in a dc self-bias voltage on the stage down to -100 V. In etching, the samples were partly covered with thin glass plates as masks and exposed to the plasmas for several minutes. A step appeared on a boundary between a part etched by the plasmas and the other covered with the plate. Etch depth was determined to be height of the step measured by stylus profilometry. The chemical composition of carbon, fluorine and oxygen was analyzed by x-ray photoelectron spectroscopy (XPS) using Mg *Kα* x-ray radiation with a pass energy of 50 eV at a takeo□ angle of 90°. The contents of carbon, fluorine, and oxygen were detected with assigning peaks of C_{1s}, F_{1s}, and O_{1s}, respectively. The atomic force microscopy (AFM) was employed with a tapping mode to observe surfaces of the samples and record their morphologies.

3 Results and Discussion

Figure 1 shows etch rates of the DLC, Si, and SiO_2 as functions of the gas-mixture ratio, $[CF_4]/([CF_4]+[Ar])$ with self-bias voltage constant at -100 V in CF_4/Ar plasmas. In fluorocarbon plasmas, F radical is a dominant etchant for Si and SiO_2.[12] Furthermore, CF_x radicals work effectively in etching of SiO_2 [13–15]. In Figure 1, the etch rate of Si has the same tendency as that of SiO_2. Therefore, the F radical is a main product in the CF_4/Ar plasmas. The etch rate of the DLC has the same tendency as those of Si and SiO_2, and is lower than other samples. This means that the F radical indeed etches the DLC, but it is not so effective as for Si and SiO_2.

XPS spectra of C_{1s}, F_{1s} and O_{1s} signals on surfaces of the DLC samples are shown in Figure 2. The contents of C and F were increased on the surfaces with increasing the gas-mixture ratio of $[CF_4]/([CF_4]+[Ar])$. In the regime of the ratio greater than 0.2 where the etch rate of the DLC decreased monotonically, chemical bond components of $C–CF_x$ and CF were detected at 287.3 and 289.5 eV and intensity of those signals increased with increasing the ratio [18]. This indicated that the surfaces of the DLC were fluorinated, i.e., terminated by fluorine in the plasmas. Conversely, the pre-etched sample and surface of sputter-etched by a pure-Ar plasma were oxidized. Dangling bonds produced in CVD and sputter-etching combined with ambient oxygen. In the CF_4/Ar plasmas, the F radical works as an etchant of the DLC and terminates the dangling bonds produced in etching on the surface.

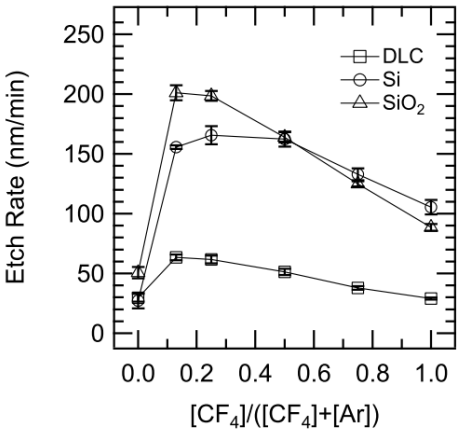

Figure 1 – Etch rate of the DLC in the CF_4/Ar plasmas plotted with those of Si and SiO_2 as a function of the gas-mixture ratio of $[CF_4]/([CF_4]+[Ar])$. The self-bias voltage was constant at –100 V. Error bars indicate variability in reproducing the experiments of etching and measuring the steps on the samples by stylus profilometry

Figure 3 shows etch rates of the DLC in CF_4/O_2 plasmas with self-bias voltage constant at -100 V. The rates increased drastically with increasing O_2 content from 0 to 0.125 of the gas-mixture ratio. Then the rates decreased drastically with the ratio varied to 0.875. In a pure-O_2 plasma, the sample of the DLC was etched at the highest rate of 120 nm/min. In the regime of small content of O_2 less than 0.2, the samples of Si and SiO_2 were etched by F radical produced in possible reaction, $CF_4 + O_2 \rightarrow 4F + CO_2$.[19] Here the F radical also contributed to etch the sample of the DLC.

In Figure 4, the XPS spectra on surfaces of the DLC etched in the plasmas are shown. Increasing the gas-mixture ratio of $[O_2]/([CF_4]+[O_2])$, intensity of the F_{1s} peak decreased and that of the O_{1s} peak was enhanced. Adding O_2 much more than 0.2 in the CF_4/O_2 plasmas, etching reaction on surfaces was suppressed, although fluorine content reached the surfaces. On the surfaces, C–O bond tends to be formed and stable rather than C–F, since energy of

the C–O, 1076 kJ/mole is much higher than that of the C–F, 547 kJ/mole [20]. Moreover oxygen added to the plasmas did not result in etching of the DLC. This means that O radical is scavenged in a reaction before reaching surfaces, $CF_4 + O_2 \rightarrow COF_2 + 2F + O$.[21]

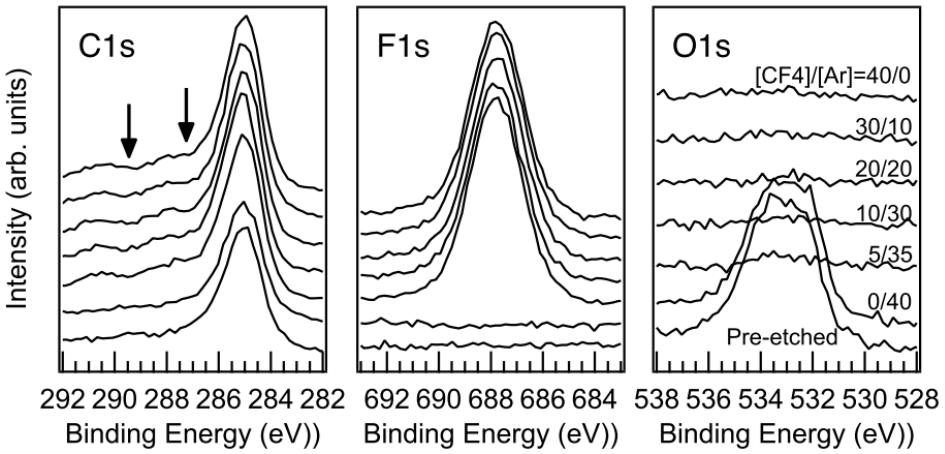

Figure 2 – XPS spectra of C_{1s}, F_{1s} and O_{1s} on surfaces of the DLC samples etched in the CF_4/Ar plasmas, and on that of a pre-etched one. The experimental conditions were the same as in Figure 1. Arrows show signals from chemical bond components of C–CF_x at 287.3 and CF at 289.5 eV

The surfaces etched in pure-CF_4, Ar and O_2 plasmas were observed by AFM (Figure 5). Values of root mean square (RMS) indicating roughnesses on the surfaces was calculated from morphologies in the AFM images. The RMSs in the pure-CF_4, Ar and O_2 were 0.084, 0.094 and 1.7 nm, respectively. Conversely, the etch rates of the plasmas were 29, 30 and 120 nm/min. The higher etch rate gets the rougher surface. For fabrication and removing processes of the DLC, it is expected to get appropriate etch rate and roughness on the surface. The results mentioned above implies that processes require etching to use gas- mixture of CF_4, O_2 and Ar in order to control the morphologies on the surfaces as well as the etch rates. Samples of the DLC were etched in changing gas-mixture ratio of $[CF_4]/[O_2]$ with Ar dilution of 30 sccm (Figure 6). The total flow rate was constant at 40 sccm. Etch rates of Si and SiO_2 decreased with decreasing the flow rate of CF_4 i.e., increasing that of O_2. Etch rate of the DLC was enhanced with increasing the flow rate of O_2. The more content of O_2 gets the more reactive etching on surface of the DLC samples. It notes that roughness on the surface is expected to be also enhanced with increasing the content of O_2 according to the AFM images (Figure 5).

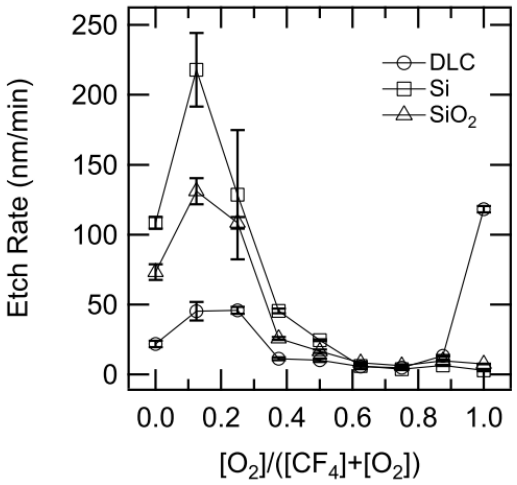

Figure 3 – Etch rate of the DLC in the CF_4/O_2 plasmas plotted with those of Si and SiO_2 as a function of the gas-mixture ratio of $[O_2]/([CF_4]+[O_2])$. The self-bias voltage was constant at 100V. The error bars are treated as in Figure 1

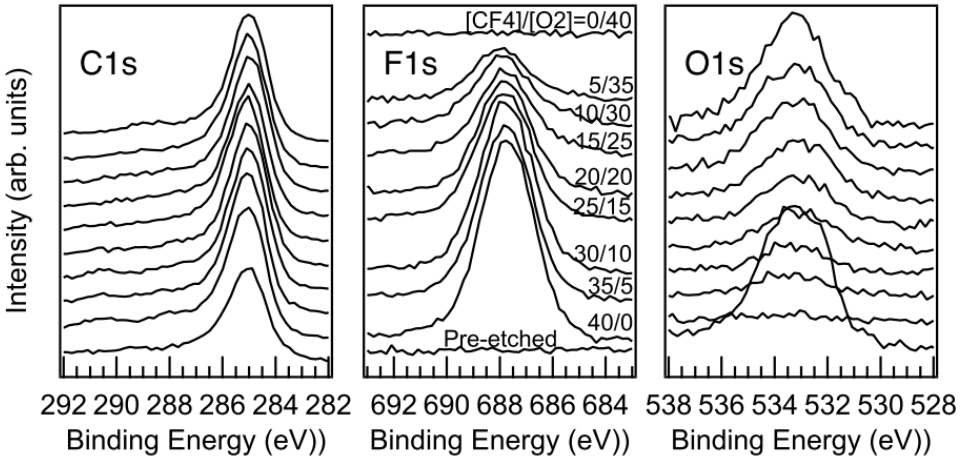

Figure 4 – XPS spectra of C_{1s}, F_{1s} and O_{1s} on surfaces of the DLC samples etched in the CF_4/O_2 plasmas, and on that of a pre-etched one. The experimental conditions were the same as in Figure 3

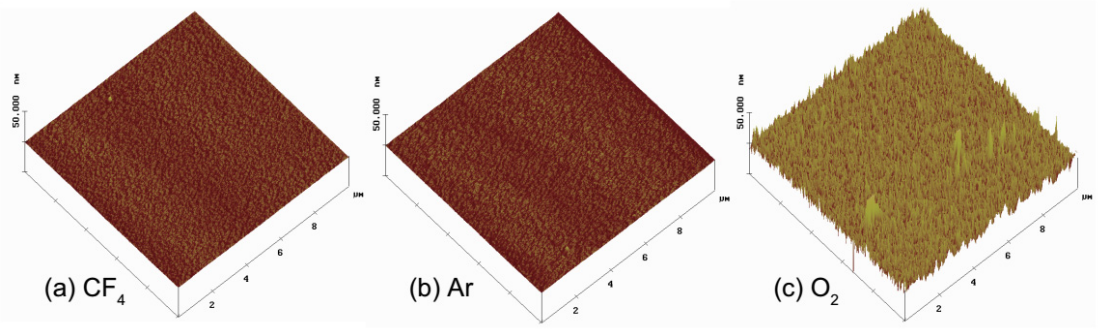

Figure 5 – AFM images on surfaces of the DLC samples etched in the (a) pure-CF_4, (b) Ar and (c) O_2 plasmas. The RMSs indicating roughness on the surfaces in the pure-CF_4, Ar and O_2 plasmas were 0.084, 0.094 and 1.7 nm, respectively

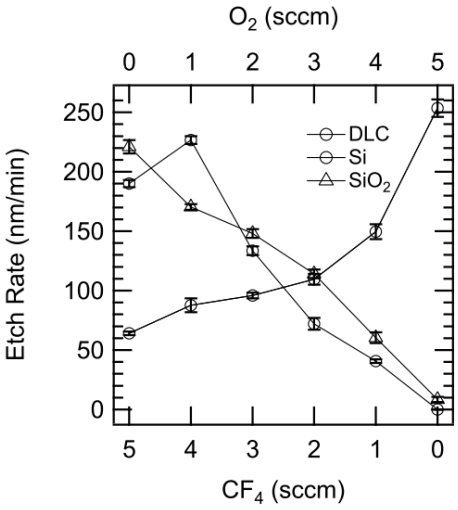

Figure 6 – Etch rate of the DLC in the CF4/O2/Ar plasmas plotted with those of Si and SiO2 as a function of the gas flow rates of CF4 or O2. Etching was performed in changing gas-mixture ratio of [CF4]/[O2] with Ar dilution of 30 sccm. The total flow rate was constant at 40 sccm. The error bars are treated as in Figure 1

4 Conclusions

The DLC was etched in the CF_4/Ar, CF_4/O_2 and CF_4/O_2/Ar plasmas. In the plasmas, F radical worked as an etchant of the DLC in addition to O radical well-known as the etchant in other works. Adding O_2 to the plasmas enhanced etch rates of the DLC. Furthermore, the pure-O_2 plasma had the etch rate highest in all the plasmas. However, it made surface of the DLC rough, implying that highly reactive etching with high etch rates tended to have marked roughness. Conversely, the Ar plasmas could be a candidate of process for etching the DLC with a smooth surface. Its sputter-etching produced abundant dangling bonds on the surface after treatment. The dangling bonds combining with ambient oxygen led the surface of the DLC oxidized. In the fluorine-content plasmas, the dangling bonds were terminated by fluorine atoms, and oxidation on the surface was suppressed by the atoms. In practical processes for fabrication and removing of the DLC, etch rate, its depth, roughness and chemical composition on the surface are required to be controlled well. The present study gives a way to control the etch rate and depth by changing the gas-mixture ratio of CF_4, O_2 and Ar, which also modifies the roughness and suppresses oxidation on the surface preferable to devices of the DLC.

Acknowledgements

This work was partly supported by Toyo Advanced Technologyies Co., Ltd.

References

1 D.S. Mao, J. Zhao, W. Li, C.X. Ren, X. Wang, X.H. Liu, J.Y. Zhou, Z. Fan, Y.K. Zhu, Q. Li, and J. F. Xu. Electron field emission from a patterned diamond-like carbon flat thin film using a Ti interfacial layer // J. Vac. Sci. Technol. – 1999. – Vol.B17. – P. 311 1999.

2 Y. Komatsu, A. Alanazi and, K.K. Hirakuri, Application of diamond-like carbon films to the integrated circuit fabrication process// Diamond Relat.Mater.-1999.-Vol.B8.- P.2018.

3 D.S. Mao, X.H. Liu, X. Wangand, W. Zhu, Electron field emission from diamond-like carbon films and a patterned array by using a Ti interfacial layer // J. Appl. Phys. – 2002 – Vol. 91 – P.3918.

4 A. Bendavid, P.J. Martin, C. Comte, E.W. Preston, A.J. Haq, F.S. Magdon Ismail and R.K. Singh, The mechanical and biocompatibility properties of DLC-Si films prepared by pulsed DC plasma activated chemical vapor deposition // Diamond Relat. Mater. – 2007 –Vol. B16. – P.1616.

5 S. Kumagai, C-Y. Chang, J. Jeong, M. Kobayashi, T. Shimizu and M. Sasaki, Development of plasma-on-chip: Plasma treatment for individual cells cultured in media// Jpn. J. Appl. Phys. – 2016 – V.55 – P.01AF01.

6 R. Hauert, A review of modified DLC coatings for biological applications // Diamond Relat. Mater. – 2003 – V. 12 – P. 583.

7 A. Shirakura, M. Nakaya, Y. Koga, H. Kodama, T. Hasebe and T. Suzuki, Diamond-like carbon films for PET bottles and medical applications// Thin Solid Films.-2006.-Vol. 5 – P.84

8 M. Massi, J. M. J. Ocampo, H. S. Maciel, K. Grigrov, C. Otani, L. V. Santos and R. D. Mansano, Plasma etching of DLC films for micro fluidic channels // Microelectron. J. – 2003. – Vol B34. –P. 635

9 I. Bello, M.K. Fung, W.J. Zhang, K. H. Lai, Y. M. Wang, Z. F. Zhou, R. K. W. Yu, C. S. Lee and, S.T. Lee, Effects at reactive ion etching CVD diamond // Thin Solid Films. – 2000. –Vol.B368. – P.222

10 T. Harigai, H. Koji, H. Furuta and A. Hatta, Formation of Nanofibers on the Surface of Diamond-Like Carbon Films by RF Oxygen Plasma Etching // Jpn. J.Appl.Phys. – 2011. Vol. B. – P.5008JF12.

11 S. Kondo, H. Kondo, Y. Miyawaki, H. Sasaki, H. Kano, M. Hiramatsu and M. Hori, Reactive Ion Etching of Carbon Nanowalls // Jpn. J. Appl. Phys. 2011– V. 50 – P. 075101.

12 M. Sekine, Control of surface reactions in high-performance SiO2 etching //Appl. Srf. Sci. – 2002. – Vol. B. – 192. – P. 270.

13 R.A. Heinecke, Control of relative etch rates of SiO2 and Si in plasma etching // Solid-State Electron. – 1975. – Vol. B18. – P. 1146.

14 R. A. Heinecke, Plasma reactor design for the selective etching of SiO2 on Si // Solid-State Electron. – 1976. – Vol. B19. – P.1039.

15 L.M. Ephrath, Selective Etching of Selicon Dioxide Using Reactive Ion Etching with CF4-H2 // J. Electrochem. Soc. – 1979. – Vol. B126. – P.1419.

16 K. Takahashi, K. Ono and Y. Setsuhara, Etching characteristics of high-k dielectric HfO2 thin films in inductively coupled fluorocarbon plasmas// J.Vac. Sci. Technol. – 2005. – A.23. – P.1691.

17 K. Takahashi and K. Ono, Selective etching of high-k HfO2 films over Si in hydrogen-added fluorocarbon (CF4/Ar/H2 and C4F8/Ar/H2) plasmas // J. Vac. Sci. Technol. – 2006. – A.24. – P.437.

18 D.T. Clark and D. Shuttleworth, Plasma polymerization. III. An ESCA investigation of polymers synthesized by excitation of inductively coupled RF plasmas in perfluorocyclohexa – 1, 3 and 1,4 – dienes, and in perfluorocyclohexene // J. Polym. Sci., Polym. Chem. Ed. – 1980. – Vol. B18. – P.27

19 Y. Horiike and M. Shibagaki, A New Chemical Dry Etching// Jpn. J. Appl. Phys. Suppl. – (1976). – Vol. 15. – P.13

20 D.R. Lide, CRC Handbook of Chemistry and Physics, 79th ed. (CRC Press, Boca Raton, FL, 1998).

21 S.J. Pearton and D.P. Norton, Dry Etching of Electronic Oxides, Polymers, and Semiconductors//Plasma Process. Polym. – 2005. – Vol. B. – P.16.

IRSTI 29.27.51

On the induced charge density distribution in streaming plasmas

Zh.A. Moldabekov, P. Ludwig*, J.-P. Joost and M. Bonitz

Institut für Theoretische Physik und Astrophysik, Christian-Albrechts-Universität zu Kiel, Leibnizstraße 15, 24098 Kiel, Germany
**e-mail: ludwig@theo-physik.uni-kiel.de*

Motivated by experiments on the generation of streaming plasmas in high energy density facilities, industrial setups, and fundamental dusty plasma research, the plasma polarization around a test charge in streaming plasmas is considered in this work. The induced charge density distribution of the plasma constituents is discussed for the subsonic, sonic, and supersonic regime taking into account the non-Maxwellian distribution of the flowing ions. It is shown that the plasma polarization (the plasma wakefield) in the vicinity of the test charge shows different scaling in the subsonic and supersonic regimes, where Mach number is defined as the ratio of the ion streaming velocity and the ion sound speed. In contrast to the wake potential, the density decays strongly monotonically in the plasma wake and does not exhibit an oscillatory pattern or trailing maxima. Therefore, the picture of an ion focusing effect creating a separated ion region downstream was not confirmed.

Key words: complex plasmas, plasma wakefield, plasma polarization, screening, streaming plasmas.
PACS numbers: 52.27 Lw, 52.30.-q, 52.40-w

1. Introduction

Screening of a test charge is one of the fundamental issues of plasma physics. While screening is very well understood in the equilibrium case [1, 2], there is no consistent physical picture of this effect in streaming plasmas. Often, however, a plasma in an experiment is far from the thermodynamically equilibrium state. Therefore, the field of non-equilibrium streaming plasmas attracts broad interest. Examples of non-equilibrium plasmas with a stream of particles include complex plasmas [3, 4], dense plasmas [5, 6], so-called warm dense matter [7], and ultrarelativistic plasmas [8]. Recent experiments have been performed on the generation of streaming plasmas in high energy density facilities [9, 10, 11] as well as industrial setups [12, 13, 14]. Another very active consideration of the streaming induced phenomena such as plasma wakefields is in the field of complex plasmas, which allows for studying collective physical properties of charged many-particle systems on the kinetic level [15].

A complex (dusty) plasma is a partially ionized plasma containing additional micron or submicron sized "dust" particles that become highly charged and actively involved in various multi-component plasma processes [15]. For recent results on the dynamically screened charge potential in streaming plasmas see e.g. Refs. [4, 16, 17, 18, 19] and references therein. A main observation is that streaming leads to a significant deviation from the Yukawa-type screening. In particular, a wakefield around the test charge is formed, giving rise to an attractive force on other like-charged particles downstream. The characteristics of the wakefield potential strongly depend on the type of the energy (velocity) distribution of the plasma particles [17, 20] and on the configuration of external electric as well as magnetic fields [21].

While the potential around a test charge has been explored in detail [16, 22], an appropriate analysis of the induced charge density is still missing. To this end, in this paper, we present preliminary results of the induced charge density and analyse the relevant plasma polarization effects. The results are obtained from high resolution linear response calculations [21, 23] which have been validated against PIC simulations [20].

2. Linear response approach

In experimental complex plasmas, the non-Maxwellian distribution of the flowing ions significantly differs from shifted-Maxwellian distribution often considered in theoretical works [22, 24, 25]. Compared to a shifted-Maxwellian case, the most prominent feature of the ion wake in the non-Maxwellian case is that the screened potential has a single main maximum in the trailing wake instead of an oscillatory wakefield [18]. In contrast, the much lighter electrons can be well described by an equilibrium Maxwellian distribution.

As an ansatz, we use the dielectric function based on the non-Maxwellian distribution of the ions to calculate the induced charge density around the test charge. The dielectric function obtained in the relaxation time approximation reads [24, 26].

$$\varepsilon\left(\tilde{\mathbf{k}},0\right)=1+\frac{1}{\tilde{k}^2\tau}+\frac{1}{\tilde{k}^2+i\nu_i M\,\tilde{k}_z}\frac{1+\left\langle\xi(\mathrm{x})\,\mathrm{Z}(\xi(\mathrm{x}))\right\rangle}{1+\left\langle\xi(0)\,\mathrm{Z}(\xi(0))\right\rangle}\,, \tag{1}$$

where $\left\langle ... \right\rangle = \int_0^\infty ... \exp(-x)\mathrm{d}x$ is the average involving the following functions:

$$\xi(\mathrm{x})=\frac{\imath\nu_i - M\,\tilde{k}_z x}{\sqrt{2\left(\tilde{k}^2+\imath\nu_i M_{th}\tilde{k}_z\right)}}\,,$$

$$Z(\mathrm{z})=\imath\sqrt{\pi}\,\omega(\mathrm{z})\,,$$

$$\omega(\mathrm{z})=\mathrm{e}^{-z^2}\,\mathrm{Erfc}(-\imath\,\mathrm{z})=\frac{\imath}{\pi}\int_{-\infty}^{\infty}\frac{e^{-t^2}}{z-t}\mathrm{d}t\,.$$

In Eq. (1), $\tau = T_e / T_n$ is the electron-neutral temperature ratio, $\tilde{\mathbf{k}}$ is the wave vector in units of $\upsilon_{th} / \omega_{pi}$ (where υ_{th} is the thermal velocity of atoms and ω_{pi} is the plasma frequency of ions), and ν_i is the the ion-neutral collision frequency in units of ion plasma frequency. Additionally, the Mach number $M = \upsilon_d / c_s$ is defined as the ratio of the ion streaming velocity υ_d and the ion sound speed $c_s = \sqrt{k_B T_e / m_i}$.

In k-space, the charge density induced by a test charge Q_d can be expressed in terms of the dielectric function (1) [6]:

$$\tilde{n}_{ind}\left(\tilde{\mathbf{k}}\right)=\frac{Q_d}{e}\left(\frac{1}{\varepsilon\left(\tilde{\mathbf{k}},0\right)}-1\right)\,. \tag{2}$$

This expression is favorable for numerical evaluation. The induced charge density is then computed in real space based on a numerical three-dimensional Discrete Fourier Transformation (3D DFT) on a large grid with resolutions $4096\times4096\times16384$. In order to handle 3D grids of this size efficently, our high performance linear response program *Kielstream* is used [27].

Without loss of generality, we consider a grain charge of $Q_d = 10^4 e$. Specific parameters are the fixed temperature ratio $\tau = 100$, and the ion-neutral collision frequency $\nu_i = 0.01$, which is close to the collisionless case. The Mach number is varied in the range $M = 0.1 \ldots 2.8$. We note that for very small ion streaming velocities the linear response approach may not be applicable due to strong dust-plasma interactions. Also justification of the consideration of very large values of M can be problematic due to a possible manifestation of instabilities [18, 26].

3. Results for the induced charge density distribution

As a representative example, in Figure 1, we show contour plots of the dynamically screened test charge potential and of the corresponding induced charge density distribution in the sonic case, $M = 1$. In contrast to the well-known wakefield potential, where a pronounced trailing peak is present, here we find that the pattern of the induced charge density has a completely different topological structure. The induced charge density is purely monotonic. Notably, this observation contradicts the widely used picture of an ion cloud focused at some

distance from the test charge. Instead the density wake resembles a candle flame. Accordingly, this results in weaker screening at $z < 0$, and appearance of an area, at $z > 0$, where another like charged test particle is attracted [16].

The dependence of the induced charge density in the cases of subsonic and supersonic regimes are presented in Figure 2. The main feature to be noticed, is that the characteristic flame type shape is retained for all values of M. With increase of the Mach number it becomes more extended in the direction of the streaming.

In Figure 3, the induced charge density profile along z axis at $r = 0$, i.e., parallel to the streaming direction passing the test particles location, is given. Indeed, for all considered Mach numbers, there are no oscillations in the density wake field. With increase of the ion flow velocity, the induced charge density decreases in the upstream direction of the test charge, $z > 0$, while gradually increasing downstream, $z < 0$. Again, from Figure 3, one can clearly see that there are no oscillations (no maximum) in the density distribution as seen in the wake potential.

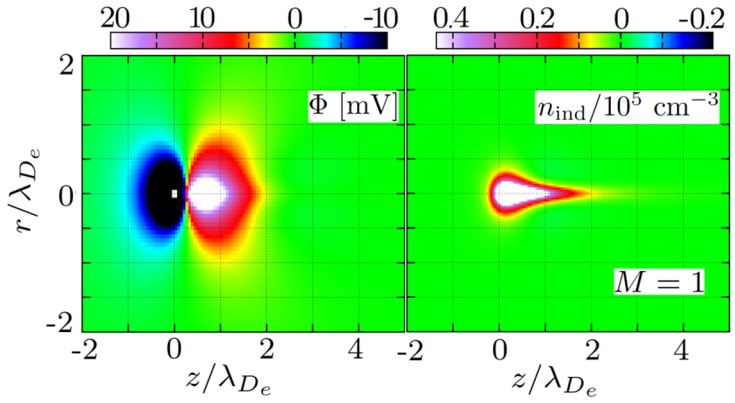

Figure 1 – Electric potential (left) and induced charge density (right) around the test charge for $M = 1$. We use cylindrical coordinates with ions streaming in positive z-direction, where the test charge is located at the origin

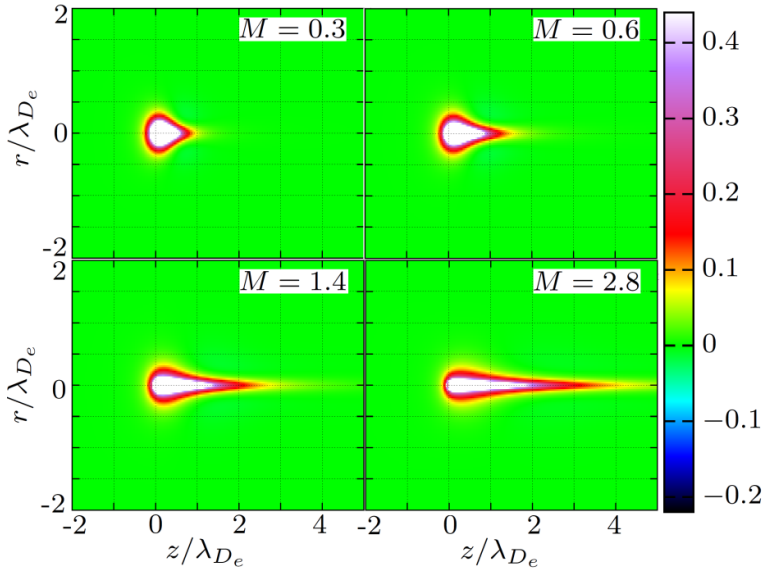

Figure 2 – Induced charge density in units of $10^5\ cm^{-3}$ for subsonic ($M = 0.3$, $M = 0.6$) and supersonic ($M = 1.4$, $M = 2.8$) regimes. For the sonic case we refer to Figure 1

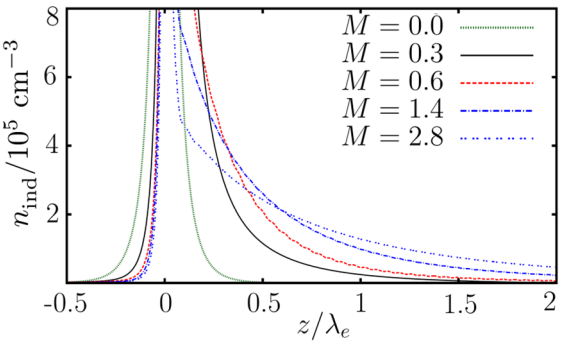

Figure 3 – Induced charge density around the test charge along streaming direction ($r = 0$) revealing a strictly monotonic behavior

4. Characteristics of the plasma polarization

The plasma quasineutrality condition ensures that the test particle charge Q_d is compensated by the charge of the induced density distribution n_{ind} (screening cloud), i.e., $Q_{ind} = \int e\, n_{ind}\, \mathrm{d}V = -Q_d$. This also holds in the case of streaming plasmas, where the ion streaming cannot change the charge balance.

In case of statical screening, n_{ind} is given by the Yukawa density distribution,

$$n_{ind}^{Y}(\mathrm{r}) = \frac{Q_d}{4\pi e} k_s^2 \frac{\exp(-\mathrm{k}_s \mathrm{r})}{r}\ , \qquad (3)$$

where $k_s^2 = 1/\lambda_e^2 + 1/\lambda_i^2$, and $\lambda_{e(\mathrm{i})} = \sqrt{k_B T_{e(\mathrm{i})} / 4\pi e^2 n}$. In turn, in the case of dynamical screening, from the plasma quasineutrality condition, we deduce that the volume integrated deviation of n_{ind} from the Yukawa density distribution, $n_{ind}^{*} = n_{ind} - n_{ind}^{Y}$, is zero, i.e. $Q_{ind}^{*} = \int e\, n_{ind}\, \mathrm{d}V = 0$. Comparison with the static case, n_{ind}^{Y}, yields that the charge depletion Q_{ind}^{-} (described by $n_{ind}^{*} < 0$) is equal to the charge enhancement Q_{ind}^{+} (given by $n_{ind}^{*} > 0$). That means, the ionic Debye screening cloud around the dust particle is shifted and deformed by streaming ions but keeps its volume. The latter has been validated by direct volume integration.

In Figure 4 the value of the accommodated charge due to streaming is presented for different values of $\tau = T_e / T_n$ (100, 30, and 10). A large amount of the induced charge is displaced from the direct vicinity of the test particle downstream in the wake of the test particle. Additionally, the amount of the accommodated charge in the wakefield does not exceed the absolute value of the test particle charge. While there is a rapid increase of the accommodated charge n_{ind}^{*} at small M, for larger Mach numbers the wake charge slowly approaches Q_d.

So far, our consideration did not include the shape of the screening cloud (the plasma polarization) and it change during the transition from the subsonic to supersonic regime. To point this out, we consider the dipole moment due to the deformation of the induced charge density $\mathbf{d} = \int \mathbf{r}\, e n_{ind}(\mathbf{r})\, \mathrm{d}V$. Due to symmetry of the induced charge density, $\mathbf{d}$ is directed along z axis. In Figure 5, the absolute value of $\mathbf{d}$ in units of $|\mathrm{Q}_d|\lambda_e$ is shown as the function of the Mach number on a logarithmic scale. From this figure, one can see that the slope of dependence of $d = |\mathbf{d}|$ on M increases during the crossover from the subsonic to the supersonic regime. Therefore, the transition is well characterized by the ratio of the dipole moment to the ion flow speed, that is to say by the effective "polarizability" of the screening cloud. This quantity is presented in the inset of Figure 5. At $M < 0.5$, one finds that $d^* \sim 0.25 \times M$, and at $M > 1.5$, $d^* \sim M^2$. Therefore, the subsonic case can be characterized as linear polarization regime, whereas the supersonic case corresponds to the regime with nonlinear plasma polarization. In the subsonic regime, the linear growth of d^* with increase in the Mach number is mainly due to fast increase of the charge enhancement (see dependence of Q_{ind}^{+} on M in

Figure 4. In the supersonic regime, where the charge enhancement changes slowly with increase in M, the dominant mechanism responsible for the quadratic growth of d^* is the displacement of the ionic screening cloud to larger distances (see Figures 2 and 3).

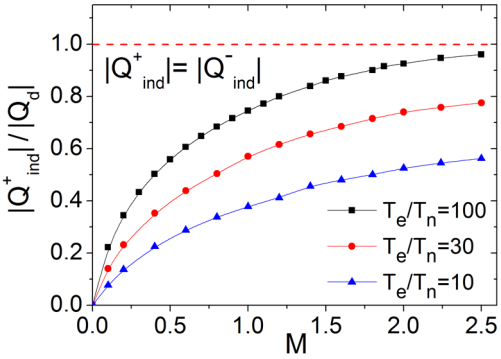

Figure 4 – Charge enhancement as function of the ion flow velocity for different electron-neutral temperature ratios

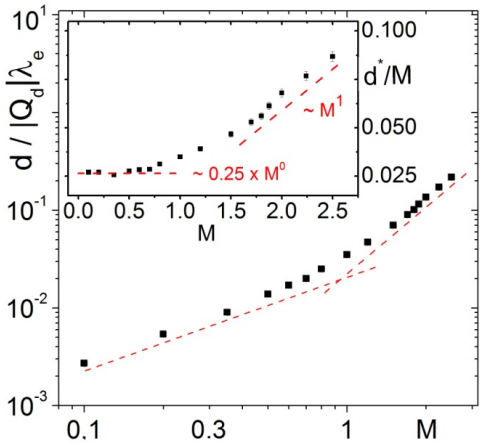

Figure 5 – Dipole moment $d^* = d / (|\,Q_d\,|\,\lambda_e)$ of the induced charge density as a function of the Mach number. The transition from the linear to non-linear polarization regime is illustrated in the inset plotting the ratio of d^* to M on a linear scale. Red lines are a guide to the eye

5. Conclusions

Considering a streaming plasma, the calculation of the induced density distribution around a test charge, taking into account the non-Maxwellian distribution of the flowing ions, reveals first results for the actual plasma polarization. In particular, it has been revealed that the density profile is stricly monotonic so there are no oscillations and maximums in the wake density at all. The shape of the induced charge possesses the topology of a "candle flame". The picture of an ion focusing effect creating a separated ion region downstream is therefore questionable. At the considered parameters, the characteristic length scale of the wake density is $l \geq \lambda_e$. It remains an open question whether the field can be described at large distances $r \gg l$ using the dipole approximation.

Acknowledgments

Zh.A. Moldabekov gratefully acknowledges funding from the German Academic Exchange Service (DAAD). This work was supported by the Deutsche Forschungsgemeinschaft via SFB-TR 24 (projects A2 and A9).

References

1 M. Lampe, G. Joyce. Grain-grain interaction in stationary dusty plasma // Phys. Plasmas. – 2015. – Vol. 22. – P. 023704.

2 Zh. Moldabekov et al. Statically screened ion potential and Bohm potential in a quantum plasma // Phys. Plasmas. – Vol. 22. – P. 102104.

3 R. A. Quinn, J. Goree. Particle interaction measurements in a Coulomb crystal using caged-particle motion // Phys. Rev. Lett. – 2002. – Vol. 88. – P. 195001.

4 M.-J. Lee, Y.-D. Jung. Space-charge wave in a dusty plasma column containing collisional streaming ions // Physical Sciences and Technology. – 2016. – Vol. 3. – No. 2. – P. 20-24.

5 O. Hurricane et al. Fuel gain exceeding unity in an inertially confined fusion implosion // Nature. – 2014. – Vol. 506. – P. 343.

6 Zh. Moldabekov et al. Ion potential in warm dense matter: Wake effects due to streaming degenerate electrons // Phys. Rev. E. – 2015. – Vol. 91. – P. 023102.

7 N.A. Tahir et al. Proposal for the study of thermophysical properties of high-energy-density states in matter using current and future heavy ion facilities at the GSI Darmstadt // Phys. Rev. Lett. – Vol. 95. – P. 035001.

8 M.H. Thoma, Field theoretic description of ultrarelativistic electron-positron plasmas, Rev. Mod. Phys. – 2001. – Vol. 81. – P. 959.

9 F. Taccogna et al. Plasma-neutral interaction in kinetic models for the divertor region // Contrib. Plasma Phys. – 2008. – Vol. 48. – P. 147.

10 Y. Tanaka et al. Influence of emissivity on behavior of metallic dust particles in plasmas // Phys. Plasmas. – 2008. – Vol. 15. – P. 073704.

11 S. K. Kodanova et al. Dust particle evolution in the divertor plasma // IEEE Transactions on Plasma Science. – 2016. – Vol. 44. – P. 525.

12 L. Boufendi et al. Study of initial dust formation in an Ar-SiH4 discharge by laser induced particle explosive evaporation // J. Appl. Phys. – 1994. – Vol. 76. – P. 148.

13 L. Boufendi. A. Bouchoule. Industrial developments of scientific insights in dusty plasmas // Plasma Sources Science & technology. – 2002. – Vol. 11. – P. A211.

14 R.I. Golyatina, S.M. Maiorov. Ion drift in parent gas for cesium, rubidium, and mercury // Physical Sciences and Technology. – 2016. – Vol. 3. – P. 12.

15 M. Bonitz, C. Henning, D. Block. Complex plasmas – a laboratory for strong correlations // Reports on Progress in Physics. – 2010. – Vol. 73. – P. 066501.

16 P. Ludwig et al. On the wake structure in streaming complex plasmas // New J. Phys. – 2012. –Vol. 14. – P. 053016.

17 Zh. Moldabekov et al. Dynamical screening and wake effects in classical, quantum, and ultrarelativistic plasmas // Contributions to Plasma Physics. – 2015. – Vol. 55. – P. 186.

18 R. Kompaneets, G.E. Morfill, A.V. Ivlev. Wakes in complex plasmas: A self-consistent kinetic theory // Phys. Rev. E. – 2016. – Vol. 93. – P. 063201.

19 W. J. Miloch. Wake effects and mach cones behind objects // Plasma Physics and Controlled Fusion. – 2010. – Vol. 52. – P. 124004.

20 S. Sundar et al. Collision induced amplification of wakes in streaming plasmas // Phys. Plasmas. – 2017. – Vol. 24. – P. 102130.

21 J.-P. Joost et al. Screened coulomb potential in a flowing magnetized plasma // Plasma Physics and Controlled Fusion. – 2015. – Vol. 57. – P. 025004.

22 P. Ludwig et al. Non-Maxwellian and magnetic field effects in complex plasma wakes // Eur. Phys. J. D. – 2018. – Vol. 72. – P. 82.

23 P. Ludwig. C. Arran, M. Bonitz. Complex plasmas: scientific challenges and technological opportunities, edited by M. Bonitz, J. J. Lopez, K. Becker, H. Thomsen.– Springer, New York, 2014. – P. 73-99.

24 H. Kählert. Ion-dust streaming instability with non-Maxwellian ions // Phys. Plasmas. – 2015. – Vol. 22. – P. 073703.

25 K.I. Golden, G.J. Kalman, L.G. Silvestri. Is the Vlasov equation valid for Yukawa plasmas? // Physical Sciences and Technology. – 2017. – Vol. 4. – P. 9.

26 A. V. Ivlev et al. Kinetic approach for the ion drag force in a collisional plasma // Phys. Rev. E. – 2005. – Vol. 71. – P. 016405.

27 P. Ludwig, C. Arran, M. Bonitz. Introduction to streaming complex plasmas B: Theoretical description of wake effects complex plasmas: Scientific challenges and technological opportunities. – Springer, New York, 2014. – P. 73–99.

IRSTI 29.27.29

Dust grain in streaming ions with temperature variation

S. Sundar

Department of Aerospace Engineering, Indian Institute of Technology,
Chennai - 600036, Madras, India
e-mail: sitaucsd@gmail.com

This work presents improved numerical observations to demonstrate influence of the ion-to-electron temperature ratio on the dust grain in streaming non-Maxwellian ions for a range of ion speeds. Increase in electron-to-ion temperature ratio influences the ion-grain dynamics substantially and manifests itself as an enhancement in the wake amplitude. The interplay of streaming ion speed with temperature and their synergistic impact on the wake potential and density of the grain is discussed in detail. Physical properties like peak potential and peak position and its dependence on temperature, collision, and streaming speeds is presented. A comparison of the results obtained using 3D-6V particle-in-cell simulation with that of the linear response approach is delineated systematically. At lower temperature, peak potential and peak position exhibit monotonic increase with collision. However, at higher temperature the behavior becomes non-monotonic and initially exhibits an increase in the peak potential with collision and then a decreasing trend. For moderate streaming speeds at lower temperatures, splitting of ion focus behind grain is observed from the density contours as well as three-dimensional potential plots. Our results are reasonably consistent with that of the earlier results reported using Linear Response formalism, nevertheless, in certain regimes it endows us with richer physics.

Key words: complex plasmas, plasma wakefield, plasma polarization, streaming plasmas.
PACS numbers: 52.27 Lw, 52.30.-q, 52.40-w

1. Introduction

Presence of dust is ubiquitous in universe and so is its importance from the fundamental and practical application aspect. It has been one amongst the widely investigated research area due to its relevance to physical phenomena like Saturn rings [1], lunar wakes [2], Fusion devices [3], dust charging and collective effects [4] as well as wakes in laboratory plasmas, space plasmas [5] etc. Strong coupling is known to influence the low frequency collective modes in dusty plasmas [6, 7] and the nonlinear propagation of these very low-frequency waves has been presented using generalized hydrodynamic model [7]. Collisional instabilities in a dusty plasma with recombination and ion-drift effects of dust acoustic waves has also been noted [8].

Charged lunar dust has been reported to be a major concern [9] for exploration activities due to its strong adhesive property. A wake forms downstream of the Moon when it is present in the Solar window. Moon is known to spend almost a quarter of its orbit time in the magneto-sheath where the temperature is higher than that in the solar window. Influence of temperature on electrostatic nonlinear ion waves has been reported utilizing numerical schemes [10]. The temperature variation affects charging and other associated attributes significantly and makes it pertinent to advance our theoretical understanding of the Physics of dust grain. To understand the impact of temperature on dust grain, herein we model a system with single grain in the presence of streaming ions.

For a system of an isolated dust grain in stationary plasma, the electrons bombard continuously on the grain owing to its comparatively higher mobility eventually making the dust grain negatively charged. Due to the local charge imbalance, the negatively charged dust grain is shielded mostly by ions added with electrons. Now the grain is surrounded by ions symmetrically from all sides by positive charged ions. This way we have the charge of the grain shielded by the ions which in turn is shielded by the electrons.

But many a times it has been observed that the sheath region has an electric field which give ions a flow or directionality. This breaks the symmetrical ion shielding around the grain and introduces asymmetry. In the presence of the ambient electric field in the sheath region, ions flow towards the grain and accumulate behind it eventually giving rise to an ion focusing. This ion focus, in turn, attracts electrons, which attracts ions and so on. This way we have a streamlined negative charge followed by positive and negative charges. Such a juxtaposition manifests itself in the form of potential oscillations and has often been called `wake' behind the grain. This laboratory wake behind grain has a strong analogy with the lunar wake of Moon in solar wind flow. In order to understand the underlying Physics, we mimic such a system numerically and explore the effect of temperature variation coupled with varying ion streaming speeds using particle-in-cell simulation.

The wake behind grain is known to be susceptible to external electric and magnetic fields, grain size versus Debye length a / λ_{De}, collision frequency ratio, v_{in} / λ_{De}, ion streaming speeds or Mach number M as well as electron-ion temperature ratio, T_e / T_i where a is the grain radius, λ_{De} is the electron Debye length, T_e (T_i) is the electron (ion) temperature, and v_{in} denotes the ion-neutral charge exchange collisions frequency and ω_e is the electron plasma oscillation frequency. Among the collisions affecting the wake features, the most dominant is the ion-neutral charge exchange collision [11] and is considered in most of the numerical experiments. However, the aim of the present work is to explore the dependence of wake physics on electron-to-ion temperature, T_e / T_i.

It has been reported in the previous works that the wake behind grain exhibits a monotonic dependence on the T_e / T_i [12], however, the work has mostly been done keeping the distribution of ions to be Maxwellian or shifted-Maxwellian. Note that the presence of electric field and/or collision impart the ions a directionality and the distribution is no longer Maxwellian rather it has long tail along the streaming direction eventually giving rise to a non-Maxwellian distribution [11, 13-15]. Recently, in one of the works, effect of temperature on wake for non-Maxwellian streaming ions is presented in brief [13]. Here, we explore the influence on wake behind grain due to interplay of temperature and streaming speed variation.

The outline of the present work is as follows. In section 2, we first introduce the simulation scheme utilized followed by the description of methodology. In section 3, we present the systematic results regarding the impact of temperature and ion flow variation on the grain in streaming ions. Finally, we present a summary and conclusion in section 4 followed by acknowledgments in section 5.

2. Linear response approach

Our simulations have been performed with the state-of-the-art three-dimensional Cartesian mesh, oblique boundary, particles and thermals in cell COPTIC code [16]. We are exploring the dynamics at ion time scale and have safely assumed the electron to obey the Boltzmann distribution,

$$n_e = n_{e\infty} \exp\left(e\phi / k_B T_e\right), \tag{1}$$

where Boltzmann constant is taken to be unity. The equation to delineate the ion dynamics in six-dimensional phase space in the presence of the self-consistent electric field $-\nabla\phi$, an optional external force **D** [17] is given by

$$m_i \frac{d\mathbf{v}}{dt} = e\left[-\nabla\phi\right] + \mathbf{D}. \tag{2}$$

When the ion distribution is non-Maxwellian [11], the external force **D** is non-zero and is responsible for the ion drift while neutrals are stationary. We have performed simulations on a 32 × 32 × 96 cell grid with more than 15 million ions in the domain. To retrieve the dynamics near grain, we have performed few simulations with even higher resolutions and number of particles. Most of the simulation runs were evolved for 1000 time steps. A list of parameters employed during simulation is presented in Table 1. The normalization scheme and further simulation details could be followed from the recent work [11].

Table 1– Detailed list of the simulation parameters

Temperature ratio, T_e / T_i	10 - 100
Mach Number, M	0.1 - 1.0
Collision frequency, v_{in} / ω_e	0.002 -1.5
Electron Debye length, λ_{De}	5
Grid size,	64 × 64 × 128
Number of particles,	60 × 10^6
Total number of time steps,	1000
Grain potential, ϕ_a	0.05-0.2
Time-step, dt	0.1

3. Results

Temperature has been to known affect the grain dynamics and wake oscillations besides role in Landau damping. Here, we investigate the explicit role played by temperature on wake oscillations and its interplay with ion streaming speeds and collision frequency. At higher temperature shielding is reduced and wake effects become prominent. Wake features are best observed at a temperature ratio of 100 and weakens as one lowers the temperature. A contour plot of the wake potential for two different temperature ratios (50 and 100) is shown in Figure 1. Subplots (a)-(b) correspond to $M = 0.5$ and (c)-(d) to $M = 1$. As reported earlier [11], here also, we observe that there are no multiple wake oscillations behind grain rather a single ion focus region. Ion focusing is stronger at as one increases the electron temperature and also at higher ion flows eventually leading to higher first peak potentials. Contrary to some previous research reports [13], at very low temperature ratios i.e. $T_e / T_i = 10$, we didn't observe any ion focusing or positive potential peak downstream grain.

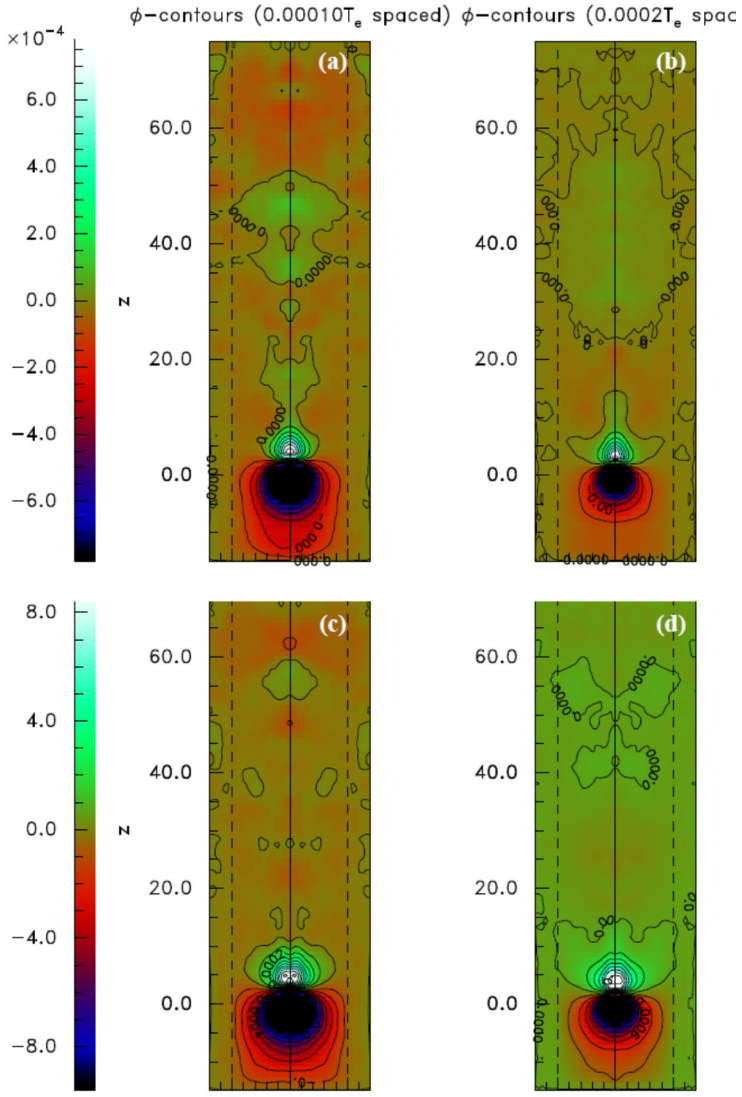

Figure 1 – Wake potential contours $e\phi / k_B T_e$, averaged over the azimuthal angle for (a) $M = 0.5$, $T_e / T_i = 50$, (b) $M = 0.5$, $T_e / T_i = 100$, (c) $M = 0.8$, $T_e / T_i = 50$, and (d) $M = 0.8$, $T_e / T_i = 100$. Here, the grain is at the origin and the normalized grain charge is $Q_d = 0.1$

A. Interplay of ion flow speed and collisionality with electron-ion temperature ratio on wakefield potential

We have seen that increase in temperature ratio increases the wake peak height. Similar effect is exhibited by increase in the ion flow speed. However, presence of collision in the system complicates the dynamics further and the change is no longer monotonic. In Figure 2, the wake first peak position (top) and peak amplitude (bottom) in normalized units as a function of Mach number is illustrated for two different temperature ratios 50 and 100. In agreement with previous research reports [11, 13] for temperature ratio 100, here also, the wake first peak potential has a bell shape curve with ion flow speed and is non-monotonic clearly exhibiting a maxima around $M = 0.5$. Exploring the wake features at lower temperatures leads us to the outcome that at lower temperature the variation in wake peak height with ion streaming speed is very small and is almost constant over the whole range. The wake amplitude decreases substantially with decrease in temperature ratio (i.e. at 50) and becomes negligible as one decreases the temperature ratio further below 10. The wake peak position is nearer to the grain at higher temperature and moves farther as we decrease the temperature. Effect of collisionality on wake peak height coupled with variation in temperature is shown in Figure 3. At higher temperature ratio (i.e. at 100), the wake peak exhibits enhancement with increase in collision frequency which further decreases at very high collisionality. However, at lower temperature ratios (i.e. at 50), the wake peak height versus collision is monotonically increasing with collisionality. Nevertheless, the wake peak amplitude at temperature ratio 50 is substantially smaller compared to that at higher temperature ratio 100. Wake peak position at temperature ratio 50 is almost constant for the whole range of collisionality. On the other hand, for temperature ratio 100, it is constant till $\nu_{in} / \omega_e = 0.6$ and exhibits an increase at higher collisionality. Note that the location of the wake peak is farther from the grain for temperature ratio 50 at lower collisonality and is closer to the grain at higher collisionality when compared with higher temperature ratio 100.

B. Impact of temperature on the ion density distribution

Wake effects are inherently related to the density and has profound effect on the density distribution. For the two different temperature ratios, the spatial profiles of the density is shown in Figure 4. The single ion focus behind grain can be traced from the density profiles. One peculiar observation we have here is for $M = 0.8$ with $T_e / T_i = 50$. In this case, the ion focus is not streamlined behind the grain but is splitted in two ion bunched behind grain. In 3D potential plots also, we were able to observed splitting of the positive peak potential behind grain.

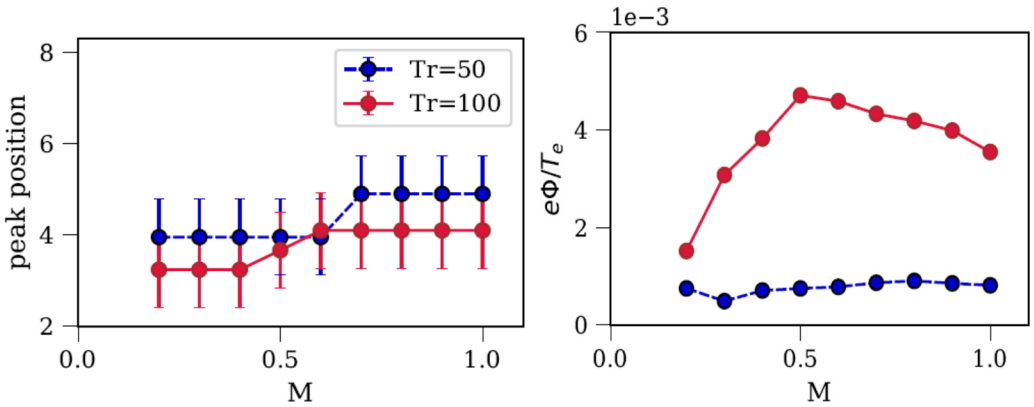

Figure 2 – Peak position (top) and peak amplitude (bottom) of the wake potential in normalized units as a function of Mach number, M, for $T_e / T_i = 100$ (solid) and $T_e / T_i = 50$ (dashed) drift-driven distribution, for the collision frequency $\nu = 0.1$ and $Q_d = 0.1$

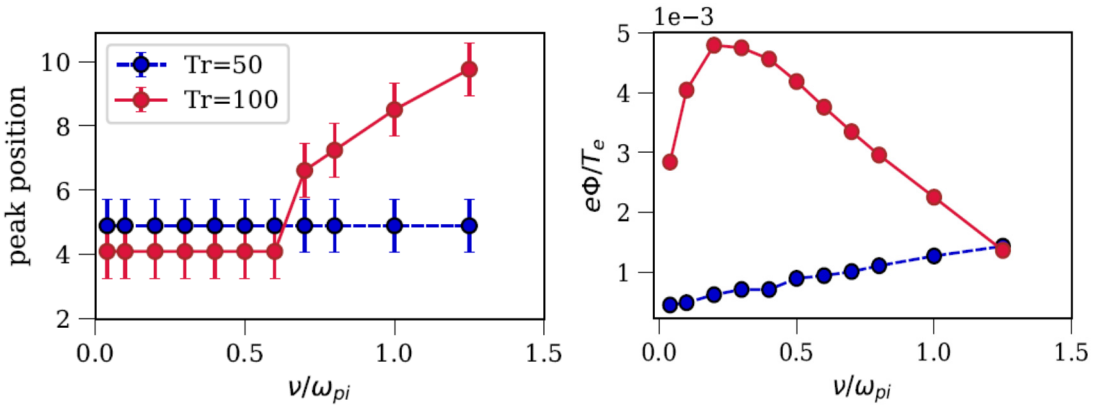

Figure 3 – Peak position (top) and peak amplitude (bottom) of the wake potential in normalized units as a function of collision frequency ν_{in} / ω_e, for $T_e / T_i = 100$ (solid) and $T_e / T_i = 50$ (dashed) drift-driven distribution, $M = 0.8$ and $Q_d = 0.1$

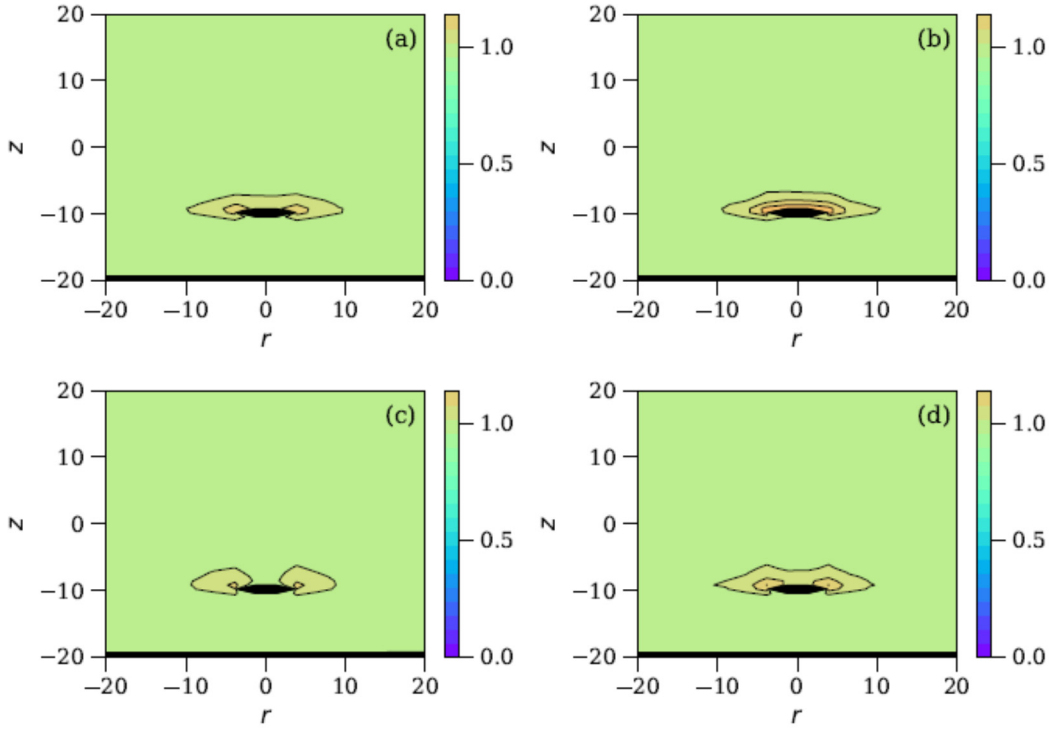

Figure 4 – Spatial profiles of the ion density (normalized to the distant unperturbed ion density), averaged over the azimuthal angle, for (a) $M = 0.5$, $T_e / T_i = 50$, (b) $M = 0.5$, $T_e / T_i = 100$, (c) $M = 0.8$, $T_e / T_i = 50$, and (d) $M = 0.8$, $T_e / T_i = 100$

4. Conclusions

The present numerical work demonstrates the influence of temperature variation on the wake feature and facilitates understanding of wake formation for grain in non-maxwellian streaming ions. We have explored the role played by electron-ion-temperature ratio on the wake formed behind grain due to ion focusing. The wake peak is observed to exhibit monotonic increase with increase in electron-to-ion temperature ratio. The variation in wake peak gets further complicated by

the inclusion of varying ion flow speeds and collisionality. The density distribution presented validates the potential profile observations and puts the result on firm footing. Thorough understanding of parametric dependence of wake peak has wider implications which includes space physics, lunar wakes, laboratory experiments. Physical insights gleaned from the temperature variation effect has the potential provide an improved physical basis for thermo-phoretic force close to walls in dusty plasma experiments [19-25] eventually leading to better perspective for levitation experiments. One of the NASA research report suggests the presence of unwanted dust in space suit as well as in the lunar atmosphere [2] which could have toxic effects and calls for further research. The dust in space mission has adhesive properties which is susceptible to thermal effects. In that direction, the present work can prove to be fruitful in further exploration.

Acknowledgments

S. Sundar would like to thank I. H. Hutchinson for support in using the COPTIC code and acknowledge the support of CAU Kiel. This work was funded by the DFG via SFB-TR24, project A9. Our numerical simulations were performed at the HPC cluster of Christian-Albrechts-Universitaet zu Kiel. S. Sundar would like to thank Zh. Moldabekov from Uni Kiel for his help in scientific discussion.

References

1 O. Havnes, T. Aslaksen, T. W. Hartquist, F. Li, F. Melandsø, G. E. Morfill, T. Nitter. Probing the properties of planetary ring dust by the observation of Mach cones // Journal of Geophysical Research: Space Physics. – 1995. – Vol. 100. – P. 1731.

2 W. M. Farrell T. J. Stubbs R. R. Vondrak G. T. Delory J. S. Halekas. Complex electric fields near the lunar terminator: The near-surface wake and accelerated dust // Geophysical Research Letters. – 2007. – Vol. 34. – P. 029312.

3 J. Winter. Plasma physics and controlled fusion dust in fusion devices—a multi-faceted problem connecting high- and low-temperature plasma physics / Plasma Physics and Controlled Fusion. – 2004. – Vol. 46. – P. B583.

4 M. R. Jana, A. Sen, P. K. Kaw. Collective effects due to charge-fluctuation dynamics in a dusty plasma // Phys. Rev. E. – 1993. – Vol. 48. – P. 3930.

5 F. Verheest. Waves and instabilities in dusty space plasmas // Space Science Reviews. – 1996. – Vol. 77. – P. 267.

6 P. K. Kaw, A. Sen. Low frequency modes in strongly coupled dusty plasmas // Physics of Plasmas. – 1998 – Vol. 5. – P. 3552.

7 B. M. Veeresha, S. K. Tiwari, A. Sen, P. K. Kaw, A. Das. Nonlinear wave propagation in strongly coupled dusty plasmas // Phys. Rev. E. – 2010. – Vol. 81. – P. 036407.

8 P. Kaw, R. Singh. Collisional Instabilities in a dusty plasma with recombination and ion-drift effects // Phys. Rev. Lett. – 1997. – Vol. 79. – P. 423.

9 T. J. Stubbs, R. R. Vondrak, W. M. Farrell. Impact of dust on lunar exploration // Workshop on Dust in Planetary Systems Book Series: ESA special publications. – 2007. – Vol. 643 – P. 239-243.

10 Y.-N. Nejoh The dust charging effect on electrostatic ion waves in a dusty plasma with trapped electrons // Physics of Plasmas. – 1997 – Vol. 4. – P. 2813.

11 J. Vranjes, H. Saleem, S. Poedts Ion temperature gradient instability in a dusty plasma // Physical Review E. – 2004. – Vol. 69. – P. 056404.

12 S. Sundar, H. Kählert, J.-P. Joost, P. Ludwig, M. Bonitz. Impact of collisions on the dust wake potential with Maxwellian and non-Maxwellian ions // Physics of Plasmas. – 2017. – Vol. 24. – P. 102130.

13 P. Ludwig, W. J. Miloch, H. Kählert, M. Bonitz. On the wake structure in streaming complex plasmas // New Journal of Physics. – 2012. – Vol. 14. – P. 053016.

14 P. Ludwig, H. Jung, H. Kählert, J.-P. Joost, F. Greiner, Zh. Moldabekov, J, Carstensen, S. Sundar, M. Bonitz, A. Piel. Non-Maxwellian and magnetic field effects in complex plasma wakes // The European Physical Journal D. – 2018. – Vol. 72. – P. 82.

15 H. Kaehlert. Ion-dust streaming instability with non-Maxwellian ions // Physics of Plasmas.–2015. – Vol. 22. – P. 073703.

16 S. Sundar. Wake effects of a stationary charged grain in streaming magnetized ions // Physical Review E. – 2018. – Vol. 98. – P. 023206.

17 I. H. Hutchinson. Nonlinear collisionless plasma wakes of small particles // Physics of Plasmas. – 2011. – Vol. 18. – P. 032111.

18 I. H. Hutchinson, C.B. Haakonsen. Collisional effects on nonlinear ion drag force for small grains // Physics of Plasmas. – 2013. – Vol. 20. – P. 083701.

19 O. Havnes, T. Nitter, V. Tsytovich, G. E. Morfill, T. Hartquist. On the thermophoretic force close to walls in dusty plasma experiments // Plasma Sources Science and Technology. – 1994. – Vol. 3. – P. 448.

20 V. Nosenko, S. Zhdanov, A. V. Ivlev, G. Morfill, J. Goree, A. Piel. Heat transport in a two-dimensional complex (dusty) Plasma at melting conditions // Phys. Rev. Lett. – 2008. – Vol. 100. – P. 025003.

21 V. Nosenko, J. Goree. Shear flows and shear viscosity in a two-dimensional Yukawa system (dusty plasma) // Phys. Rev. Lett. – 2004. – Vol. 93. – P. 155004.

22 D. Samsonov et. al. Instabilities in a dusty plasma with ion drag and ionization // Phys. Rev. E. – 1999. – Vol. 59. – P. 1047.

23 J. Winter. Dust in fusion devices - experimental evidence, possible sources and consequences // Plasma Physics and Controlled Fusion. – 1998. – Vol. 40. – P. 1201 - 1210.

24 D. Samsonov, S. Zhdanov, G. Morfill, V. Steinberg // New Journal of Physics. – 2003. – Vol. 5. – P. 24.

25 T. G. Northrop. Dusty plasmas // Physica Scripta. – 1992. – Vol. 45. – P. 475-490.

IRSTI 29.19.22

The formation of SiC films by magnetron sputtering

K.Kh. Nussupov, N.B. Beisenkhanov*, B.Zh. Seitov,
D.I. Bakranova and S.Keyinbay

Kazakh-British Technical University,
Tole bi str.59, 050000 Almaty, Kazakhstan
**e-mail: beisen@mail.ru*

This paper is devoted to the synthesis of solid silicon carbide (SiC_x) films on the surface of single-crystal silicon (c-Si) with a thin interlayer of amorphous silicon (a-Si) by magnetron sputtering as well as to establish new regularities in the influence of heat treatment on composition, crystallization processes and structure of layers. A principal difference between the method of synthesis and the traditionally used magnetron sputtering is the 13.56 MHz high-frequency magnetron sputtering of a silicon target and a graphite target. An amorphous $SiC_{0.97}$ film with a density of 3.179 g/cm^3 and 165 nm thick was obtained under the deposition regime: rf = 150 W, 13.56 MHz; Ar – 2.4 l/h, 0.4 Pa; 100°C, 2400 s; containing SiC nanocrystals after annealing (1100°C, 30 min, Ar). Synthesis of an amorphous SiC_x film with a density of 3.204 g/cm^3 at a long sputtering of Si and C targets – 14400 s, containing nanoclusters with a predominance of truncated SiC bonds, was carried out.

Key words: silicon, semiconductors, silicon carbide, crystallization, magnetron sputtering
PACS numbers: 81.15.Cd; 61.10.Nz; 61.10.Kw; 78.30.-j.

1 Introduction

Important physical and chemical properties of silicon carbide for semiconductor electronics, such as wide bandgap (Eg = 2.3–3.5 eV), high melting point (2830°C), high chemical resistance and thermal conductivity, high carrier mobility and hardness (33400 Mn/m^2) caused its wide application in radiation-resistant electronics, high-temperature electronics, high-frequency electronics, optoelectronics [1-3]. Silicon carbide is also widely used as heat-resistant materials in the manufacture of rifled discs and drills, in the design of thermonuclear reactors, in composition heat-resistant materials, in coatings of the hull of spacecrafts [4]. Electronic devices based on SiC have a high speed and the ability to work at temperatures up to 600 °C [5, 6].

Unfortunately, since it is still difficult to grow SiC material of crystalline quality to meet requirements for a large scale industrial application, small-size and high-cost SiC wafers severely limit their applications at present [7]. The difference in the lattice parameters of the silicon carbide and monocrystalline silicon is ~20%, and the difference in their thermal expansion coefficients is ~8%. Therefore, the growth of epitaxial SiC layers on a Si substrate is a nontrivial problem [8, 9]. For example, by means of ion implantation [2, 5-8, 11, 12], ion-beam sputtering [13-15] or plasma enhanced chemical vapor deposition [8, 16] it is possible to obtain amorphous SiC films with subsequent crystallization during annealing (900-1300°C). Successes were achieved in the synthesis of thin epitaxial SiC films on Si by the substitution of atoms [9, 10, 17-19]. The method of magnetron sputtering has become widespread due to relatively high growth rates, good adhesion of SiC films and sufficiently low cost of the technological process [20-23]. In [20] magnetron sputtering of a two-component target, which is composed of separate parts of C and Si, is proposed. In general, at temperatures below 500 °C, the structure of SiC films is amorphous. In magnetron sputtering with direct current, polycrystalline fused targets of silicon and carbon are commonly used [21]. An alternative to using a fused target is sputtering a pure silicon target in a mixture of argon and

methane [22]. The resulting SiC films had a polycrystalline structure with nanometer-sized columnar grains. In [23], a method was proposed for depositing amorphous a-$Si_{1-x}C_x$ by means of radio-frequency magnetron sputtering of two or more targets.

In this work, the silicon carbide films on the surface of a thin layer of amorphous silicon grown on the surface of a single-crystal silicon substrate were synthesized by means of magnetron sputtering.

2 Materials and methods

The deposition of SiC films was carried out on the MAGNA TM-200-01 unit with the simultaneous sputtering of the silicon target and the graphite target in the high-frequency regime of 13.56 MHz at a power of 150 W. The gas Ar flow rate was 2.4 l/h, the chamber pressure – 0.4 Pa, the substrate temperature – 100°C, deposition time 2400 and 14400 s. Single-crystal silicon wafers of (100) orientation with dimensions 7×7×0.3 mm and resistivity 4-5 Ω·cm as substrates were used [11,12,13].

The composition and structure of the film after deposition and annealing at the temperature of 1100°C were investigated using IR spectrometer Nicolet iS-50 (Thermo Scientific, USA) [12,13].

Phase composition of the films was determined by highly sensitive X-ray diffraction using narrowly collimated (0.05 × 1.5 mm^2) CuK_α X-ray beam [11-13].

The density and thickness of the films had determined by X-ray reflectometry through registration of the angular dependence of the reflection coefficient using two spectral lines CuK_α (0.154 nm) and CuK_β (0.139 nm) on the installation Complexray C6 [12, 13, 24].

3 Results and discussion

The deposited films were investigated by X-ray reflectometry using two spectral lines CuK_α and CuK_β. According to the value of the critical angle of the total external reflection $2\theta_c = 0.51994°$ (Table 1, Figure 1b), the SiC_x film density was determined using the Henke program [25], which was 3.179 g/cm^3 and corresponds to the density of $SiC_{0.97}$ layer. The composition of the SiC_x layers can be determined approximately from the expression [12]:

$$x = x_1 + (\rho_x - \rho_1)\bullet(x_2 - x_1)/(\rho_2 - \rho_1), \qquad (1)$$

where $x_2 = 1$, $x_1 = 0$, $\rho_2 = 3.21$ g/cm^3, $\rho_1 = 2.33$ g/cm^3, $\rho_x = 3.179$ g/cm^3, $x = N_C/N_{Si} = 0.965$ and the density of the SiC_x layer is an intermediate value between the density of SiC (or Si_1C_1) and Si (or Si_1C_0). According to the formula $SiC_x = Si_{1-x/(1+x)}C_{x/(1+x)}$, the density corresponds to the composition $SiC_{0.965} = Si_{51}C_{49}$. The film thickness was about 166 nm (Table 2, Figure 1a).

Table 1 – Determination of the layer density ρ using the Henke program

Film	I_{max}, s^{-1}	$I_{max}/2$, s^{-1}	$2\theta_c$, degree	θ_c, degree	θ_c, mrad	ρ, g/cm^3
SiC_x	708339	354170	0,51994	0,25997	4,537	3,179

Table 2 – Determination of the layer thickness d by the formula $2d\cdot\sin\theta = \lambda$, or $d = \lambda/2\theta$

Film	$(2\theta)_j$, degree	$(2\theta)_i$, Degree	j – i	$2\theta_{av}=[(2\theta)_j - (2\theta)_i]/(j - i)]$, degree	λ, nm	d, nm
SiC_x	1,806	0,740	20	0,0533	0,15420	165,8
SiC_x	1,666	0,704	20	0,0481	0,13923	165,8

After annealing at the temperature of 1100°C for 30 minutes in Ar atmosphere, the density decreases up to 2.792 g/cm^3 (Table 3) and the layer thickness increases up to 174 nm (Table 4). The change in the film density and its composition to $SiC_{0.525} = Si_{66}C_{34}$ after annealing assumes that under the action of a high-frequency plasma of 13.56 MHz a structural phase of high density was precipitated, which decays after annealing.

In IR spectra, the presence of a wide SiC peak in the range 700-1030 cm-1 and SiO2 peak at 1100 cm^{-1} before and after annealing (Figure 2).

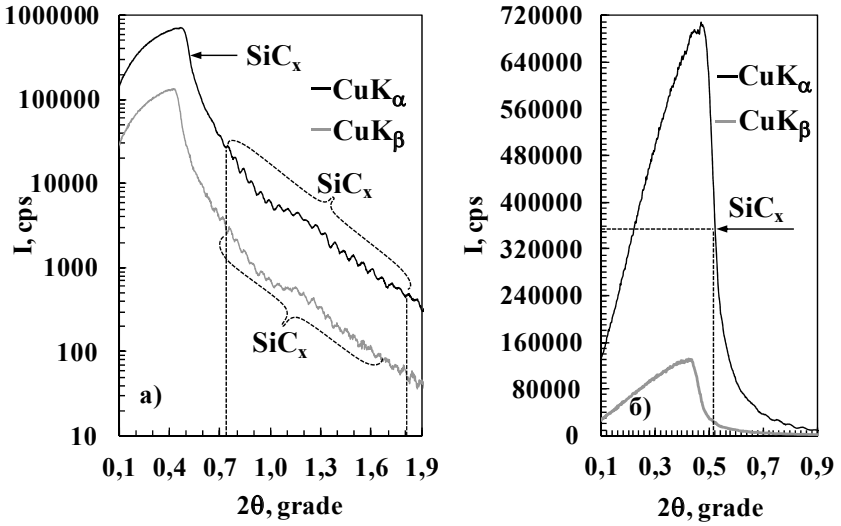

Figure 1 – X-ray reflectometry using two spectral lines of CuK_α (0.154 nm) and CuK_β (0.139 nm) of the SiC_x film synthesized on the surface of Si substrate by magnetron sputtering (150 W – rf, 2400 s, Ar – 2.4 l/h, 0.4 Pa , 100°C), in logarithmic (a) and natural (b) scales

Table 3 – Determination of the layer density ρ using the Henke program

Film	I_{max}, s^{-1}	$I_{max}/2$, s^{-1}	$2\theta_c$, degree	θ_c, degree	θ_c, mrad	ρ, g/cm^3
SiC_x	352693	176347	0,48730	0,24365	4,2525	2,792

Table 4 – Determination of the layer thickness d by the formula $2d \cdot \sin\theta = \lambda$, or $d = \lambda/2\theta$

Film	$(2\theta)_j$, degree	$(2\theta)_i$, Degree	j – i	$2\theta_{av}=[(2\theta)_j - (2\theta)_i]/(j - i)]$, degree	λ, nm	d, nm
SiC_x	1,834	0,820	20	0,0507	0,15420	174,3
SiC_x	1,706	0,748	21	0,04562	0,13923	174,9

The appearance of SiC(111) line of polycrystalline silicon carbide phase on the X-ray diffraction pattern (Figure 3) after annealing (1100°C, 30 min, Ar) was observed. The absence of SiO_2 lines indicates the absence of thick SiO_2 amorphous layer or SiO_2 crystallites. As a result, the SiO_2 peak of IR absorption corresponds to the natural oxide on the back surface of c-Si. Thus, the formation of a SiC film after deposition by magnetron sputtering in the high-frequency regime and annealing at 1100°C for 30 minutes is reliably shown.

Long-term deposition of SiC_x thick films on the c-Si surface using the MAGNA TM-200-01 unit with simultaneous sputtering of targets of silicon and graphite in the high-frequency regime of 13.56 MHz was carried out with parameters as follows: the magnetron power was 150 W, argon gas flow was 2.4 l/h, the pressure in the chamber was 0.4 Pa, the substrate temperature was 100°C, the sputtering time was 14400 s. It is shown by X-ray reflectometry that the film density corresponding to the critical angle of total external reflection θ_c = 0.25648° was 3.204 g/cm^3 (Figure 4b, Table 5) and is practically equal to the density of silicon carbide 3.21 g/cm^3. No intensity oscillations are observed (Figure 4a) due to an increase in the sputtering time by a factor of 6 and a thickness of up to 1 μm in comparison with a duration of 2400 s and a thickness of 165.8 nm (Table 2). X-ray reflectometer determines the film thickness in the range of 2-400 nm.

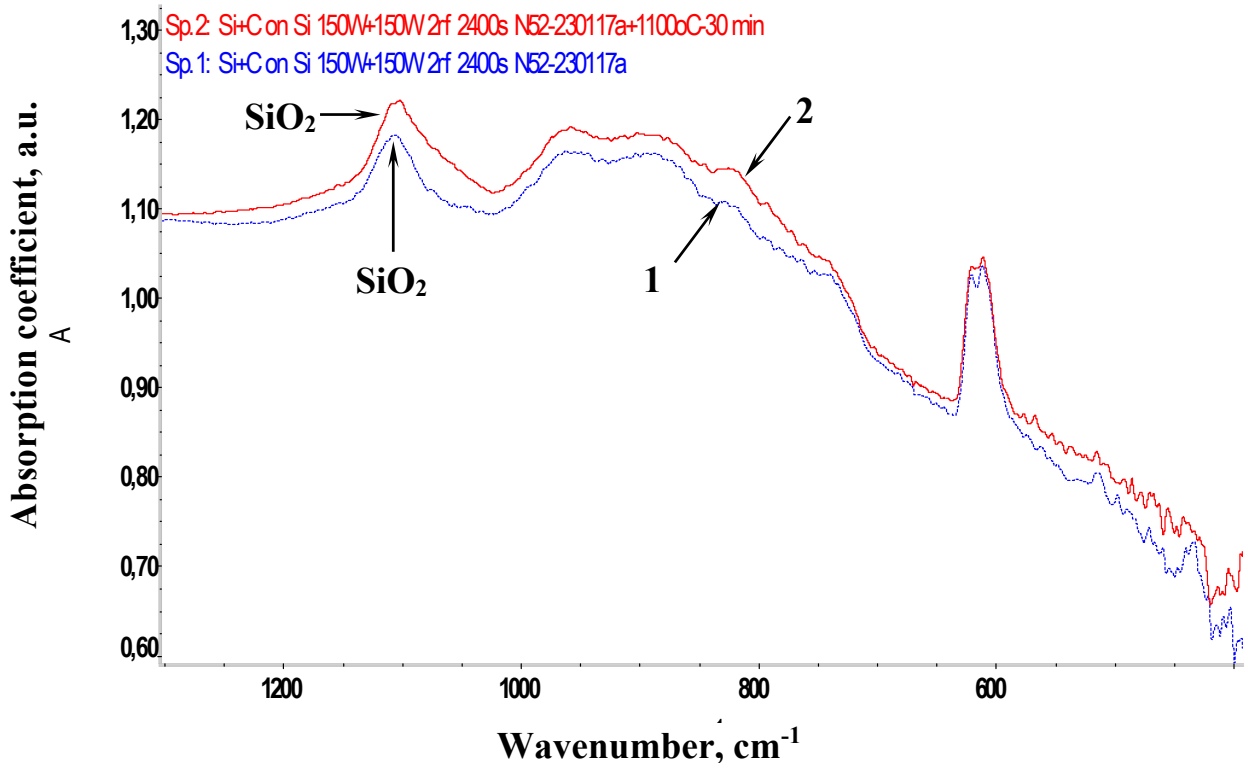

Figure 2 – IR absorption spectra of a SiC_x film synthesized on the surface of a Si wafer by magnetron sputtering (150 W, 2400 sec, Ar-2.4 L / h, 0.4 Pa): 1- after deposition, 2 – after annealing at 1100°C for 30 min (Ar)

Figure 3 – X-ray diffraction pattern of thin SiC_x film deposited by magnetron sputtering, after annealing at 1100°C for 30 min in an Ar atmosphere

In the IR spectrum of the film, a broad peak is observed in the region 440-1200 cm^{-1} with an amplitude of 0.220 a.u. and a half-width of 360 cm^{-1}, indicating the amorphous nature of the SiC film (Figure 5). Indeed, as shown in [12], for the ion-synthesized $SiC_{1.0}$ and $SiC_{1.4}$ layers, the half-width of the IR-transmission peak of the amorphous layer was 300 cm^{-1} with a maximum in the region of 700-795 cm^{-1}, i.e. below the value of 795.9 cm^{-1}, characteristic of tetrahedrally oriented Si-C bonds in β-SiC (or 799.5 cm^{-1} in 2H-SiC, 797.6 cm^{-1} in 4H-SiC, 797.0 cm^{-1} in 6H-SiC, 797.5 cm^{-1} in 15R-SiC). In Figure 5, a peak of SiO_2 with a maximum at 1100 cm^{-1} and an amplitude of 0.06 due to the presence of SiO_2 layer on the underside of the Si substrate, is also observed. A feature of the SiC peak is the location of the maximum in the 860 cm^{-1} region, suggesting the prevalence of truncated SiC bonds absorbing in the region above 795.9 cm^{-1}.

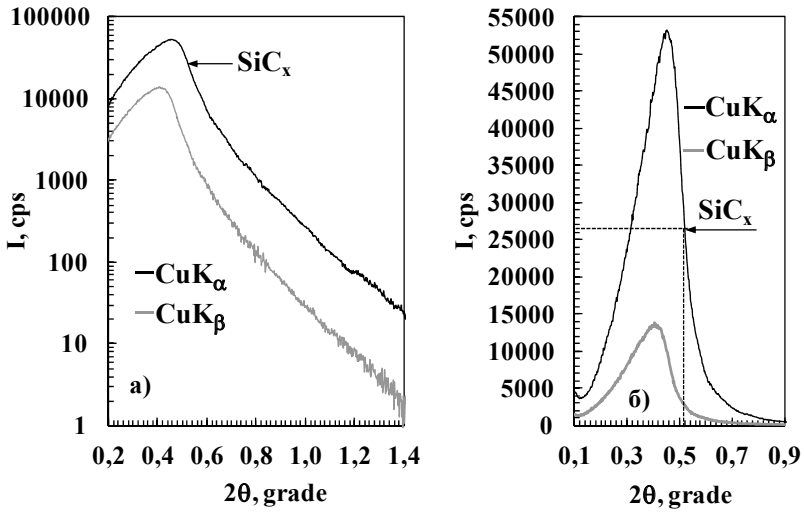

Figure 4 – X-ray reflectometry of a SiC_x film synthesized on the surface of a Si wafer by magnetron sputtering (150 W-rf, 14400 s, Ar-2.4 l/h, 0.4 Pa, 100°C), in logarithmic (a) and natural (b) scales

Table 5 – Determination of the layer density ρ using the Henke program

Film	I_{max}, c^{-1}	$I_{max}/2$, c^{-1}	$2\theta_c$, degree	θ_c, degree	θ_c, mrad	ρ, g/cm^3
SiC_x	53212	26606	0,51295	0,25648	4,476	3,204

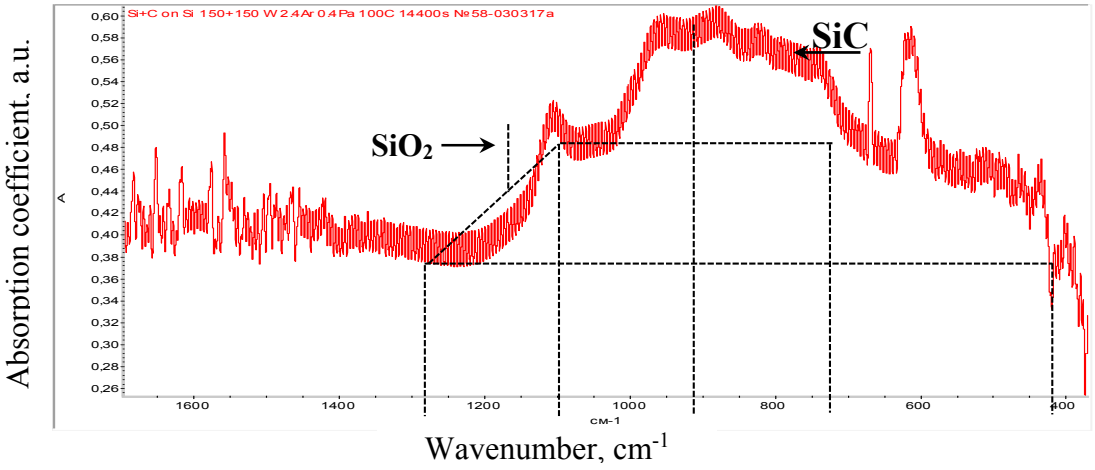

Figure 5 – IR absorption spectrum of a $SiC_{1.0}$ film deposited on the surface of a Si wafer by magnetron sputtering (150 W, 13,56 MHz, 14400 s, Ar-2.4 l/h, 0.4 Pa)

4 Conclusions

The synthesis of silicon carbide (SiCx) films on the surface of single-crystal silicon (c-Si) with a thin interlayer of amorphous silicon (a-Si) by magnetron sputtering. A principal difference between the method of synthesis and the traditionally used magnetron sputtering is the 13.56 MHz high-frequency magnetron sputtering of a silicon target and a graphite target. An amorphous $SiC_{0.97}$ film with a density of 3.179 g/cm^3 and 165 nm thick was obtained under the deposition regime: rf = 150 W, 13.56 MHz; Ar – 2.4 l/h, 0.4 Pa; 100°C, 2400 s; containing SiC nanocrystals after annealing (1100°C, 30 min, Ar). Synthesis of an amorphous SiC_x film with a density of 3.204 g/cm^3 at a long sputtering of Si and C targets – 14400 s, containing nanoclusters with a predominance of truncated SiC bonds, was carried out.

References

1 F. Liao, S.L. Girshick, W.M. Mook, W.W. Gerberich, M.R. Zachariah. Superhard nanocrystalline silicon carbide films // Appl. Phys. Lett. − 2005. – Vol. 86. − P**.** 171913−171915.

2 J.K.N. Lindner. High-dose carbon implantations into silicon: fundamental studies for new technological tricks // Appl. Phys. A. – 2003. – Vol. 77. – P. 27 – 38.

3 A.V. Afanas'ev, V. A. Il'in, A. V. Korlyakov, A. O. Lebedev, V. V. Luchinin,, Yu. M. Tairov, in Physics and Technology of Micro- and Nanosystems, Ed. By V. V. Luchinin and V.V. Malinovskii (Russkaya Kollektsiya, St. Petersburg, 2011). P. 50.

4 United State Patent. Heat resistant material and hot structure member both space shuttle, space shuttle, and method for producing heat resistant material for space shuttle / Oguri K., Sekigawa T. // Pub. № US 2004/0180242 A1.

5 H. Yan, B. Wang, X.M. Song, L.W. Tan, S.J. Zhang, G.H. Chen, S.P. Wong, R.W.M. Kwok, W.M.L. Leo. Study on SiC layers synthesized with carbon ion beam at low substrate temperature // Diamond and related materials. − 2000. – Vol. 9. − P. 1795−1798.

6 D. Chen, S.P. Wong, Sh. Yang, D. Mo. Composition, structure and optical properties of SiC buried layer formed by high dose carbon implantation into Si using metal vapor vacuum arc ion source // Thin Solid Films. − 2003. –Vol. 426. − P. 1−7.

7 Y. Liangdeng, S. Intarasiri, T. Kamwanna, S. Singkarat. // In book: Ion beam applications in surface and bulk modification of insulators. – Austria, Vienna: IAEA-TECDOC-1607. 2008. – P. 63.

8 L. Calcagno, P. Musumeci, F. Roccaforte, C. Bongiorno, G. Foti. Crystallization mechanism of amorphous silicon carbide // Appl. Surf. Sci.– 2001. –Vol. 184. – P. 123–127.

9 S.A. Kukushkin, A.V. Osipov. Topical review. Theory and practice of SiC growth on Si and its applications to wide-gap semiconductor films // *J. Phys. D Appl. Phys.* -2014. –Vol. 47. –P. 313001–313041.

10 S. A. Kukushkin, A.V. Osipov. New method for growing silicon carbide on silicon by solid-phase epitaxy: model and experiment // Phys. Solid State. – 2008. –Vol. 50 (7). –P. 1238–1245.

11 K.Kh. Nussupov, N.B. Beisenkhanov, I.V. Valitova, K.A. Mit', D.M. Mukhamedshina, E.A. Dmitrieva. Structure properties of carbon implanted silicon layers // J. of Materials Science: Materials in Electronics. − 2008. – Vol.19. − P. 254−262.

12 K.Kh. Nussupov, N.B. Beisenkhanov, S.K. Zharikov, I.K. Beisembetov, B.K. Kenzhaliev, T.K. Akhmetov, B.Zh. Seitov. Structure and composition of silicon carbide films synthesized by ion implantation // Phys. Solid State. – 2014. – Vol. 56(11). – P. 2307–2321.

13 I.K. Beisembetov, K.Kh. Nusupov, N.B. Beisenkhanov, S.K. Zharikov, B.K. Kenzhaliev, T.K. Akhmetov, B.Zh. Seitov. Synthesis of SiC thin films on si substrates by ion-beam sputtering // Journal of Surface Investigation. X-ray, Synchrotron and Neutron Techniques. – 2015. – Vol. 9. -No.2. – P. 392-399.

14 A. Valentini, A. Convertino, M. Alvisi, R. Cingolani, T. Ligonzo, R. Lamendola, L. Tapfer. Synthesis of silicon carbide thin films by ion beam sputtering // Thin Solid Films. – 1998. – Vol. 335 (1–2). – P. 80-84.

15 K. Volz, M. Kiuchi, M. Okumura, W. Ensinger. C–SiC–Si gradient films formed on silicon by ion beam assisted deposition at room temperature. // Surface and Coatings Technology. – 2000. – Vol. 128–129. – P. 274-279.

16 Y. Sun, T. Miyasato, J.K. Wigmore, N. Sonoda, Y. Watari. Characterization of 3C-SiC films grown on monocrystalline Si by reactive hydrogen plasma sputtering. // Journal of Applied Physics. – 1997. – Vol. 82 (5). – P. 2334-2341.

17 S.A. Kukushkin, A.V. Osipov, N.A. Feoktistov. Synthesis of epitaxial silicon carbide films through the substitution of atoms in the silicon crystal lattice: a review. // Phys. Solid State. – 2014. – Vol.56 (8). – P. 1507–1535.

18 S.A. Kukushkin, K.Kh. Nusupov, A.V. Osipov, N.B. Beisenkhanov and D.I. Bakranova. X-Ray Reflectometry and Simulation of the parameters of SiC epitaxial films on Si(111), grown by the atomic substitution method. // Physics of the Solid State. – 2017. – Vol. 59 (5). – P. 1014–1026.

19 Kukushkin S.A., Nussupov K.Kh., Osipov A.V., Beisenkhanov N.B., Bakranova D.I. Structural properties and parameters of epitaxial silicon carbide films, grown by atomic substitution on the high-resistance (111) oriented silicon // Superlattices and Microstructures. – 2017. – Vol. 111. – P.899-911.

20 V.I. Perekrestov, A.S. Kornyushchenko, I.V. Zahaiko. Polucheniye plenok karbida kremniya metodom magnetronnogo raspyleniya sostavnoy uglerod-kremniyevoy misheni (Formation of silicon carbide films by magnetron sputtering of compound carbon-silicon target) // Zhurnal nano- i elektronnoĭ fiziki. – 2015. – Vol. 7 (2). – P. 02016 (in Russian).

21 S.M. Rajab, I.C. Oliveira, M. Massi, H.S. Maciel, S.G. dos Santos Filho, R.D. Mansano. Effect of the thermal annealing on the electrical and physical properties of SiC thin films produced by RF magnetron sputtering. // Thin Solid Films.– 2006. – Vol. 515. – 170-175.

22 Y.M. Lei, Y.H. Yu, C.X. Ren, S.C. Zou, D.H. Chen, S.P. Wong, I.H. Wilson. Compositional and structural studies of DC magnetron sputtered SiC films on Si(111). // Thin Solid Films.– 2000. – Vol. 365. – P. 53-57.

23 Y.-H. Joung, H.I. Kang, J.H. Kim, H.-S. Lee, J. Lee, W.S. Choi. SiC formation for a solar cell passivation layer using an RF magnetron co-sputtering system // Nanoscale Res. Lett. – 2012. – Vol. 7(1). –P. 22.

24 A. G. Touryanski, A. V. Vinogradov, I. V. Pirshin, X-ray reflectometer. US Patent No. 6041098 (2000).

25 B.L. Henke, E.M. Gullikson, J.C. Davis. X-ray interactions: photoabsorption, scattering, tansmission, and reflection at E = 50-30,000 eV, Z = 1-92 // Atomic Data and Nuclear Data Tables. – 1993.– Vol.54 (2). – P. 181-342.

IRSTI 29.31.23

Ion-beam formation of light-emitting structures based on silicon nitride layers on silicon

Murzalinov D.[1*], Vlasukova L.[2], Parkhomenko I.[2],
Komarov F.[2] and Akilbekov A.[3]

[1]*Saken Seifullin Kazakh Agrotechnical University, Zhenis ave., 62, Astana, 010011, Kazakhstan*
[2]*Belarus State University, Nezavisimosti ave. 4, Minsk, 220030, Belarus*
[3]*L.N. Gumilyov Eurasian National University, Satpayev str., 2, Astana, 010008, Kazakhstan*
[*]*e-mail: dan_collaps@mail.ru*

The paper shows the advantage of silicon nitride for use as a light-emitting element in integrated circuits. Along with this, the chosen methods for obtaining the studied samples enable us to determine all possible causes responsible for radiative recombination. The effect of irradiation with Xe^+ ions of 200 MeV in the dose range $10^9 – 10^{14}$ ions/cm^2 on the optical properties and the structure of silicon enriched silicon nitride (SRN) films deposited on the Si substrate by chemical vapor deposition under low pressure was studied. Based on the Raman scattering (RS) data, it was concluded that the irradiation by 200 MeV Xe ions with a dose of 1×10^{14} ions/cm^2 leads to the dissolution of the amorphous Si phase in the nitride matrix. According to the results of transmission electron microscopy, preliminary irradiation with swift heavy ions (SHI) enhances the phase separation process in the nitride layer with a 22% excess of Si during the subsequent annealing at 1100°C for 60 minutes. The SHI irradiation, followed by the heat treatment, leads to a further increase in the intensity of the photoluminescence (PL) in the spectral range 600–750 nm compared with that in case of annealed films without preliminary irradiation. It is known that radiation in this spectral range is due to Si nanocrystals (Si NCs).

Key words: Si-rich SiN_x/Si, nanoclusters, swift heavy ions, photoluminescence, K-centers.
PACS numbers: 79.20.Rf, 78.55.−m.

1 Introduction

The physical fundamentals of the development of new materials and technologies are currently in the center of attention for many researchers. By controlling the size of the structural components of a material, it becomes possible to produce qualitatively new electronic devices.

The radiative properties of silicon nanoparticles in the visible range are of the considerable interest.

Despite the advances in the study of the light-emitting system "Si nanocrystals in a SiO_2 matrix" [1-3], many authors believe that silicon dioxide is not the best matrix to obtain luminescence. The Si_3N_4 matrix is more preferable for the formation of silicon nanocrystals arrays.

Silicon nitride is one of the main dielectrics in integrated circuits with a band gap of ~ 5.3 eV. This material is more suitable for the development of electroluminescent devices compared to SiO_2 (E_g=8.2eV).

Initially, the interest to the light-emitting properties of silicon nitride arose during the formation of the system "Si nanoclusters in a dielectric matrix" on its basis. Indeed, such a system exhibits intensive luminescence. However, the silicon nitride matrix luminesces itself, and the nature of this radiation is being widely discussed in the literature.

In connection with the foregoing, in this work, it seems appropriate to expand research in the field of creating a light-emitting structure based on silicon nitride enriched with silicon.

2 The structure of crystalline and amorphous Si_3N_4

Silicon nitride is a refractory compound with a predominantly covalent type of bonds. Si_3N_4 is a polymorphic compound that exists in three modifications. In the crystalline state, there are two hexagonal phases: α- and β-Si_3N_4 (Figure 1), with the structure

of phenacite [4]. At temperatures below 1150°C, the β-phase is stable; at higher temperatures, the α-phase is stable. The density of these phases is almost the same 3.1-3.2 g·cm^{-3}.

The cubic γ-modification was obtained at a pressure of 15 GPa and a temperature above 1700°C by the method of laser heating in a diamond cell. In the literature, this modification is referred to as the c-modification. It has a spinel-type structure in which two silicon atoms have an octahedral coordination with six nitrogen atoms, one silicon atom is coordinated tetrahedrally with four nitrogen atoms (Figure 2). It is theoretically shown that this structure should have a high hardness, similar to that of a diamond and c-BN [4-8].

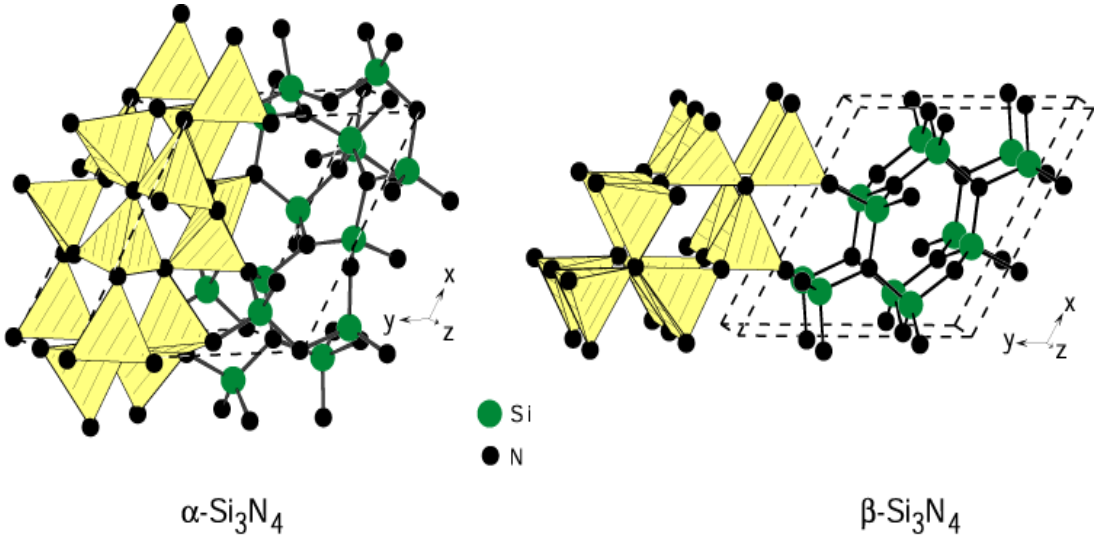

Figure 1 – α-Si_3N_4 and β-Si_3N_4 unit cells

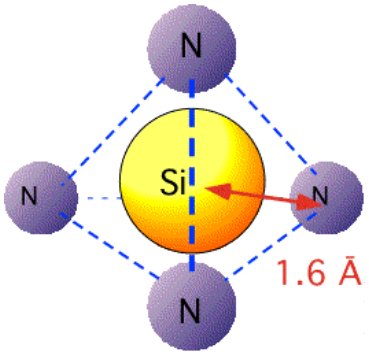

Figure 2 – The main structural unit of Si_3N_4

In the work [ref.] Gritsenko V.A. reports the parameters of elementary cells of α- and β-modifications. The unit cell of α-Si_3N_4 contains 28 atoms (12 Si and 16N) and has lattice constants a = 7.75 Å and c = 5.62 Å. The β-Si_3N_4 cell contains 14 atoms (6 Si and 8 N), the lattice constants, a = 7.71 Å, c = 2.91 Å. By the symmetry, α-Si_3N_4 is referred to P31c space group, β-Si3N4 – P63/m. Both phases have a tetrahedral structure.

Non-stoichiometric silicon nitride (SiN_x) differs from stoichiometric nitride (Si_3N_4) by the amount of excess silicon in the composition (Si_{exc}) [9].

$$Si_{exc.} = \frac{Si_{at.\%}}{Si_{at.\%}+N_{at.\%}} - \frac{3}{7} \qquad (1)$$

3 Luminescence of defects. Edge luminescence

In recent years, a number of studies have appeared in which PL of silicon nitride is associated with radiative transitions between the energy levels of defects [10–15].

In this case, the K- and N- centers act as the main centers of radiative recombination. The K-center is an intrinsic defect in the silicon nitride matrix, which is a silicon atom bound to three nitrogen atoms (N3≡Si •). The presence of K-centers in the silicon nitride matrix can lead to luminescence in the range of 2.5±0.1 eV (478–517 nm). The N-center is a two-coordinated nitrogen atom (Si2 = N •).

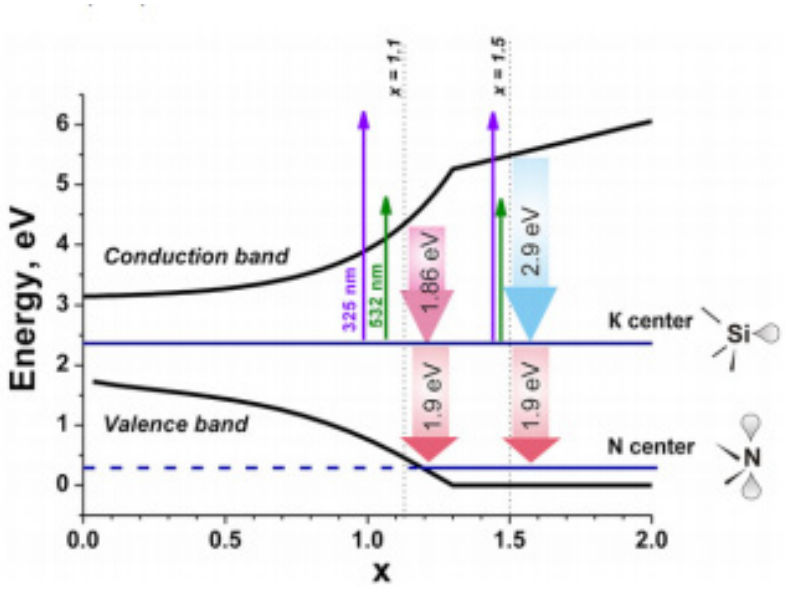

Figure 3 – Model of possible optical transitions based on the Robertson's band diagram for amorphous SiN_x

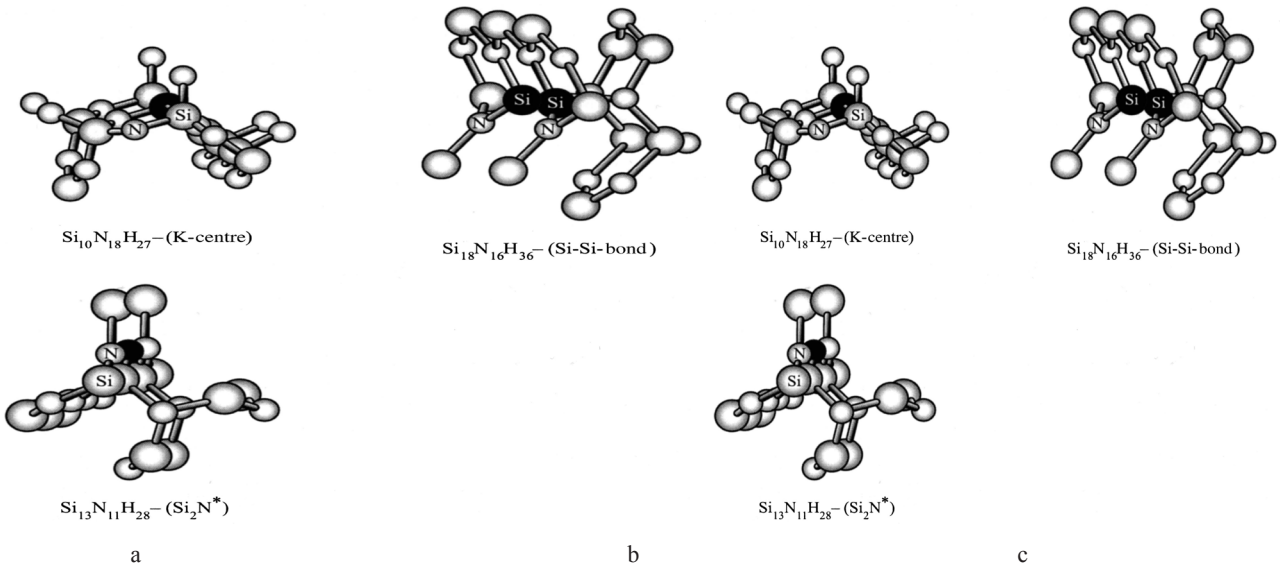

a – $Si_{10}N_{18}H_{27}$-(K-center); b – $Si_{18}N_{16}H_{36}$-(Si-Si-bond); c – $Si_{13}N_{11}H_{28}$-(Si_2N*)

Figure 4 – Models of defects in silicon nitride.

Models of the centers are shown in Figure 4.

These centers are already present in the initial silicon nitride films, but their number increases noticeably after high-temperature annealing as a result of the dissociation of the N-H bonds [16, 17].

The energy of electronic transitions with the participation of K-centers is 2.1–2.6 eV; therefore, the luminescence in the green region (470–590 nm) is often attributed to the K-centers [18, 19].

In the model of edge luminescence, there is a process of transition of excited carriers to neighboring localized states with lower energy, followed by the light emission. In amorphous materials, there is only a short-range order. Therefore, in these materials, one can observe new phenomena, which are explained by the presence of localized electronic states. The energy levels of these localized states lie near the bands' edges, expanding them into the region of

the bandgap. The formation of localized states in amorphous silicon nitride, in contrast to crystalline states, leads to a higher photosensitivity and the appearance of PL due to radiative recombination of charges localized at the band edges [20-23].

This model was quite successfully applied to explain PL and its shift with increasing concentration of Si in SRN films, in which Si nanoclusters were not detected by high-resolution transmission electron microscopy (TEM). Using this model, researchers managed to explain the position of the PL band and the change in the PL intensity depending on the composition of the nitride film [24-28].

The intensity and the spectral range of PL in silicon nitride films strongly depend on the regimes and conditions of deposition, as well as on subsequent heat treatments.

4 Experiment

The silicon nitride film was deposited on a Si (100) n-type substrate by chemical vapor deposition at low pressure from a gas mixture of dichlorosilane (SiH_2Cl_2) and ammonia (NH_3). The temperature of the substrate during the deposition was 800°C. The SiH_2Cl_2/NH_3 ratio was changed during the deposition process to form a nitride film consisting of two layers with a different stoichiometric parameter "x". The composition of as-deposited SiNx films was determined by Rutherford backscattering spectrometry using 1.3 MeV He+ ions from the HVE AN-2500 accelerator. It was done to compare the effects of thermal annealing and swift heavy ion irradiation on SiN_x matrix. The refractive index of the nitride film, measured by laser ellipsometry, is 2.22. Samples of SiN_x/Si structure with size of 1×1 cm^2 were cut out and irradiated on a DC-60 cyclotron (Astana, Kazakhstan) with 200 MeV Xe ions in the dose range 10^9-10^{14} ions/cm^2. The structural characteristics of the as-deposited and annealed silicon nitride films were investigated by transmission electron microscopy in the "cross-section" geometry (XTEM) using a Hitachi H-800 microscope operated at 200 keV. Some samples were annealed in a nitrogen atmosphere at 1100°C for 60 min in a furnace with resistive heating.

5 Results and Discussion:

To determine the composition of the initial films, the Rutherford backscattering method was used.

In Figure 5, which represents the dependence of the concentrations of Si and N atoms on the layer depth, one can see the two regions with different Si/N ratio. The surface layer of the nitride is characterized by "x" =0.54 ($SiN_{0.54}$). This corresponds to the silicon excess (Si_{exc}) ≈22%. Beneath this region, there is a layer with "x"=1.0 ($SiN_{1.0}$), where the level of silicon excess is ≈7%.

The existence of the two layers in the studied nitride film is proved by the data of transmission electron microscopy. Figures 6-8 show TEM images of (vertical) cross section of the "deposited sample", as well as samples after heat treatment and after Xe^+ ion irradiation with subsequent annealing.

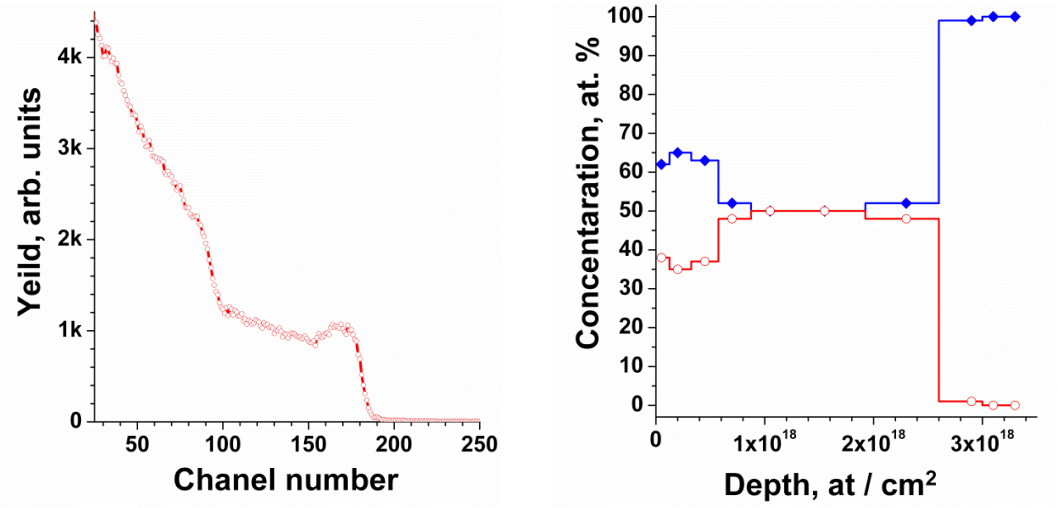

a b

a – RBS spectrum of SiNx film, b – calculated distribution profiles of Si (blue) and N (red).

Figure 5 – Rutherford backscattering spectrum of the SiN_x film

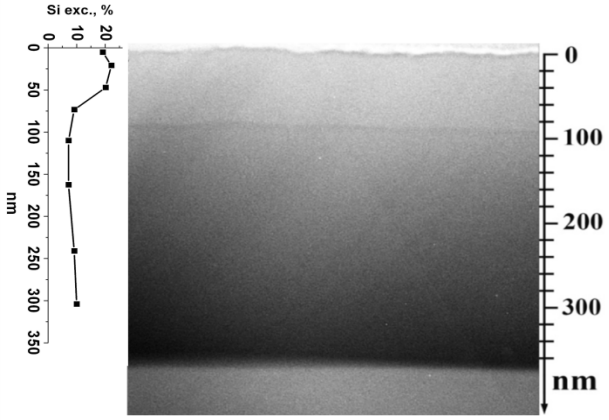

Figure 6 – TEM image of the silicon nitride film. Left part of the TEM image shows the distribution of Si excess (given in %) by depth from RBR data

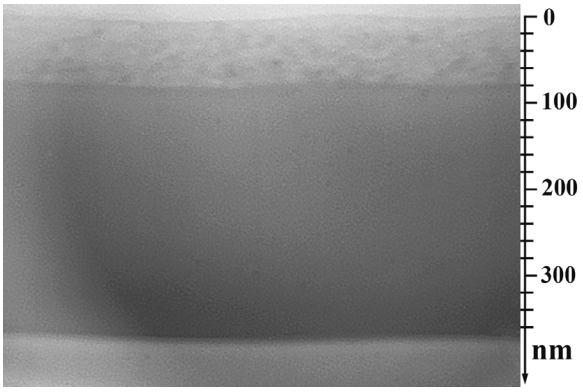

Figure 7 – TEM image of cross section of the silicon nitride film after annealing at 1100°C, 60 min

On TEM image, the two layers are clearly seen: the surface layer with thickness ~80 nm and a layer beneath it – the second one with thickness ~290 nm (Figure 6).

Annealing leads to the formation of inclusions with dark contrast within the surface layer of the nitride (Figure 7).

Taking into consideration the high level of Si excess in this region (≈22%), it can be concluded that these inclusions are crystalline precipitates of Si. It is known that high-temperature annealing of Si-reach SiN_x films leads to the formation of silicon nanocrystals embedded in a nitride matrix [29, 30].

It should be noted the absence of any inclusions in the deeply-lying second nitride layer with excessive Si ≈7%.

Figure 8 shows the effects of heat treatment and the combined processing of SHI irradiation with subsequent annealing on the structure of the nitride film.

It can be seen that in case of the sample irradiated with swift heavy ions before the heat treatment, the inclusions become darker and clearly visible comparing to that in the sample after annealing.

In order to determine the phase state of the studied samples before and after irradiation with swift heavy ions the method of Raman spectroscopy (RS) was used. Figure 9 shows the RS spectra of the sample immediately after the nitride deposition and the samples after irradiation with Xe^+ ions.

The RS spectra of the nitride films contain a few bands with maxima at ~180 and ~ 480 cm^{-1}, as well as weak lines in the frequency region of 300-400 cm^{-1}. These bands are due to the scattering on amorphous phase of Si.

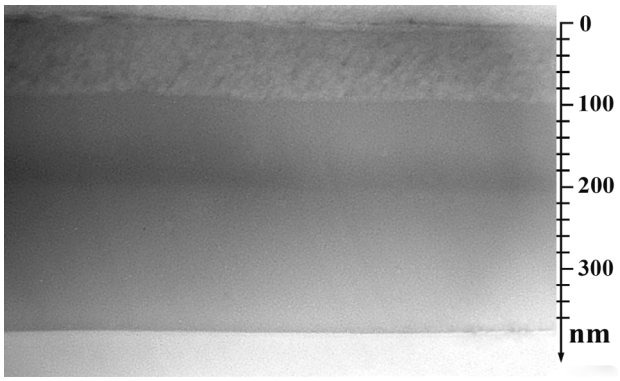

Figure 8 – TEM image of the nitride film after irradiation with Xe^+ (200 MeV, 10^{14}) with subsequent annealing

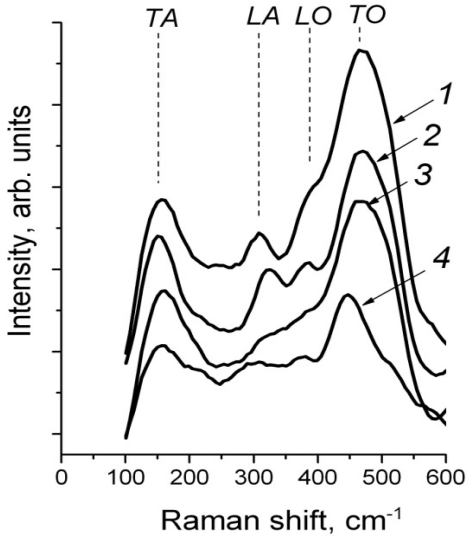

1 – initial; 2 – 10^9 ions/cm^2; 3 – 10^{12} ions/cm^2; 4 – 10^{14} ions/ cm^2

Figure 9 – RS spectra (λ_{exc}=355 nm) of initial sample and samples irradiated with Xe^+ ions

According to data in works [31, 32], spectra of amorphous Si demonstrate intensive bands of transverse acoustic (TA), longitudinal acoustic (LA) and transverse optical (TO) phonons with maxima at 150, 310 and 480 cm^{-1}, respectively.

The spectra also contain weak signal from the longitudinal optical phonon (LO) in form of a shoulder at 370 cm^{-1}. Thus, it can be concluded that there are amorphous silicon clusters in the samples.

The increase of irradiation dose from 10^9 to 10^{12} ions/cm^2 leads to the decrease of intensity of the bands referred to amorphous phase of silicon. The increase of the ion dose up to 10^{14} ions/cm^2 leads to extinction of the signal from amorphous phase of Si in RS spectrum. It can be explained by the dissolution of amorphous Si clusters within the nitride matrix as a result of SHI irradiation.

Characters of luminescence of amorphous and crystalline silicon nitride differ sufficiently. To study the radiation properties of these samples we analyse photoluminescence spectra (PL), excited by UV-laser with the wavelength of 325 nm (3.8 eV).

For the sample after deposition of nitride film, the photoluminescence spectrum was not registered. Figure 10 shows PL spectra of initial and irradiated samples after annealing, which were registered under UV-laser excitation.

As it is seen in Figure 10, a wide band of a complex form in the green-blue spectral region with the maximum at 440 nm dominates in the spectrum. This band can be connected with radiative recombination of carriers on K- and N- radiative centers. The existence of such defects leads to the emission of photons with energy of 3±0.1 eV (400-427 nm). Thus, the complex form of the green-blue band is explained by the contribution of intrinsic defects of silicon nitride into radiative recombination.

Irradiation with swift heavy ions with doses 10^{12} ions/cm^2 and higher leads to the PL quenching. However, blue radiation can partly be recovered by the heat treatment after irradiation.

For deeper understanding of the light-emitting mechanism of "complex" samples, it is required to study photoluminescence excited with lasers of the different wavelength.

With this purpose, the PL was excited with green laser (λ = 532 nm). Under this excitation energy (2.33 eV) the contribution from Si nanocrystals becomes dominant in the luminescence (Figure 11).

It is seen that in the PL spectrum of the Si-reach silicon nitride films there is a domination of a wide "red" band with the maximum at ~700 nm, which can be referred to the recombination of excitons in Si nanoclusters.

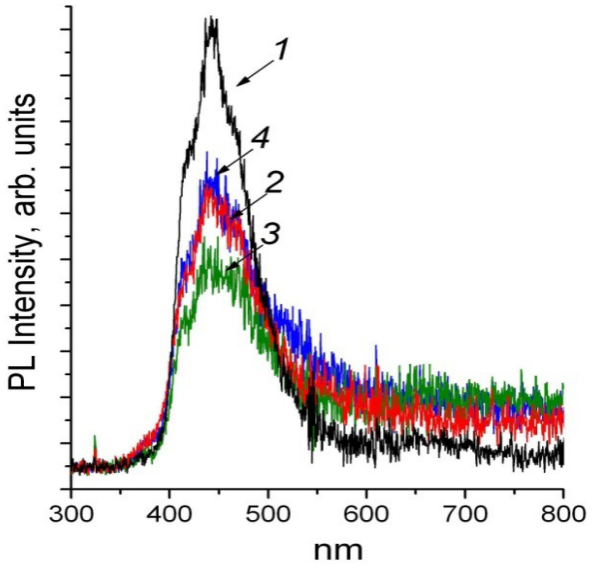

initial; 2 – 10^9 ions/cm^3; 3 – 10^{12} ions/cm^2; 4 – 10^{14} ions/cm^2. PL spectra were obtained under UV-laser excitation (λ = 325 nm)

Figure 10 – PL spectra of initial samples and samples irradiated with SHI Xe^+ and annealed (1000°C, 60 min).

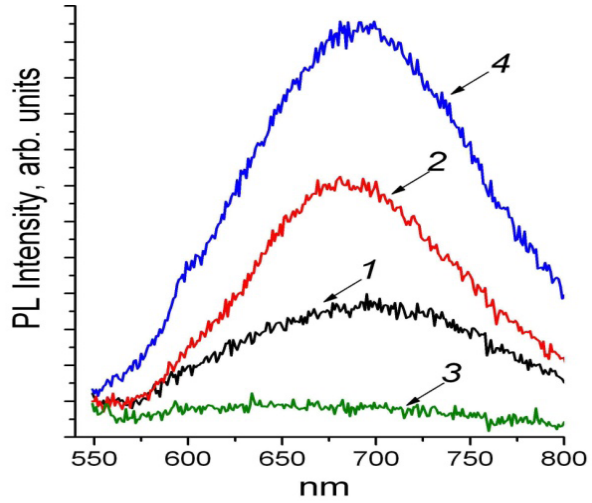

1 – initial sample; 2 – initial sample after annealing (1100°C, 60 min); 3 – sample after irradiation with swift Xe^+ ions with dose 10^{14} ions/cm^2; 4 – sample after irradiation with swift Xe^+ ions with dose 10^{14} ions/cm^2 and subsequent annealing (1100°C, 60 min)

Figure 11 – PL spectra of the Si-reach SiN_x/Si samples, obtained at green excitation (532 nm).

The annealing leads to the increase of PL intensity. This can be explained by the crystallization of Si clusters. As it is seen from Figure 11, SHI

irradiation leads to luminescence quenching. It agrees with the RS data about the dissolution of amorphous Si clusters in the nitride matrix as a result of SHI irradiation.

However, SHI irradiation with subsequent heat treatment leads to the stronger effect of the PL intensity increase, compared to that in case of annealed films without preliminary irradiation. This additionally proves the assumption that preliminary irradiation with heavy ions enhances the process of phase separation in the surface layer of the nitride with high Si excess during the heat treatment.

6 Conclusion

Using Raman spectroscopy it was shown that irradiation with swift heavy Xe ions with energy 200 MeV and dose 1×10^{14} ions/cm^2 leads to the dissolution of amorphous phase of Si in the silicon nitride matrix. By TEM analysis it was revealed that preliminary irradiation with swift heavy ions enhances the process of phase separation in the nitride layer with Si excess of 22% during the annealing at 1100°C for 60 min. It was also shown that SHI irradiation causes the PL quenching in the visible range in the nitride film.

Irradiation with swift heavy ions with subsequent heat treatment leads to the stronger effect of the increase of PL intensity in the spectral range 600-750 nm comparing to that in case of annealed films without preliminary irradiation. It is known that radiation in this spectral range is caused by Si nanocrystals. Therefore, preliminary irradiation enhances the process of crystallization of amorphous Si clusters within the nitride layer with high Si excess during the heat treatment.

Acknowledgement

The authors are grateful to MSc Nemkayeva R.R. for helpful discussions during preparation of this paper

References

1 L.Pavesi, D.J. Lockwood Silicon photonics/ ed. by L. Pavesi. – Berlin: Springer, 2004. – 398 p.

2 C.-F.Wang, M.P.Sarparanta, E.M. Mäkilä et al. Multifunctional porous silicon nanoparticles for cancer theranostics // Biomaterials. – 2015. – Vol. 48. – P. 108-118.

3 L.Pavesi, L.Dal Negro, C.Mazzoleni et al. Optical gain in silicon nanocrystals // Nature. – 2000. – Vol. 408, -No. 6811. – P. 440-444.

4 R.A.Andriyevsky, I.I.Spivak. Silicon nitride and materials based on it. Moscow: Metallurgiya, 1984. – 136 P. (in Russian)

5 Y.Roizin, V.Gritsenko. ONO structures and oxynitrides in modern microelectronics: material science, characterization and application. In dielectric films for advanced microelectronics. – Chichester: John Wiley & Sons, 2007. – P. 251-297.

6 A.V. Rzhanov. Silicon nitride in electronics. – Novosibirsk: Nauka, 1982. – 197 P. (in Russian)

7 A.Zerr, G.Miehe, G.Serghiou et al. Synthesis of cubic silicon nitride // Nature. – 1999. – Vol. 400, №6742. – P. 340-342.

8 A.S. Yunoshev. Shock wave synthesis of cubic silicon nitride // Fizika goreniya i vzryva. – 2004. – V.40, №3. – P. 132-135. (in Russian)

9 P.R.J.Wilson, T.Roschuk, K.Dunn et al. Effect of thermal treatment on the growth, structure and luminescence of nitride-passivated silicon nanoclusters // Nanoscale research letters. – 2011. – Vol. 6, – No.1. – P. 168-180.

10 M.Wang, D.Li, Z.Yuan, D.Yang, D.Que. Photoluminescence of Si-rich silicon nitride: Defect-related states and silicon nanoclusters // Applied physics letters. – 2007. – Vol. 90, – No. 13. – P. 131903.

11 S.Jang, M.Han. RF power control for fabricating amorphous silicon nitride without Si-nanocrystals and its effect on defects and luminescence // Journal of Alloys and Compounds. – 2014. – Vol. 614. – P. 102-106.

12 C.Ko, J.Joo, M.Han, B.Y.Park, J.H.Sok, K.Park. Annealing effects on the photoluminescence of amorphous silicon-nitride films // Journal-Korean Physical Society. – 2006. – Vol. 48. -No.6. – P. 1277.

13 R.Kumar Bommali, S.Preet Singh, S.Rai et al. Excitation dependent photoluminescence study of Si-rich a-SiNx: H thin films // Journal of Applied Physics. – 2012. – Vol. 112. –No.12. – P. 123518.

14 D.Li, F.Wang, D.Yang, D.Que. Electrically tunable electroluminescence from SiNx-based light-emitting devices // Optics express. – 2012. – Vol. 20. –No.16. – P. 17359-17366.

15 S.V.Deshpande, E.Gulari, S.W.Brown, S.C. Rand. Optical properties of silicon nitride films deposited by hot filament chemical vapor deposition // Journal of Applied Physics. – 1995. – Vol. 77. – No. 12. – P. 6534-6541.

16 B.Yan, J.H.D.da Silva, P.C. Taylor. Defect structure in nitrogen-rich amorphous silicon nitride films // Journal of non-crystalline solids. – 1998. – Vol. 227. – P. 528-532.

17 J.Kanicki, W.L.Warren, C.H.Seager, M.S.Crowder, P.M. Lenahan. Microscopic origin of the light-induced defects in hydrogenated nitrogen-rich amorphous silicon nitride films // Journal of non-crystalline solids. – 1991. – Vol. 137. – P. 291-294.

18 L.Zhang, H.Jin, W.Yang, Z.Xie, H.Miao, L. An Optical properties of single-crystalline α-Si 3 N 4 nanobelts // Applied physics letters. – 2005. – Vol. 86, №6. – P. 061908.

19 R.Huang, J.Song, X.Wang et al. Origin of strong white electroluminescence from dense Si nanodots embedded in silicon nitride // Optics letters. – 2012. – Vol. 37. -No4. – P. 692-694.

20 M.Wang, M.Xie, L.Ferraioli, Z.Yuan, D.Li, D.Yang, L.Pavesi Light emission properties and mechanism of low-temperature prepared amorphous SiN X films. I. Room-temperature band tail states photoluminescence // Journal of Applied Physics. – 2008. – Vol. 104. –No.8. – P. 083504-1-083504-4.

21 D.Engemann, R.Fischer. Photoluminescence in amorphous silicon // physica status solidi (b). – 1977. – Vol. 79. –No.1. – P. 195-202.

22 S.Zhang, G.Kong, Y.Wang, S.Sheng, X. Liao. Structural characterization of stable amorphous silicon films // Solid state communications. – 2002. – Vol. 122. –No.5. – P. 283-286.

23 J.Kistner, X.Chen, Y.Weng et al. Photoluminescence from silicon nitride-no quantum effect // Journal of Applied Physics. – 2011. – Vol. 110. –No.2. – P. 023520.

24 X.Zeng, W.Liao, G.Wen, X.Wen, W.Zheng. Structural evolution and photoluminescence of annealed Si-rich nitride with Si quantum dots prepared by plasma enhanced chemical vapor deposition // Journal of Applied Physics. – 2014. – Vol. 115. –No.15. – P. 154314-1-154314-6.

25 B.Sain, D.Das. Tunable photoluminescence from nc-Si/a-SiN x: H quantum dot thin films prepared by ICP-CVD // Physical Chemistry Chemical Physics. – 2013. – Vol. 15.-No.11. – P. 3881-3888.

26 P.D.Nguyen, D.M.Kepaptsoglou, Q.M. Ramasse et al. Impact of oxygen bonding on the atomic structure and photoluminescence properties of Si-rich silicon nitride thin films // Journal of Applied Physics. – 2012. – Vol. 112. –No.7. – P. 073514-1-073514-10.

27 D.S.Chao, J.H. Liang. Annealing temperature dependence of photoluminescent characteristics of silicon nanocrystals embedded in silicon-rich silicon nitride films grown by PECVD // Nuclear Instruments and Methods in Physics Research Section B: Beam Interactions with Materials and Atoms. – 2013. – Vol. 307. – P. 344-348.

28 H.L.Hao, L.K.Wu, W.Z.Shen, H.F. Dekkers. Origin of visible luminescence in hydrogenated amorphous silicon nitride // Applied Physics Letters. – 2007. – Vol. 91. –No.20. – P. 201922.

29 Y.Q.Wang, G.L.Kong, W.D. Chen et al. Getting high-efficiency photoluminescence from Si nanocrystals in SiO 2 matrix // Applied physics letters. – 2002. – Vol. 81. –No.22. – P. 4174-4176.

30 C.Liu, C.Li, A.Ji, L.Ma, Y.Wang, Z.Cao. Intense blue photoluminescence from Si-in-SiN_x thin film with high-density nanoparticles // Nanotechnology. – 2005. – Vol. 16. –No.6. – P. 940-943.

31 Jr.J.E.Smith, M.H.Brodsky, B.L.Crowder, M.I.Nathan, A.Pinczuk. Raman spectra of amorphous Si and related tetrahedrally bonded semiconductors // Physical Review Letters. – 1971. – Vol. 26. No.11. – P. 642-646.

32 A.A.Sirenko, J.R.Fox, I. A. Akimov et al. In situ Raman scattering studies of the amorphous and crystalline Si nanoparticles // Solid state communications. – 2000. – Vol. 113. –No.10. – P. 553-558.

IRSTI 29.19.22

Graphene produced by carbon diffusion through nickel foil

G.W. Beall*, T.K. Kuanyshbekov and M.A. Tulegenova

Texas State University, 601 University dr., San Marcos, TX 78666-4684, USA
e-mail: gb11@txstate.edu

This paper presents results of obtaining graphene and few-layer graphene nanostructures by unconventional method consisting in the diffusion of carbon through a thin nickel foil. The production of graphene and few-layer graphene nanostructures by the diffusion method was carried out under high vacuum conditions, with resistive heating of nickel. The growing method presented by us makes it possible to control the process of graphene formation by changing parameters such as: temperature, time and thickness of nickel. Data on the time dependence of the diffusion process on the nickel thickness and temperature are given. From the obtained experimental data was found the parameters determining the diffusion dynamics: E_a - the activation energy and concentration diffusion coefficient. The obtained samples were investigated by optical and electron microscopy, as well as by Raman spectroscopy. The experimental results are in good agreement with the theoretical Arrhenius relation, which confirms the diffusion nature of the process.

Keywords: carbon, graphene, few-layer graphene, diffusion.
PACS number(s): 68.65.Pq.

1 Introduction

Graphene attracts wide attention due to its physical and mechanical properties, and also represents a huge potential for various scientific and practical applications. Graphene is characterized as a two-dimensional sheet of sp^2-hybridized carbon atoms located in a hexagonal lattice [1]. Graphene synthesis is the production of graphene of the desired size, purity, and defect level using various methods [2-6]. The most commonly used methods of graphene synthesis are mechanical exfoliation; epitaxial growth; chemical vapor deposition (CVD); electrochemical exfoliation; chemical oxidation / reduction of graphite [7].

To obtain graphene by mechanical exfoliation, thin layers of highly oriented pyrolytic graphite are placed between the adhesive tapes, and the graphite films are separated again and again until a thin layer is obtained [1].

Another important method is the epitaxial growth of graphene, where graphene is grown on single-crystal silicon carbide (SiC). In this method, silicon carbide (SiC) is heated at a temperature of about 1200 °C under vacuum, resulting in the sublimation of Si atoms, forming carbon layers on SiC, which can be bilayer, multilayer or monolayer. In the CVD method, graphene is grown directly on various substrates of transition metals such as Ni, Cu, Co, Au and Ru by saturation of carbon under the influence of various gaseous hydrocarbons such as methane, ethylene, acetylene and benzene at high temperature.

In the CVD method, the difference between a cold wall and a hot wall is that the hot wall chamber is heated by an external energy source, while the temperature is everywhere relatively constant, and the substrate is heated by radiation from the heated walls of the chamber. In the reactor of the cold wall system, the sample is heated by the following different methods: passing current through the sample; using the heater that contacts the substrate; induction and the walls of the chamber are at room temperature [8].

The next method for obtaining graphene is electrochemical exfoliation of graphite. In this method, such electrodes as highly oriented pyrolytic graphite, graphite, Cu, Pt are used. In electrochemical separation, one of the important processes is the choice of the electrolyte, because

from it depends the increase of the charge transfer and the functionalization of the obtained graphene sheets. Many different electrolytes for electrochemical exfoliation, including HBr, HCl, HNO_3 and H_2SO_4, have been investigated, and the most commonly used of them are acid electrolytes containing H_2SO_4 and alkaline KOH electrolyte diluted with distilled water, which are ideal for exfoliation graphite [9-11]. To obtain graphene by this method, at first, two graphite electrodes or other types are inserted into the solution and about 10 V are applied to them, then the intercalating ion in the solution penetrates between the graphite layers exfoliates into few-layer graphene sheets, after which to separate the graphite particles from graphene solution is subjected to centrifugation or ultrasound is used to improve the cleavage, and then the solution is dried at the end [10, 12].

The last common method of producing graphene is referred to as the Hummer method [7]. In this method the starting material is graphite. The graphite is converted to graphene oxide by treatment with super acids, oxidizers and heat. The graphene oxide is then dispersed into water down to predominantly single sheets. These individual sheets of graphene oxide are then reduced with strong reducing agents to graphene. This process has two main problems. The first is that many defects remain in the hexagonal lattice after reduction, Secondly, the reduced graphene sheets have a strong tendency to restack into nano-graphite.

Considering the disadvantages of the above methods, we proposed a method for obtaining few-layer graphene structures and graphene on a nickel substrate, the essence of which was the diffusion of carbon through a nickel foil. This method is realized in conditions of high vacuum during resistive heating of nickel foil with tightly pressed pyrolytic graphite on one side.

Carbon diffusion in various materials was published in [13-16]. The diffusion and dissolution of carbon in nickel are considered in [17-19].

2 Experiment

In this paper, we investigated the diffusion of carbon through a nickel foil. As the initial material, we used highly oriented pyrolytic graphite (HOPG) from NT-MDT, nickel foil with a purity of 99.99%.

To confirm the diffusion nature of the process and to determine the concentration diffusion coefficient, we considered the theoretical Arrhenius relation.

$$D=D_{0exp}(-E_a/kT) \quad (1)$$

D – is the diffusion coefficient [m²/s]; E_a - activation energy [J]; k – is the Boltzmann constant [J/K]; T – is the temperature [K]. The average distance that a particle travels during a time τ is estimated by the relation

$$L=\sqrt{D * \tau} \quad (2)$$

For example, at a temperature of about 900 ^{0}C, the value of the concentration diffusion coefficient is estimated at 8.23 * 10^{-12} m^2/c. Table 1 shows the values of the process parameters.

Table 1 –The time dependence of the process (τ) on the substrate thickness (L) and temperature (T)

L (μm)	T (°C)	t (c)
40,2±4,2	903,7±5,5	182,31±22,40
60,5±3,4	900,5±6,4	431,64±7,05
80,3±3,8	902,7±4,0	736,32±25,69

We have proposed a method of growing graphene, few-layer graphene by the diffusion method on nickel foil in a high-vacuum chamber. The essence of this method is that in the case of resistive heating, the tightly pressed pyrolytic graphite on the nickel foil diffuses through the nickel foil and graphene and few-layer graphene layers are formed on the reverse side of the surface. Figure 1 shows the scheme of obtaining graphene on nickel by the diffusion method.

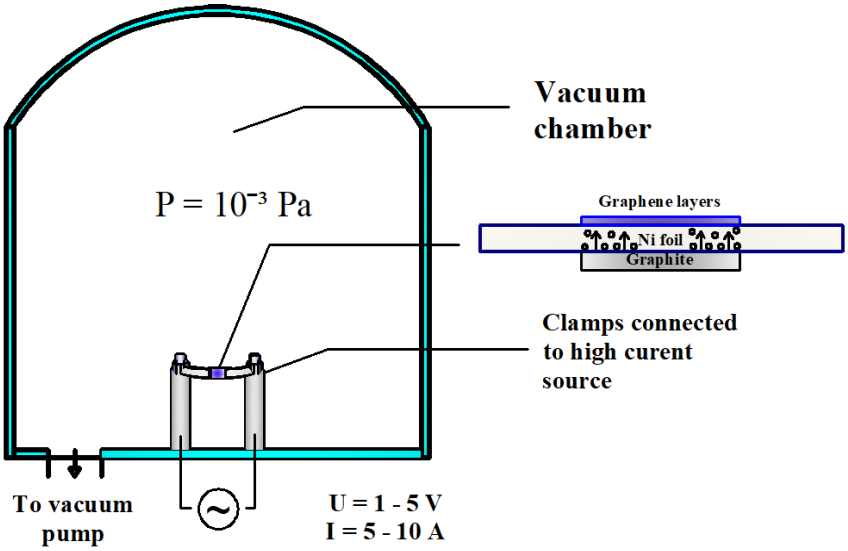

Figure 1 – Experimental setup of graphene production method

Before obtaining graphene or few-layer graphene by diffusion method on nickel, an experiment was first done to obtain the graphite layer. To perform this experiment, we took a thin nickel foil with a thickness of about 40 μm, with a size of 3.5 * 0.5 cm and highly oriented pyrolytic graphite (HOPG). HOPG was tightly pressed with nickel foil and under high vacuum conditions it was heated at a high temperature of about 900 °C until a graphite layers was formed on the other side of the nickel foil. Figure 2 shows a SEM image of graphite layers.

This figure clearly shows the folds, wrinkles on the surface of the graphite layers grown by the diffusion method on nickel foil.

After diffusion growth of the graphite layers, the surface of the nickel foil becomes defective and folds. According to the known literature data, during the process of growing graphene nanostructures, the interaction between the substrate and graphene strongly influences the formation of wrinkles, folds and pulsations due to the opposite polarity of the coefficients of thermal expansion of graphene nanostructures and metals [20]. Wrinkles, folds are more likely to occur due to the influence of thermal stress and compression when cooling graphene, graphene nanostructures.

The next process of our experimental part is the production of graphene, a few-layer graphene by the diffusion method on nickel foil. To obtain graphene or few layer graphene, we used the same initial materials that were used to obtain a graphite layer by the diffusion process. In this experiment, the thickness of the nickel foil ranged from 40 to 80 μm, the temperature of the resistive heating was 900 °C, and the time of obtaining a certain graphene layer depended on the size of the nickel foil and on the temperature (Table 1). Figure 3 shows the nickel foil before and after diffusion.

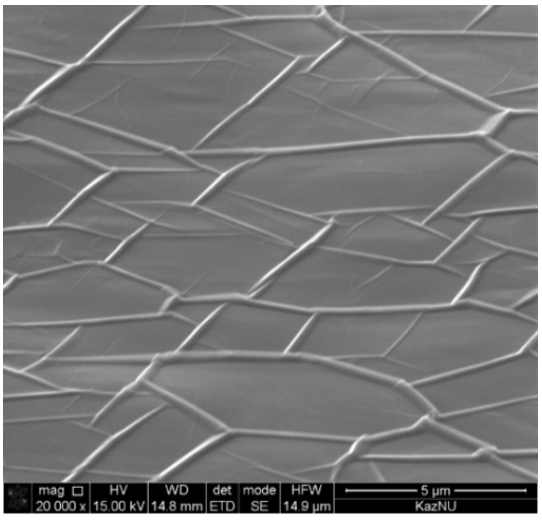

Figure 2 – SEM image of graphite layers

Figure 4 shows the optical image of the graphene obtained by the diffusion method on nickel at a temperature of 900 °C.

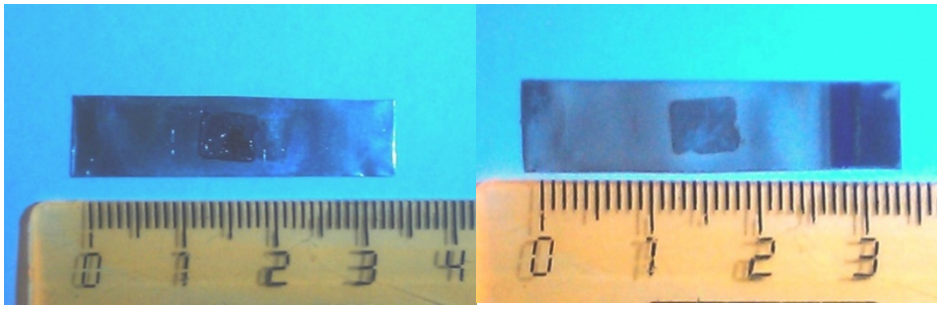

Figure 3 – Nickel foil before and after diffusion

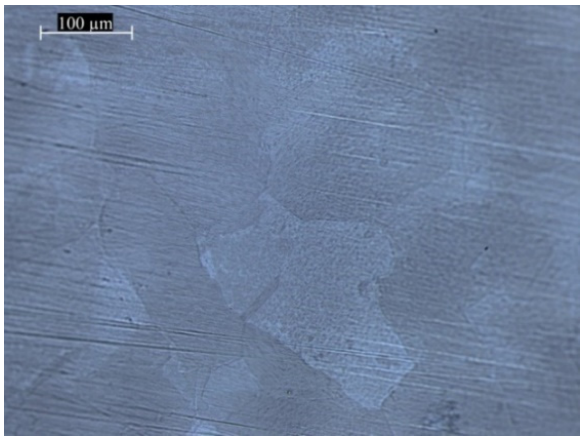

Figure 4 – Optical image of graphene

Optical image clearly shows graphene and few-layer graphene sheets grown by the diffusion method on nickel foil. This figure shows the grains of the nickel substrate and the boundaries on which the few-layer graphene sheets were grown, as well as the possibility of growing the larger size of graphene sheets, regardless of the morphology of the substrate surface and small nucleation centers. According to [21], the number of nucleation sites for graphene growth is extremely small on the Ni (111) surface, which is an important growth factor for large single-domain graphene crystals. According to the literature data, carbon diffusion in Ni (111) can occur mainly through grains and their boundaries or in other defective places in the graphene layer [22-25].

The average grain size of nickel and few-layer graphene was estimated in the analysis using optical microscopy. It was 10*15 μm^2 and Raman spectroscopy analysis confirmed the presence of few-layer graphene (FLG) on the obtained sample.

Figure 5 shows the Raman spectrum of graphene obtained by the diffusion method on nickel. The main modes of Raman spectroscopy of graphene, few-layer graphene are D, G, 2D peaks. D line (disorder, defects) this peak corresponds to defects inside the carbon lattice. D mode is due to the disordered structure of the graphene and is located in the region of 1370 cm^{-1}. G – the peak is located in the region of 1580 cm^{-1} and arises due to the E_{2g} mode at the G point, also the G-peak arises due to the expansion of the C-C bond of the graphite materials and is characteristic for all sp^2 carbon systems. In the Raman spectrum the 2D peak is located in the 2730 cm^{-1} range and the number of graphene layers can be determined with this peak [26, 27].

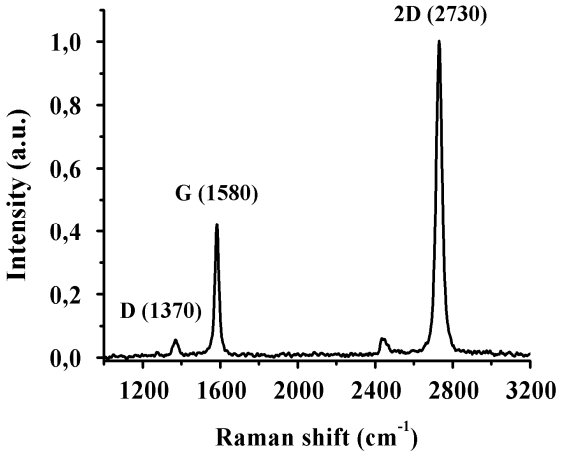

Figure 5 – Raman spectrum of graphene obtained by the diffusion method at the temperature of 900 °C.

According to [28], the number of layers of graphene is determined by the ratio of the intensities of the I_{2D}/I_G peaks. The ratio I_{2D}/I_G ~ 2-3 is characteristic for monolayer graphene, for two-layer graphene $2> I_{2D}/I_G> 1$ and for multilayer $I_{2D}/I_G<1$ [28, 29]. Based on the ratio of the intensity of the Raman scattering I_{2D}/I_G peaks, it can be concluded

that the graphene obtained by the diffusion method on nickel foil is a two-layer one (Figure 5).

3 Conclusions

We studied the production of graphene on nickel by diffusion method. The following problems were solved: the features of graphene production on nickel by diffusion method were studied; the most optimal process parameters for this method were determined; the obtained samples were investigated using optical microscopy, electron microscopy and Raman spectroscopy.

The obtained results of this method show the possibility of controlling the process of graphene formation by changing parameters such as temperature, time and thickness of nickel. During the experiment, the main parameters of carbon diffusion in nickel were estimated. In this case, the theoretical limiting possible size of the formed graphene is limited only by the size of the reaction chamber. The experimental results are well correlated with the theoretical Arrhenius ratio, which confirms the diffusion nature of the process.

Acknowledgments

The authors are grateful to Professor Ilyin A.M. and researcher Guseinov N.R. for assisting in the performance of this work.

References

1 K.S. Novoselov, A.K. Geim, S.V. Morozov, D.Jiang, Y.Zhang, S.V. Dubonos, I.V. Grigorieva, A.A. Firsov. Electric field effect in atomically thin carbon films // Science. – 2004. – Vol. 306. – P. 666-669.

2 A.M. Ilyin. Computer simulation of radiation defects in graphene and relative structures. In Graphene Simulation. Gong, J.R.; (Ed). InTech, Rijeka – 2011. – P. 39-52.

3 A.M. Ilyin, E.A. Daineko, G.W. Beall. Computer simulation and study of radiation defects in graphene // Physica E. – 2009. – Vol. 42. – P. 67-69.

4 A.M. Ilyin., G.W. Beall, I.A. Tsyganov. Simulation and study of bridge-like radiation defects in the carbon nanostructures // J. Comp. Theor. Nanosci. – 2010. – Vol. 7. – P. 2004-2007.

5 A.M. Ilyin, N.R. Guseinov, R.R. Nemkaeva, S.B. Asanova, V.V. Kudryashov. Bridge-like radiation defects in few-layer graphene // Nucl.Instrum&Methods in Phys.Res., B. – 2013. – Vol. 315. – P. 192-196.

6 M.M. Myrzabekova, S. Sarkar, G.A. Baigarinova, N.R. Guseinov, A.M Ilyin. Obtaining and research of new composite materials polymer-graphene // Phys. Sci. Technol. – 2014. – Vol. 1. – P. 4-9.

7 L. Shahriary, A.A. Athawale. Graphene oxide synthesized by using modified hummers approach // International Journal of Renewable Energy and Environmental Engineering – 2014. – Vol. 2. – P. 58-63.

8 K. S. Kim, Y. Zhao, H. Jang, S. Y. Lee, J. M. Kim, K. S. Kim, J.-H. Ahn, Ph. Kim, J.-Y. Choi, B. H. Hong. Large-scale pattern growth of graphene films for stretchable transparent electrodes // Nature – 2009. – Vol. 457(7230). P. 706–710.

9 K. Parvez, R. Li, S.R. Puniredd, Y. Hernandez, F. Hinkel, S. Wang, X. Feng, K. Mullen. Electrochemically exfoliated graphene as solution-processable, highly conductive electrodes for organic electronics // ACS Nano – 2013. – Vol. 7. -P. 3598.

10 C.Y. Su, A.Y. Lu, Y. Xu, F.R. Chen, A.N. Khlobystov, L.J. Li. High-quality thin graphene films from fast electrochemical exfoliation // ACS Nano – 2011. – Vol. 5. - P. 2332.

11 N. Liu, F. Luo, H. Wu, Y. Liu, C. Zhang, J. Chen. One-step ionic-liquid-assisted electrochemical synthesis of ionic-liquid-functionalized graphene sheets directly from graphite // Adv. Funct. Mater. – 2008. – Vol. 18. -P.1518.

12 V.V. Singh et al. Greener electrochemical synthesis of high quality graphene nanosheets directly from pencil and its SPR sensing application // Adv. Funct. Mater. – 2012. – Vol. 22. - P. 2352–62

13 J. Cermak, L. Kral. Carbon diffusion in carbon-supersaturated ferrite and austenite // Journal of alloys and compounds. – 2014. – Vol. 586. - P. 129 – 135.

14 I. V. Belova, G. E. Murch. Carbon interstitial diffusion in γ-Fe // Diffusion Fundamentals – 2005. – Vol. 2. -P. 48.1-48.2.

15 P. Werner, H.J. Gossmann, D. C. Jacobson. Carbon diffusion in silicon // Appl. Phys. Lett. – 1998. – Vol. 73. - No. 17. - P. 2465-67.

16 D.E. Jiang, E. A. Carter. Carbon dissolution and diffusion in ferrite and austenite from first principles // Physical review. – 2003 – Vol. 67. - P. 214103.Ch.

17 J.J. Lander, H.E. Kern, A.L. Beach. Solubility and diffusion coefficient of carbon in nickel: reaction rates of nickel carbon alloys with barium oxide // Journal of Applied Physics. – 1952. – Vol. 23. -P. 1305.

18 B.S. Berry. Diffusion of carbon in nickel // Journal of Applied Physics. – 1973. – Vol. 44. -P. 3792.

19 A. Wiltner, Ch. Linsmeier, T. Jacob. Carbon reaction and diffusion on Ni(111), Ni(100), and Fe(110): Kinetic parameters from x-ray photoelectron spectroscopy and density functional theory analysis // J Chem Phys. – 2008. – Vol. 129(8). - P.084704.

20 A. Obraztsov, E. Obraztsova, A. Tyurnina, A. Zolotukhin. Chemical vapor deposition of thin graphite films of nanometer thickness // Carbon. – 2007 – Vol. 45. - P. 2017–2021.

21 W. Zhu, et al. Structure and electronic transport in graphene wrinkles // Nano Lett. – 2012. – Vol. 12 (7). - P.3431.

22 G. Odahara, Sh. Otani, Ch. Oshima, M. Suzuki, T. Yasue, T. Koshikawa. In-situ observation of graphene growth on Ni(111) // Surface Science. – 2011. – Vol. 605. - P. 1095-1098.

23 Z. Fogarassy, M. H. Rümmeli, et al. Dominantly epitaxial growth of graphene on Ni (111) substrate // Surface Science – 2014. – Vol. 314. - P. 490–499.

24 I. Gierz, T. Suzuki, R.T. Weitz, D.S. Lee, B. Krauss, C. Riedl, U. Starke, H. Höchst, J.H. Smet, C.R. Ast, K. Kern. Electronic decoupling of an epitaxial graphene monolayer by gold intercalation // Physical Review B. – 2010. – Vol. 6 (81). - P. 235408.

25 L. Huang, Y. Pan, L. Pan, M. Gao, W. Xu, Y. Que, H. Zhou, Y. Wang, S. Du, H.J. Gao. Intercalation of metal islands and films at the interface of epitaxially grown graphene and Ru (0001) surfaces // Appl.Phys.Let. – 2011. – Vol. 99. - P. 163107.

26 A. C. Ferrari, D. M. Basko, Raman spectroscopy as a versatile tool for studying the properties of grapheme // Nat. Nanotechnol. – 2013. – Vol. 8. - P. 235–246.

27 A. Eckmann, A. Felten, A. Mishchenko, L. Britnell, R. Krupke, K. S. Novoselov, C. Casiraghi. Probing the nature of defects in graphene by Raman spectroscopy // Nano Lett. – 2012. – Vol. 12. - P. 3925–3930.

28 A.C. Ferrari, J.C. Meyer, V. Scardaci, C. Casiraghi, M. Lazzeri, F. Mauri, S. Piscanec, D. Jiang, K.S. Novoselov, S. Roth, A.K. Geim. Raman spectrum of graphene and graphene layers // Phys. Rev. Lett. – 2006. – Vol. 97. - P. 187401.

29 V. T. Nguyen, H. D. Le, V. Ch. Nguyen, T. T. T. Ngo, D. Q. Le, X. N. Nguyen, N. M. Phan. Synthesis of multi-layer graphene films on copper tape by atmospheric pressure chemical vapor deposition method. // Adv. Nat. Sci. – 2013 – Vol. 4. - P. 035012.

IRSTI 29.15.39

Method for determining angles in X-ray emulsion chambers (XRECs) (ADRON experiment)

S.B.Shaulov[1,2*], K.V. Cherdyntceva[1], J.K. Janseitova[1], R.A.Nam[1],
V.V. Piskal[1], V.S. Puchkov[1],
S.E. Pyatovsky[1], A.L. Shepetov[1], V.A.Ryabov[1] and V.V. Zhukov[1]

[1]*P.N. Lebedev Physical Institute of the Russian Academy of Sciences, Moscow 119991, Russia*
[2] *Moscow Institute of Physics and Technology (State University),MIPT (SU), Moscow, Russia*
e-mail: ser101@inbox.ru

Paper presents an analysis of the measurement procedure of the zenith and azimuth angles υ and φ in the X-ray emulsion chambers (XREC) of ADRON and PAMIR experiments. Earlier, asymmetry was observed in distributions of azimuth angles of gamma and hadron families. A detailed analysis of methodological errors in measuring θ, φ angles allowed us to establish the causes of the distortion of azimuth angles distributions. There are two reasons: systematic errors in the measurement of zenith angles by MBS-2 microscopes, used both in the PAMIR experiment, and in the ADRON experiment, and the inclination of XREC based on the subsidence. Calculations showed that the total systematic error $\Delta\upsilon \approx 4$ ° completely explains the observed azimuthal asymmetry. Formulas for correcting θ and φ angles are given. The recalculation of the angles by the indicated formulas showed that this corrects the distribution of the azimuthal angles φ. The REC plane should be set relative to the horizontal with an accuracy of no worse than 1 degree in order to avoid distortion of the angular distributions.

Key words: XREC, ADRON, EAS, ionization chambers, cascades, BSM-2 microscope, Gaussian.
PACS number(s): 23.20.En, 26.90 + n, 29.87.+ g, 29.90.+ r.

1 Introduction

Characteristics of cosmic rays (CR) in the energy region above 19^{15} eV are studied in ground-based experiments deep in the atmosphere. The spectrum and composition of CR is restored by parameters of extensive atmospheric showers (EAS) generated by CR nuclei. Of greatest interest is the small area of EAS near its axis, the EAS cores, where the most energetic hadrons are concentrated. The most informative core detector is the x-ray emulsion chamber (XREC) [1-8] . To determine the primary energy is necessary to register the entire shower, for this purpose XREC is combined with EAS electronic detectors in the so-called hybrid installations [9-15].

The hybrid experiment ADRON [16-19] was started in 1985 to combine the techniques of the EAS and the XREC. The unification of events in the XREC with the EAS was made statistically, using information about the location and angles of the EAS and events in the XREC. Such a method particularly requires obtaining reliable information about angles in the XREC [20-24]. It is known from practice that processing of film information always contains operator errors. To reduce the number of measurement errors, the angles of events in the REC were measured twice and by different operators. With a significant discrepancy between the values of at least one of two angles, a control measurement was made. This procedure reduced the number of errors from 10% to 2% [20].

The installation of ADRON was operated at the Tien Shan station (690 g/cm^2) from 1985 to 1991. In the experiment, two types of XRECs with an area of 162 m^2 were exhibited. The designs of both types of XRECs are shown in Figure 1. In 1985-1986, two half-years and in 1986-89 three one-year exposures of the hadron chamber were made in 1989-1991, two single-year exposures of a thin lead chamber.

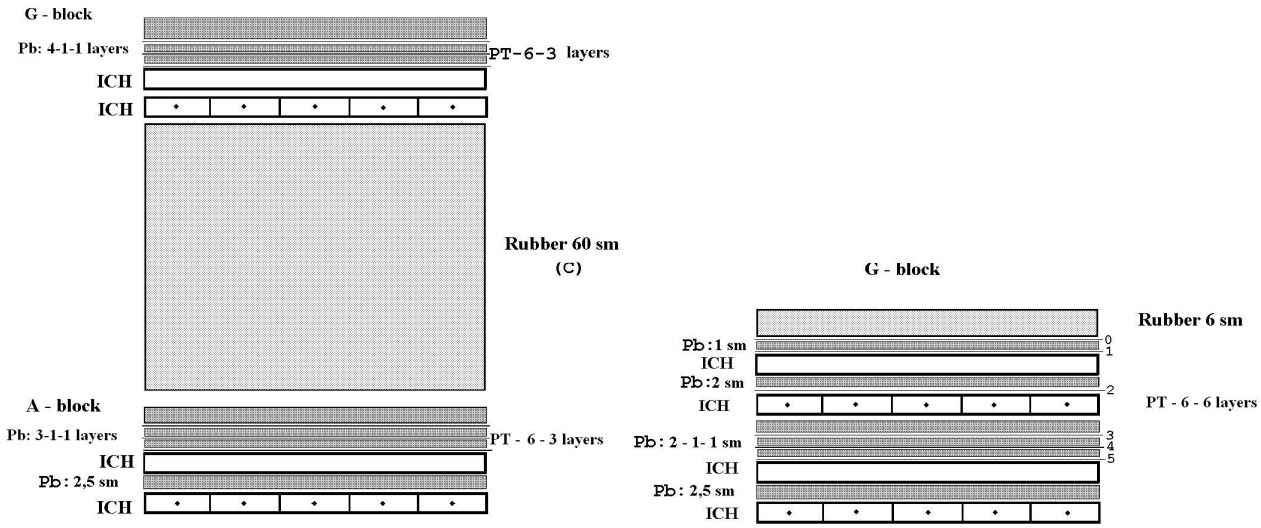

Figure 1 – X-ray emulsion chambers (XRECs) of the ADRON experiment

For comparison with EAS in the XREC, gamma-ray families with a total energy of $\sum E_\gamma \geq 10$ TeV were selected. Statistics of such events in the exposures of 1985-1989 (hadron chamber) was 2816 for the gamma-ray unit, and 2222 for the hadron block. In expositions of 1989-1991 (thin lead chamber) it was about 1004 of such events (gamma-family).

Figure 2 shows the spectra of the total energy of the families $\sum E_\gamma$ for the Γ-block and $\sum E_\gamma^h$ for the A-block of the hadron XREC [21]. In the Γ-block gamma-quanta families with energies above 2-4 TeV formed during the decay of π^0-mesons are detected. Charged $\pi^\pm$ -mesons interact in the carbon block of the XREC. In this case, the π^0 mesons and gamma quanta from their decay are also registered in the hadron block of the XREC. The energy of these families of gamma quanta is denoted as $\sum E_\gamma^h$, where E_γ^h is the part of the charged hadron energy released into gamma quanta.

Figure 3 shows the distributions of selected events by multiplicity. The left figure shows the spectra in the Γ-block of the hadron XREC (upper spectrum) and the spectrum for a thin lead chamber (bottom). The break in the spectrum of the lead chamber is due to the presence of gaps occupied by ionization chambers. The right figure shows the multiplicity spectrum for the A-block of the hadron XREC.

Figure 4 shows the distributions of azimuth angles measured in the G and A-blocks of the hadron chamber (2 and 5 series, respectively) [21]. The azimuthal distributions are noticeable, at the level of 6σ, different from the uniform ones, which contradicts the data on CR at energies of the 10^{15} eV order and higher. This means that distortions of distributions must be linked with methodological reasons. Most likely this can be due to an error in definition of the vertical. It is known that due to a sharp decrease in the intensity of cosmic rays with an angle θ, the deviation from the vertical should lead to a significant non-distribution of events between different azimuthal directions.

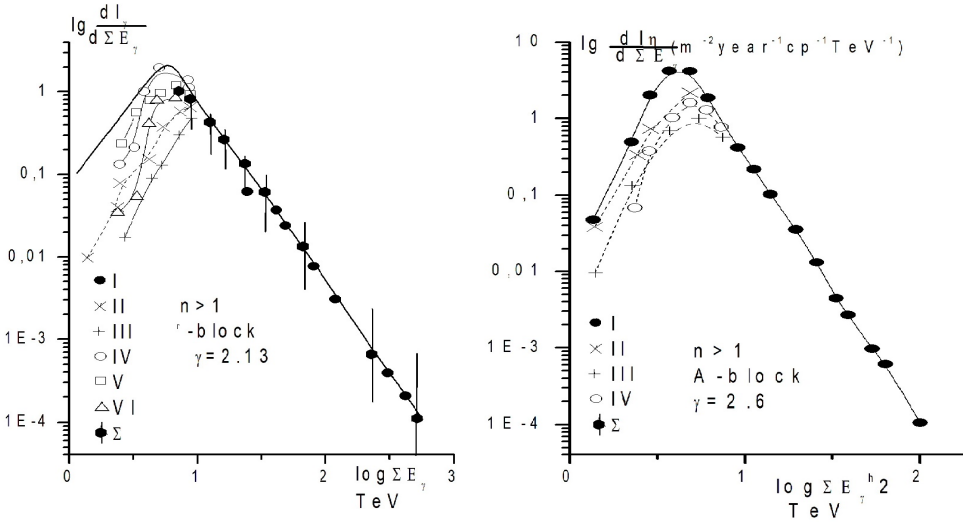

Figure 2 –The spectra of $\sum E_\gamma$ and $\sum E_\gamma^h$ for families selected in gamma and hadron blocks at $n_{\gamma,h} \geq 1$

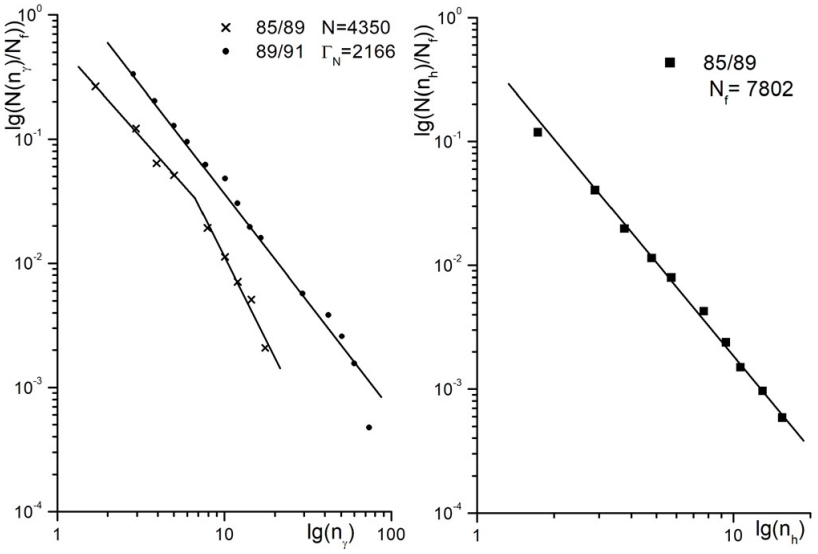

Figure 3 – Integral spectra of multiplicities in the G- and A-blocks of the XREC (without selection on the threshold)

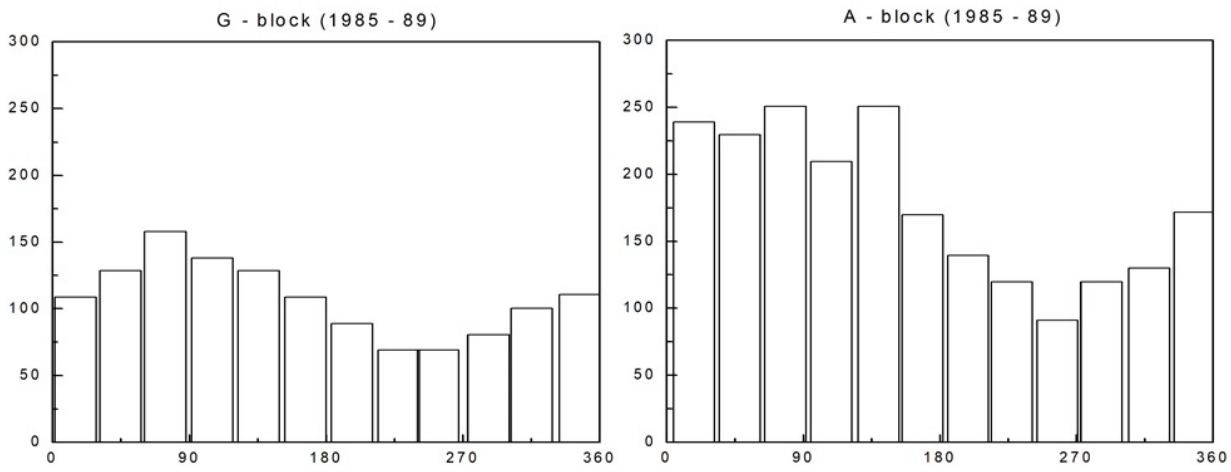

Figure 4 – Differential distributions of the azimuthal angles φ in the G- and A-blocks of the XREC.

2 Estimation of the distortion of azimuthal distributions.

The differential CR spectrum with respect to the number of particles N at a depth x in the atmosphere is written in the form [22]:

$$\frac{dI}{dN \cdot d\theta \cdot d\varphi} = A(\theta, x) N^{-(k+1)} \sin\theta, \quad (1)$$

where k is the index of the spectrum of showers with respect to the number of particles.

If we do not take into account the change in the atmosphere density along shower path,

$$A(\theta, x) = \exp\left(-\frac{k}{\Lambda}\left(\frac{x}{\cos\theta} - x \right)\right) \approx \cos^{\frac{k}{\Lambda}x}\theta, \quad (2)$$

where Λ is the range of absorption of showers with the number of particles. Then the differential angular spectrum can be written in the form:

$$d^2 I = \frac{m+1}{2\pi} I_0 \sin\theta \cos^m\theta \cdot d\theta \cdot d\varphi, \quad (3)$$

where I_0 is the total intensity of the events, and $m=\frac{k}{\Lambda}x$

If this expression is integrated with respect to υ, then we obtain:

$$dI(\rangle\theta) = \frac{I_0}{2m}\cos^{m+1}\theta \cdot d\varphi, \quad (4)$$

uniform distribution by φ.

Methodical deviation from the vertical is equivalent to rotating the coordinate system around any horizontal axis. Moreover, the redistribution of events between different intervals φ depends to a large extent on the value of the exponent m, which in our case is m = 8.2 and 9.1 for the hadron and gamma blocks, respectively.

We consider the transformation of the differential function d^2I, when the coordinate system rotates about the X axis by an angle α. Since the volume element $dV=r^2 dr d\Omega$ is an invariant of orthogonal transformations, and r does not change under rotations, then dΩ also remains unchanged. The transformation of $\cos^m\theta$ is more convenient to consider in Cartesian coordinates, and then return to spherical, but already in the rotated coordinate system. The rotation matrix at an angle α around the x axis has the form:

$$\begin{pmatrix} 1 & 0 & 0 \\ 0 & \cos\alpha & -\sin\alpha \\ 0 & \sin\alpha & \cos\alpha \end{pmatrix}$$

Proceeding the corresponding transformation of the Cartesian coordinates and taking into account that $\cos\theta = z/r$, we finally obtain:

$$d^2 I = \frac{m+1}{2\pi} I_0 \cos\theta \cos^m \alpha (1 - \sin\varphi \cdot tg\alpha \cdot tg\theta)^m \sin\theta d\theta d\varphi, \quad (5)$$

Taking into account the smallness of α and that $\theta < 45°$, we can confine to the first two terms of the polynomial in parentheses. Integrating this expression with respect to θ within θ, π/2, we obtain the differential distribution of azimuthal angles in the following form:

$$\frac{dI}{d\varphi}(\rangle\theta, \alpha) = \frac{\cos^{m+1}\theta}{2\pi} I_0 (1 - A\sin\varphi), \quad (6)$$

where

$$A = \frac{m(m+1)}{\cos^{m+1}\theta} tg\alpha \int_{\vartheta}^{\pi/2} \ln^2 \theta \cos^{m-1}\theta d\theta, \quad (7)$$

Taking into account that m is not an integer, the integral in the expression for the coefficient A must be found by numerical methods. The values of the integrals (6) over φ in the range from 0 to π, and from π to 2π give the expression for the asymmetry coefficient K:

$$K = \frac{\pi + 2A}{\pi - 2A}, \quad (8)$$

Table 1 shows the results of calculating the values of A and K at the experimental values of m = 8.2 and m = 9.1 for the hadron and gamma XREC blocks, respectively. The last column shows the experimental values of K.

Table 1 — The asymmetry coefficients K

m	α	θ	A	k	K_{ex}
8.2	3°	0°	0.19	1.28	1.36±0.04
		20°	0.27	1.41	1.64±0.07
		30°	0.35	1.57	1.78±0.11
	4°	0°	0.26	1.39	1.36±0.04
		20°	0.36	1.59	1.64±0.07
		30°	0.46	1.84	1.78±0.11
9.1	3°	0°	0.20	1.30	1.26±0.04
		20°	0.29	1.45	1.44±0.04
		30°	0.38	1.63	1.52±0.12
	4°	0°	0.27	1.42	1.26±0.04
		20°	0.38	1.65	1.44±0.04
		30°	0.50	1.94	1.52±0.12

Comparison of the experimental and calculated data shows that the deviation from the vertical by an angle α = 3-4° explains the observed asymmetry.

3 The procedure for measuring angles in XREC.

The RT-6M X-ray film used in the XREC has two emulsion layers applied on both sides to a substrate with a thickness of 200 μm. The zenith angle θ of the cascade passage through the film is measured by the relative shift of the darkening spots in the upper and lower layers. As the center of the spot, a region with a maximum of darkening is taken. The measurement is carried out using the BSM-2 microscope, which has a linear scale for determining the distance between the spots of darkening of Δ, and finding tgθ= Δ/d , where d is the thickness of the substrate. In addition, the microscope has an angular scale along which the azimuth angle of the cascade φ is determined. The azimuth angle is formed by the coordinate axis x and the straight line in the plane of the film passing through both darkening spots in the direction "towards the source". The angle φ is measured from the x-axis in a counter-clockwise direction. The scheme for measuring the angles is shown in the Figure 5. In each microscope, a linear scale for determining Δ(θ) is calibrated using an object-micrometer. In our case, we used two microscopes

with a fission rate of 11.4 and 13.7 μm in the object plane with 7x zoom. The measurement errors for θ and φ are obtained from the geometric relationships in the following form:

$$\Delta\theta = K\cos^2\theta, \Delta\varphi = Kctg\theta, \quad (9)$$

where K=0.058.

In the region of small angles θ the azimuth angle is not determined due to the overlap of the spots.

The magnitude of this region depends on the diameter of the spots D, i.e. from the energy of the cascades. The spot diameter is related to the energy by the empirical relationship $D=35\sqrt{(E_\gamma)}$ μm, where E_γ in TeV.

The accuracy of determining the center of the spot $\Delta l \sim 0.2D$.. Then, assuming that the overlap area of the spots is $\Delta l \sim 0.5D$, we obtain the estimate θ_{nep} 10° for E_γ =4 TeV.

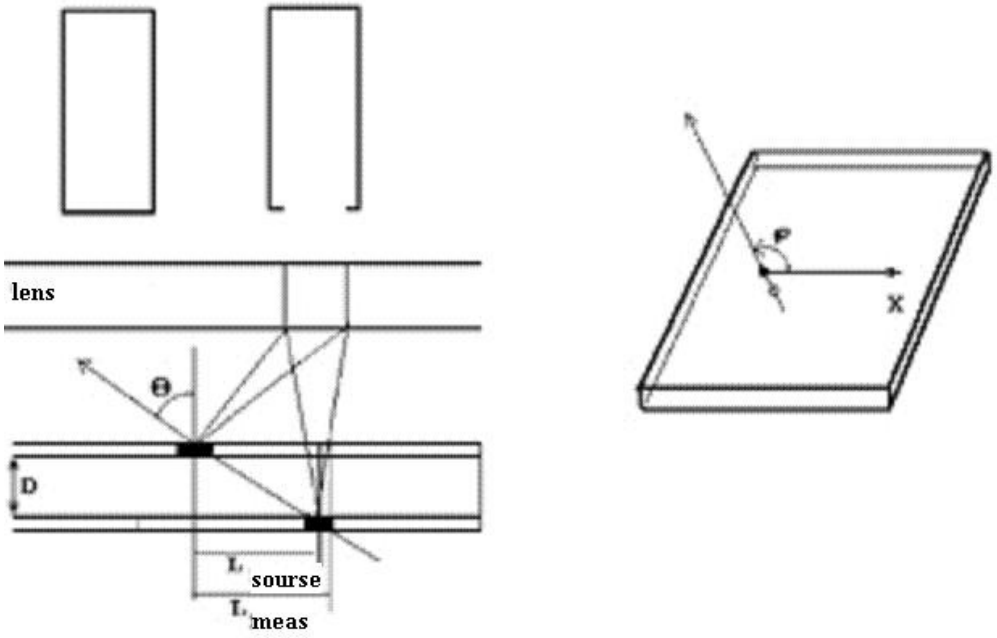

Figure 5 – Scheme of measurement of angles

4 Correction of azimuthal asymmetry

To test the azimuthal sensitivity of the X-ray film, it was irradiated with a radioactive source of gamma quanta BIS-1M. To eliminate the azimuthal inhomogeneity of the irradiation, the film was placed on the disc of the turntable and rotated at a speed of 45 rpm. Dimensions of the darkening were made inside the rings for different angles φ. As follows from the analysis of the data, the sensitivity of the X-ray film from the azimuth angle does not depend.

It turned out that the asymmetry arises from the presence of a systematic error in determining the angle υ and its azimuthal dependence. The scale for determining the distance Δ between the darkening spots on the upper and lower layers of the emulsion was always located in the right eyepiece of the BSM-2 stereo microscope. The optical scheme of it is arranged in such a way that each of the eyepieces "looks" at the object table at an angle ~2°. This is clearly seen in Figure 6, on which the laser beam passes through the optical system, reflecting from the mirror on the stage. As a result, the angle υ decreases for cascades coming to the right of the microscope and increases for those coming from the left. Since the orientation of X-ray films during exposure and measurement always remains this simulated azimuthal asymmetry relative to the sides of the Light.

The magnitude of the distortion of the zenith angle was determined by the difference method. For each cascade, the angle υ was measured at two positions of the film corresponding to the angle

φ=0°and 180°. The difference between these values is 2α .As a result of the measurements, α =2.2°±0.5° was obtained for α. This is somewhat less than the required value, which follows from the calculations. Further testing showed that the missing 2° are added because of uneven subsidence under the XREC and the slope of the concrete foundation. In the Figure 7 corrected distributions of azimuth angles are given taking into account the systematic errors of the microscope and the inclination of the XREC base.

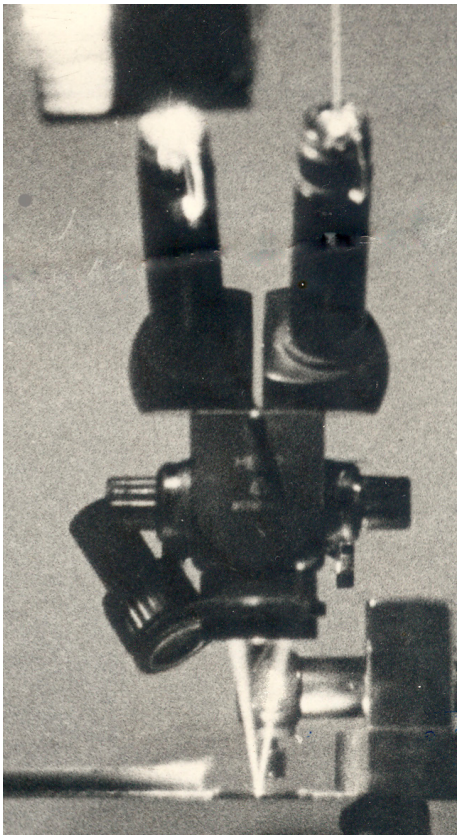

Figure 6 – Optical scheme for obtaining a stereo image in the BSM-2 microscope.
The image is obtained by passing a beam of light from the laser through the microscope optics

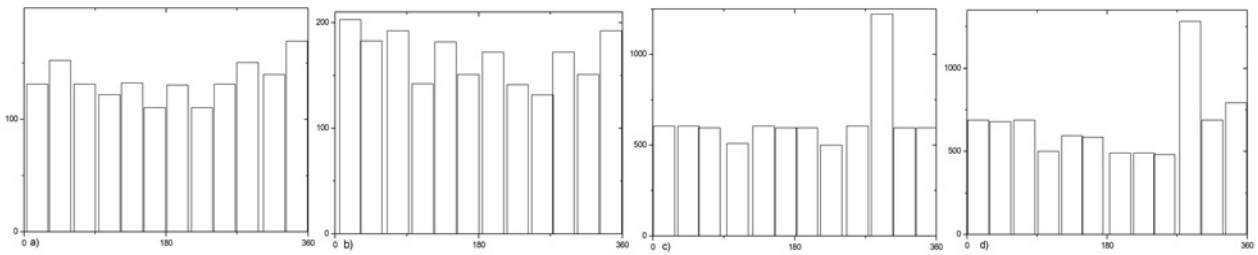

Figure 7 – Differential distributions of the azimuthal angles φ in the G- and A-blocks of the XREC. Figures c) and d) are the same - θ >30°, but for θ >3°

For each event in the XREC, the corrected angles were determined by the formulas (10):

$$tg\theta_{испр} = (tg^2\theta^{изм} + tg^2\alpha + 2tg\theta^{изм} \cdot tg\alpha \cdot \cos\varphi^{изм})^{\frac{1}{2}},$$
$$\cos\varphi_{испр} = tg^{-1}\theta_{испр}(\cos\varphi^{изм} \cdot tg\theta^{изм} + tg\alpha), \quad (10)$$

where α – is the total systematic error in the zenith angle θ.

5 Determination of random errors in measuring the angles θ and φ.

To obtain measurement errors 600 cascades were selected in the XREC HADRON and the values of their angles υ and φ were measured on four different microscope BSM-2. The Figure 8 shows the distributions of measurement errors $\Delta\theta$, $\Delta\varphi$, obtained by subtracting individual measurements from the average of four dimensions.

The distributions are practically Gaussian. The gross measurement errors making up θ 4% and φ 9%, were detected and eliminated during the two-dimensional measurement of angles. For measurement errors, the values $\Delta\theta$,= -0.1.6±2.6 are obtained for zenith and $\Delta\varphi$ =-0.1±8.6 for the azimuth angles.

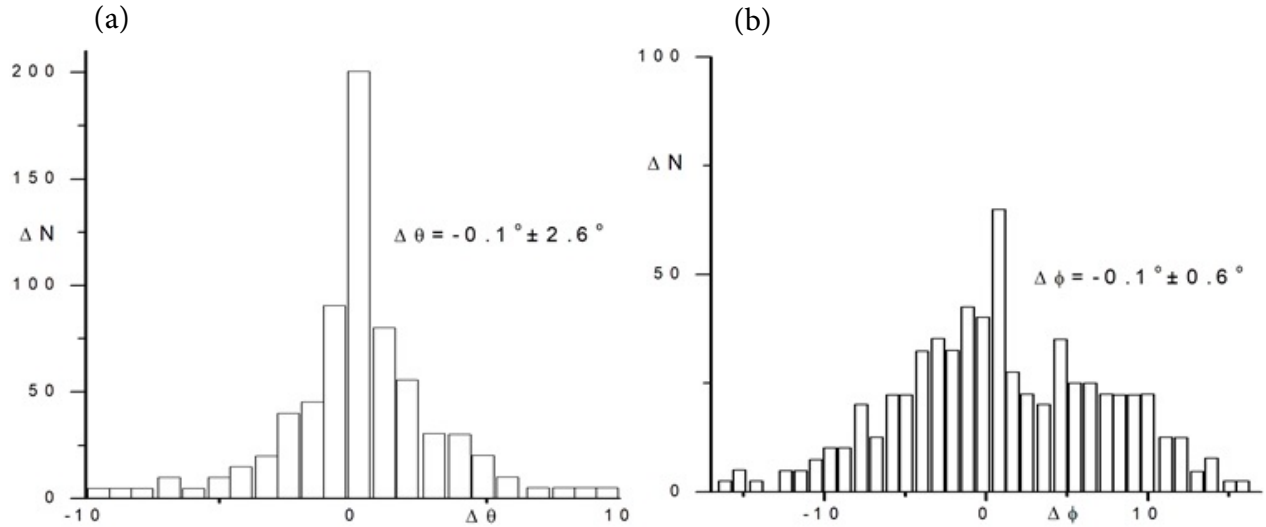

Figure 8 – Distributions of measurement errors for zenith (a) and azimuth (b) angles

6 Conclusion

Summarizing the results we can conclude:

1. The method of measuring the angles θ and φ in the XREC with the help of stereomicroscopes BSM-2 introduces a number of distortions:
2. In the range of angles θ = 0-10°, the method does not work due to overlapping of the darkening heels.
3. The stereo effect in BSM-2 microscopes leads toa systematic distortion of the angles $\Delta\theta \approx 2°$.
4. In order to obtain undistorted angular distributions, the XREC plane should be exposed with respect to the horizontal with an accuracy not worse than 1°.

References

1 S.G. Baiburina, S.B. Shaulov et al. Investigation of characteristics of hadron and gamma ray families with multilayer emulsion chambers //Alma-Ata-Dushanbe-Cracow-Lodz-Moscow-Tashkent-Tbilisi collaboration, In Kyoto 1979, Proceedings, 16th International Cosmic Ray Conference, Vol. 7. –P. 240-245.

2 Pamir Collaboration. The types of emulsion chambers in the experiment"Pamir". Naukowe Uniwersytetu Lozkiego, Zeszyty 60. – 1977. Ser.11. –P. 7-22, Lodz.

3 S.G. Baiburina, S.B.Shaulov et al. Energy spectrum and path for interaction for hadron with energy of 10Tev-100Tev, by Alma-Ata-Dushanbe-Cracow-Lodz-Moscow-Tashkent-Tbilisi collaboration, In Kyoto 1979, Proceedings of 16th International Cosmic Ray Conference, Vol. 7. – P. 74-79.

4 G. B. Zhdanov, S.A. Slavatinsky, Yu.A. Smorodin, N.G. Zelevinskaya, V.S. Puchkov, V.G. Denisova, K. V. Cherdyntseva, A.M. Dunaevsky, A.V. Uryson, S.G. Baiburina, Z.M. Guseva, S.B. Shaulov, M.D. Smirnova. Investigation of the hadron component of cosmic rays at the mountain level using multilayer X-ray emulsion chambers (Experiment "Pamir") // USSR AS Bulletin. Phys. Ser., - 1980. –Vol. 44. –No.3. - P. 457-460. (in Russian).

5 G. B. Zhdanov, S.A. Slavatinsky, Yu.A.Smorodin, V.M. Maksimenko, N.G. Zelevinskaya, V.S. Puchkov, S.A. Dubrovina, V.G. Denisova, E.A. Kanevskaya, K.V. Cherdyntseva, A.M. Dunaevsky, A.V. Uryson, S.G. Baiburina, Z.M. Guseva, S.B. Shaulov, M.D. Smirnova, S.A. Pashkov. Spatial characteristics of the gamma-quanta families (Pamir experiment) // USSR AS Bulletin. Phys. Ser. - 1980. -Vol.44, -No.3. - P. 454-456. (in Russian).

6 Pamir collaboration. Hadron families and intensity of primary protons at energy 10^{15}ev. Lodzinsky University, Poland, Working meeting 1980.

7 Pamir Collaboration. The azimuthal structure of gamma families in the Pamir experiment // Proc. 17-th Inter. Conf. on Cosmic Rays, Paris, France. -1981. –Vol.11. – P.156-158.

8 Pamir Collaboration. Investigation of nuclear interactions in the field of energies 10^{14}-10^{17}eV by the method of X-ray emulsion chambers in cosmic rays // Cooperation "Pamir", FIAN Proceedings. Moscow. -1984. -No.154. - P. 3-141 (in Russian).

9 V. Danilova, S. B. Shaulov, et al., Project of an experiment to study hadron interactions in the 10^3-10^5 TeV energy range (ANI experiment)// Armenian SSR AS Bulletin. Phys. Ser.. -Vol.17, -No. 3-4. -P. 129-232. (in Russian).

10 M.O. Azaryan, S. B. Shaulov. "STEP" installation project for joint registration of EAS and gamma families // Preprint FIAN. -1982. –Vol. 44. –P. 1-31. (in Russian).

11 T.V. Danilova, A.D. Dunaevsky, S.B. Shaulov et.all. The project of the experiment on investigation of hadron sand nuclei in the energy range 10^3− 10^5TeV // Proceedings of 18-th Inter. Conf. on Cosmic Rays, Bangalore. -1983. – Vol. 5. –P. 520-523.

12 T.V. Danilova, A.D. Dunaevsky, S.B. Shaulov. The ANI installation for the study of the interaction of hadrons and nuclei in the energy range 10^3− 10^5TeV // Proceedings of 18-th Inter. Conf. on Cosmic Rays, Bangalore. -1983. – Vol. 5. – P. 527-530.

13 G.B. Zhdanov, S.A. Slavatinsky, V.M. Maksimenko, T.V. Danilova, Yu.N. Vavilov, V.I. Yakovlev, N.M. Nesterova, V.S. Puchkov, V.G. Denisova, E.A. Kanevskaya, V.P. Pavlyuchenko, K.V. Cherdyntseva, Z.M. Guseva, S.B. Shaulov, A.P. Chubenko, R.U. Beysembaev, L.I. Vildanova, A.S. Borisov, S.A. Karpova, V.P. Antonova, A.L. Shchepetov, V.M. Aushev, P.A. Beyl, E.N. Gudkova. The project of modernization of the Pamir and Adron facilities for a comprehensive study of EAS // Preprint FIAN. – 1996. -No. 59. –P. 1-26. (in Russian).

14 S.B. Shaulov, R.M. Martirosov, E.A. Mamidjanian, L.W. Jones, O. Saavedra, M.Tamada. Partial reanimation of experimental complex ANI at Mt. Aragats (proposal) // Proceedings of the ICRW "Aragats 2007", Nor-Amberd, Armenia, 8-13 September. -2007. -P. 153-156.

15 S.B. Shaulov. Hypothesis of strange quark matter in cosmic rays // Preprint of FIAN. -2012. – No.19. -P. 3-42. (in Russian).

16 S.B.Shaulov. Statistical criteria for the combination events in EXC and EAS (Exp."Hadron") // Preprint FIAN. -1987. -No.245. – P.3-12.

17 V.V. Arabkin, D.S. Adamov, S.B. Shaulov et al. On the question of the applicability of the NCG functions for describing the spatial distribution of EAS electrons at the mountain level // Materials All-Union Conf. by space rays, Alma-Ata. Part 2. -1989. -P. 40-41. (in Russian)

18 D.S. Adamov, V.V. Arabkin, S.B. Shaulov et al. Phenomenological characteristics of EAS with $N_e = 210^5$ – 210^7 obtained by the modern Tien-Shan installation "Hadron" // Proceedings of 20-th Inter. Conf. on Cosmic Rays, Moscow. -1987. –Vol.5. - P. 460-463.

19 D.S. Adamov, V.V. Arabkin, L.I. Vildanova, S.B. Shaulov et.al. Installation of Hadron-2 for studying the characteristics of the electron-photon component of EAS trunks in the energy range 0.1-100 PeV // USSR AS Bulletin. Phys. Ser. -1991. -Vol.56. –No.4. -P. 703-708. (in Russian).

20 Z. Zhanseitova, L.V. Sukhov, S.B. Shaulov, et al., Analysis of the angular distributions of events recorded in the X-ray emulsion chamber of the Hadron experiment // Preprint FIAN. -1991. –No.147. -P. 2-14. (in Russian).

21 K.V. Cherdyntseva, J.K .Janseitova, S.B. Shaulov et al. Azimuth asymmetry of the γ-ray, Hadron and their families flow and the analysis of the zenith angles distributions for X-ray emulsion chambers (Experiment"Hadron")// Proceedings of 23-th Inter.Conf. on Cosmic Rays, Calgary. -1993. –Vol.4. –P. 88-91.

22 J.K. Zhanseitova, K.V. Cherdyntseva, S.B. Shaulov. Analysis of methodological distortions in measuring angles in the REC // Preprint FIAN. – 1994. –No.25. -P. 2-36. (in Russian).

23 S.B. Shaulov, Methods for determining the characteristics of EAS in combined events and violation of scaling // Preprint FIAN. -1996. -No. 60. -P. 1-37. (in Russian).

24 Zh.K. Zhanseitova, K.V. Cherdyntseva, S.B. Shaulov. Investigation of the angular spectra of gamma and hadron families in the experiment "Hadron" cosmic rays (project ADRON-M). Preprint FIAN. -1999. –No.32. –P. 1-32. (in Russian).

IRSTI 58.33.37

Calculation of tritium release from driver fuels into primary coolant of research reactors

Hai Quan Ho and E.Ishitsuka*

Sector of Fast Reactor and Advanced Reactor Research and Development,
Japan Atomic Energy Agency (JAEA), 4002 Narita-cho, Oarai-machi,
Higashi Ibaraki-gun, Ibaraki-ken, 311-1393, Japan
**e-mail: ishitsuka.etsuo@jaea.go.jp*

Increasing of tritium concentration in the primary coolant of the research and test reactors during operation had been reported. To check the source for tritium release into the primary coolant during operation of the JMTR and the JRR-3M, the tritium release from the driver fuels was calculated by MCNP6 and PHITS. It is clear that the calculated values of tritium release from fuels are as about 10^7 and 10^6 Bq for the JMTR and JRR-3M, respectively, and that calculated values are about 4 order of magnitude smaller than that of the measured values. The JMTR is a tank type, and the JRR-3M is a pool type research reactor. The primary coolants are light water, in which the coolant temperature is lower than 50ºC. These results show that the tritium release from fuels is negligible for both the reactors. In the calculations of tritium release rates into the water by PHITS, a gaussian triton energy by ternary fissions of ^{235}U.

Key words: tritium release rate, driver fuels, primary coolant, JMTR, JRR-3M.
PACS numbers: 25.85.Ec, 28.41.Er.

1 Introduction

Tritium release into the primary coolant during operation of the JMTR (Japan Materials Testing Reactor) and the JRR-3M (Japan Research Reactor-3M) had been measured. As results, the amount of tritium release per operation cycle was reported as $1\sim2\times10^{11}$ Bq and $1\sim4\times10^{10}$ for the JMTR and JRR-3M, respectively [1-5]. The sources and mechanism of the tritium release had been studied [6-10], and it is clear that the beryllium components in core strongly affect the tritium release into the primary coolant. However, to get a scientific evidence, the other effects such as a ternary fission by the driver fuels should be checked [11-15]. Therefore, the calculation of tritium release from the driver fuels was carried out in this paper.

2 Calculations of tritium release from driver fuels

Outline of the JMTR and the JRR-3M are summarized in Table 1. The JMTR is a tank type, and the JRR-3M is a pool type research reactor. The primary coolants are light water, in which the coolant temperature is lower than 50ºC. Core configurations for both the reactors are shown in Figures 1 and 2 [1]. In this calculation, it was assumed that all fuels were the same as standard fuel. Size of standard fuel plates for both the reactors are shown in Table 2 [16, 17].

Table 1 – Outline of JMTR, JRR-3M

Items	JMTR	JRR-3M
Thermal power (MW)	50	20
Main purposes	Irradiation tests, RI productions, Training	Beam experiments, RI productions
Main core components	Be, Al	Be, D_2O tank
Operation	30d/cy, 6cy/y	25d/cy, 6cy/y

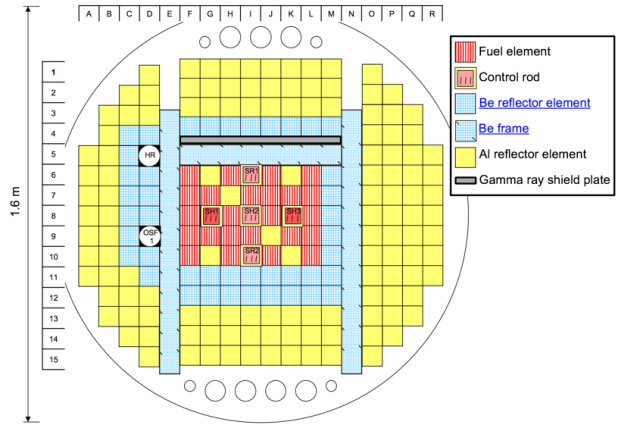

Figure 1 – Core of JMTR

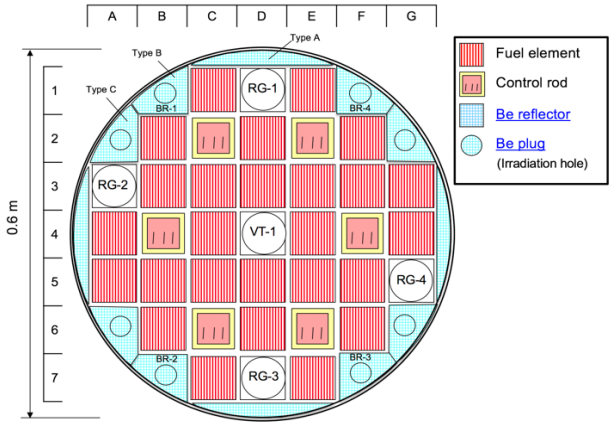

Figure 2 – Core of JRR-3M

Table 2 – Size of standard fuel plate

Items	JMTR	JRR-3M
Fuel meat thickness (mm)	0.51	0.51
Fuel meat width (mm)	62	62
Fuel meat length (mm)	760	750
Thickness of cladding (mm)	0.38	0.38
Fuel plate thickness (mm)	1.27	1.27
Fuel plate width (mm)	71	71
Fuel plate length (mm)	780	770

The difference in size of standard fuel plates between both the reactors is only the length. The cross-section of both fuel plates are the same size. Calculation model of the standard fuel plate is shown in Figure 3. Tritium productions by the ternary fissions and tritium release rates into the water for one operating cycle in both the reactors were calculated by MCNP6 [18] and PHITS [19], respectively. The calculation results of tritium production by MCNP are shown in Table 3.

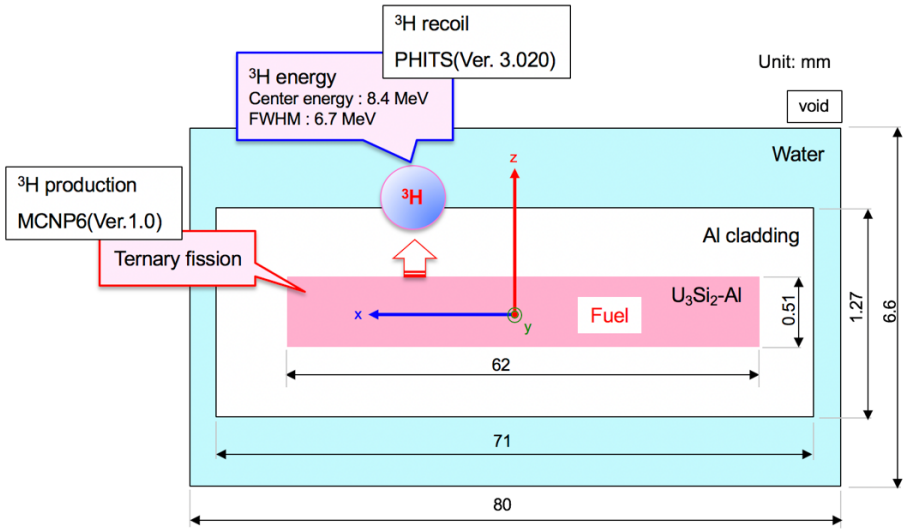

Figure 3 – Calculation model of standard fuel plate

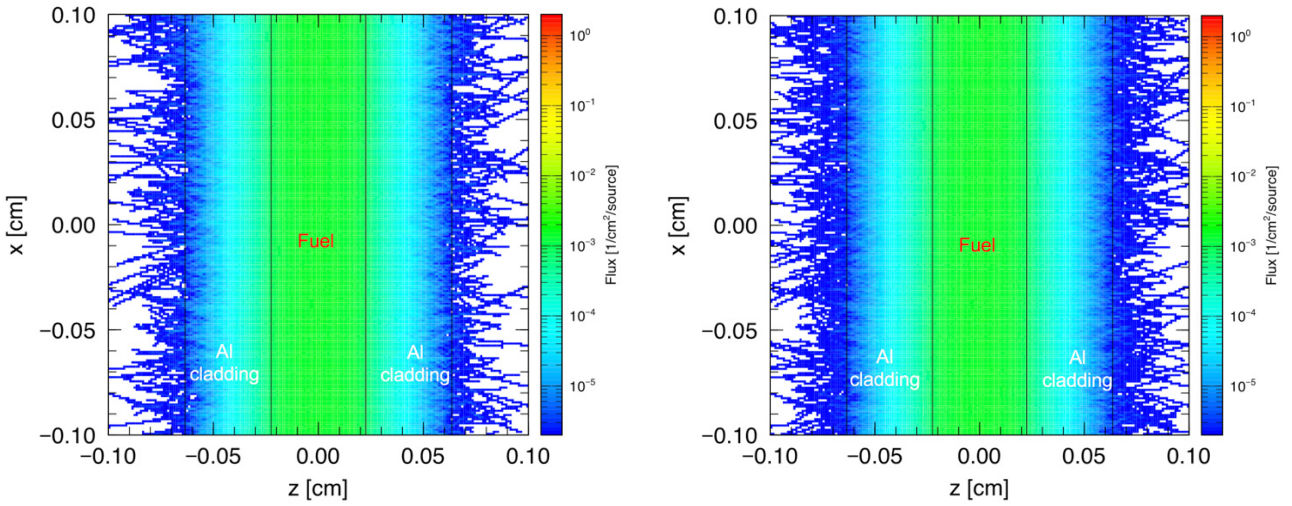

(1) Standard fuel plate of JMTR (2) Standard fuel plate of JRR-3M

Figure 4 – Triton 2D distribution

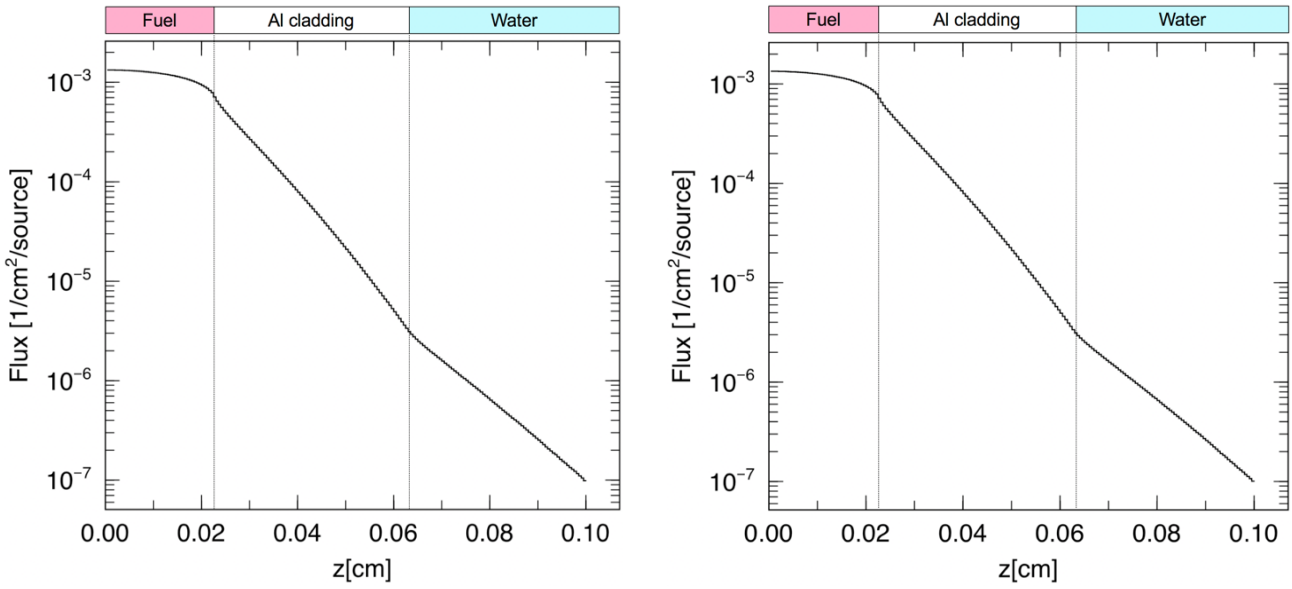

(1) Standard fuel plate of JMTR (2) Standard fuel plate of JRR-3M

Figure 5 – Triton 1D distribution

Table 3 – Calculation results

Items	JMTR	JRR-3M
Tritium production (Bq)	2.7×10^{9}	2.4×10^{8}
Tritium release rate	2.8×10^{-3}	2.8×10^{-3}
Released tritium (Bq)	7.6×10^{6}	6.5×10^{5}
Calculated value / measured value	$\sim10^{-4}$	$\sim10^{-4}$

In the calculations of tritium release rates into the water by PHITS, a gaussian triton energy by ternary fissions of ^{235}U, as shown in Figure 3, was selected [20]. The calculation results for standard fuel plates by PHITS are shown in Figure 4, Figure 5, and Table 3. Tritium release from fuels is about 10^7 and 10^6 Bq for the JMTR and JRR-3M, respectively.

3 Discussion

From the above calculation results, the tritium release from fuels for both the reactors is about 4 order of magnitude smaller than that of the measured value

(JMTR: ~10^{11} Bq, JRR-3M: ~10^{10} Bq). Therefore, it is clear that the tritium release from fuels for both the reactors is negligible, and that it is not necessary to consider as the source of tritium release.

4 Conclusions

To check the source for tritium release into the primary coolant during operation of the JMTR and the JRR-3M, the tritium release from the driver fuels are calculated by MCNP6 and PHITS. The following results were obtained.

- The calculated amount of tritium release from fuels are about 10^7 and 10^6 Bq for the JMTR and JRR-3M, respectively.
- The calculated values are about 4 order of magnitude smaller than that of the measured value.
- The tritium release from fuels for both the reactors is negligible. It is not necessary to consider the fuels as the source of tritium release.

References

1 E. Ishitsuka, J. Motohashi, Y. Hanawa, M. Komeda, S. Watahiki, A. Mukanova, I. Kenzhina and Y. Chikhray. Study of origin on tritium release into primary coolant for research and testing reactors. Tritium release rate evaluated from JMTR, JRR-3M and JRR-4 operation data // JAEA-Technology 2014-025. – 2014

2 E. Ishitsuka, H. Kawamura, H. Sugai, M. Tanase, H. Nakata. Experiments on tritium behavior in beryllium (2), -tritium released by recoil and diffusion // JAERI-M 90-013. – 1990.

3 I. Kenzhina et al. Evaluation of curve for tritium release rate into primary coolant of research and testing reactors // 4th Asian Symposium on Material Testing Reactors, Hanoi, Vietnam, 3-4 March 2016.

4 E. Ishitsuka, I. Kenzhina, K. Okumura, N. Takemoto, Y. Chikhray. Calculation by PHITS code for recoil tritium release rate from beryllium under neutron irradiation // JAEA-Technology 2016-022. – 2016.

5 Ishitsuka E., Kenzhina I. E. Evaluation of tritium release curve in primary coolant of research reactors // Physical Sciences and Technology. – 2018. – Vol. 4. – №. 1. – P. 27-33.

6 Serp J. et al. The molten salt reactor (MSR) in generation IV: overview and perspectives // Progress in Nuclear Energy. – 2014. – Vol. 77. – P. 308-319.

7 Sinha R. K., Kakodkar A. Design and development of the AHWR—the Indian thorium fuelled innovative nuclear reactor //Nuclear Engineering and Design. – 2006. – Vol. 236. – №. 7-8. – P. 683-700.

8 Terrani K. A., Zinkle S. J., Snead L. L. Advanced oxidation-resistant iron-based alloys for LWR fuel cladding // Journal of Nuclear Materials. – 2014. – Vol. 448. – №. 1-3. – P. 420-435.

9 Şahin S. et al. Neutronics analysis of HYLIFE-II blanket for fissile fuel breeding in an inertial fusion energy reactor //Annals of Nuclear Energy. – 2003. – Vol. 30. – №. 6. – P. 669-683.

10 Hu X. et al. Hydrogen permeation in FeCrAl alloys for LWR cladding application //Journal of Nuclear Materials. – 2015. – Vol. 461. – P. 282-291.

11 Gainey B. W. Review of tritium behavior in HTGR systems. – General Atomic Co., San Diego, Calif.(USA), 1976. – №. GA-A-13461.

12 Şahin S., Übeyli M. Modified APEX reactor as a fusion breeder //Energy conversion and management. – 2004. – Vol. 45. – №. 9-10. – P. 1497-1512.

13 Maeda Y. et al. Distinguished achievements of a quarter-century operation and a promising project named MK-III in Joyo //Nuclear Technology. – 2005. – Vol. 150. – №. 1. – P. 16-36.

14 Zarchy A. S., Axtmann R. C. Limitations on tritium transport through fusion reactors //Nuclear Technology. – 1978. – Vol. 39. – №. 3. – P. 258-265.

15 Murata I. et al. Fusion-driven hybrid system with ITER model //Fusion Engineering and Design. – 2005. – Vol. 75. – P. 871-875.

16 E. Ishitsuka, T. Sato, H. Sakurai, M. Saito, Y. Hutamura. Thermohydrodynamic characteristic analysis on the steady state condition of JMTR LEU fuel core // JAERI-M 92-043. –1992.

17 M. Kaminaga. Steady-state thermal hydraulic analysis and flow channel blockage accident analysis of JRR-3 silicide core // JAERI-Tech 97-015. –1997.

18 T. Goorley et al. Initial MCNP6 Release Overview. Nucl. Technol. – 2012. – Vol. 180. – P.298-315.

19 T. Sato, K. Niita, N. Matsuda, S. Hashimoto, Y. Iwamoto, S. Noda, T. Ogawa, H. Iwase, H. Nakashima, T. Fukahori, K. Okumura, T. Kai, S. Chiba, T. Furuta, L. Sihver. Particle and heavy ion transport code system PHITS, Version 2.52 // J. Nucl. Sci. Technol. – 2013. – Vol. 50(9). –P. 913-923.

20 P.D'hundt, C.Wagemans, A.Declercq, G.Barreau, A.Deruytter. Energy distributions and absolute yields of the charged light particles emitter during the thermal neutron induced ternary fission of ^{235}U // Nucl. Phys. –1980. – Vol. A346. –P.461-472.

IRSTI 29.03.30

Investigation of the low-temperature cyclohexane oxidation

M. Abbasi and N.A. Slavinskaya*

Institute of Combustion Technology, German Aerospace Center (DLR), Stuttgart, Germany
*e-mail: Nadja.Slavinskaya@dlr.de

The existence or non-existence of the negative temperature coefficient (NTC) region in cyclo-hexane (cyC_6H_{12}) oxidation is still an open question in the literature. This paper addresses this issue by presenting the rapid compression machine (RCM) and shock tube (ST) data and a consistent model to predict ignition delay times in agreement with experimental data. To this end, a semi-detailed chemical kinetic mechanism has been updated and improved to study the cyclohexane combustion at both low- and high-temperatures including polyromantic molecule (PAH) formation. The reaction mechanism is based on the 20 reaction classes; two of those were newly included in the model: cyclohexenyl peroxy formation and isomerization of hydroperoxy peroxy radical. For the main reaction classes, uncertainty boundaries of the rate coefficients have been evaluated. The NTC behavior observed in the RCM experiments was not detected in the ST measurements and in simulations performed with the developed model. The simulations performed with other literature models revealed that reaction models, which described the NTC region fixed in the RCM experiments, were unable to reproduce accurately the shock tube data. It is shown, that the cyC_6H_{12} oxidation chemistry is controlled by competition between three main reaction pathways over the full temperature interval. The developed model describes successfully laminar flame speed data and species profiles from burner-stabilized premixed flames.

Key words: cyclohexane, oxidation, polyaromatics, ignition, NTC.
PACS numbers: 07.20.Mc; 82.40.−g.

1 Introduction

Cycloalkanes (naphthenes) are an important chemical class of hydrocarbons found in conventional fuel mixtures like kerosene and diesel. They can affect the ignition quality of the fuel and can potentially raise soot emission levels due to their cyclic shapes. Therefore, the kinetic investigation of cyclohexane as the basic naphthene used in the models of commercial fuels has a great importance.

Table S1 in *Supplement-1* summarizes the main existing numerical investigations of the cyC_6H_{12} chemistry [1-10] accomplished with the experimental data [11-22] details used for the model validations. Despite of numerous investigations, up to now the published reaction models demonstrate significant discrepancies in the kinetic parameters and results. Thus the ignition delay time measurements performed in RCM [11, 17] and ST [16, 22] report contradictive information: NTC region observed in RCM was not detected in the ST experiments. To our knowledge, the published models were validated mostly on the data followed from RCM. An exception is reaction mechanism developed by Serinyel et al. [10] which was tested also on the ST low-temperature data of Daley et al. [16]. The indicated significant discrepancy between experiment and simulations was not analyzed in the study [10].

The main objective of this study is to revise and update the reaction pathways and rate coefficients of important reactions in the DLR kinetic model [23] and to establish the uncertainty quantified reaction mechanism of the cyC_6H_{12} oxidation with reasonable size to study the whole reactivity range. This model will be the base for the further extension to substituted, mono- and polycyclic napthenes. The investigation of the difference in the low-temperature data obtained in RCM and ST experiments is in the

focus of the present paper. By simulations of the experimental data with the updated mechanism and conducting chemical kinetic analyses the controlling reaction pathways responsible for autoignition at the lower temperature are identified and discussed.

The kinetic model was tested on the experimental data obtained in laminar flames. It delivers realistic predictions for cyclohexane combustion and due to its compactness meets the requirements of CFD simulations for technical combustion system.

Kinetic Model

The presented cyclohexane oxidation kinetic mechanism is a significant update of the model developed earlier in DLR [23]. The new model is based on the most recent C_0-C_3 chemistry studied by Slavinskaya et al. [24, 25, 26] and includes the PAH sub-model up to 5-ringed molecules.

Thermodynamic properties for several cyclic species were newly estimated and revised based on Benson's additivity approach including cyclic and bicyclic ring correction groups, reported in [27] , Table S2. The species transport properties were approximated using the group contribution algorithm of Joback et al. [28]. The full reaction mechanism, thermodynamic and transport data are provided in supplemental files (*Supplement_Mech, Supplement_therm, Supplement_trandat*).

Simulation of the experimental data was performed using the SENKIN and PREMIX packages of CHEMKIN II [29]. To model the ignition delay data obtained in RCM with the pressure profile, the chemical work bench (CWB) packages [30] have been used. For simulations of the ignition delay times measured in RCM, it was assumed that no reaction occurs during the compression stroke, heat losses are negligible and the constant volume assumption can be used. Simulations performed with the pressure profile shown the negligible effect of the pressure gradients on results. Constant-volume, homogeneous, and adiabatic conditions have been used to model the shock tube experiments.

2.1 High Temperature Sub-Mechanism

After sensitivity and rate of production analysis only 6 main reaction classes marked in Figure 1 were found to be important for high-temperature:

1. Unimolecular fuel decomposition, ring opening;
2. H-atom abstraction by O, H, OH, CH_3, CH_3O, C_2H_3, C_2H_5, O_2 leading to cycloalkyl radical, cyC_6H_{11};
3. Isomerization of cyC_6H_{11}, ring opening/β-scission of cyclic radicals;
4. Decomposition of unsaturated cyclic molecules;
5. Cascading dehydrogenation of cyC_6H_{11} (H-abstraction) leading to benzene (A1,C_6H_6);
6. cyC_6H_8 reactions to form, benzene

The kinetic rate parameters for reactions of type 1, as well as the further sequential unimolecular decompositions and β-scission reactions follow from the published literature reaction models [1, 3, 5, 6, 31, 32] . For cascading dehydrogenation steps, $cyC_6H_{11}\rightarrow cyC_6H_{10}\rightarrow cyC_6H_9\rightarrow\ldots\rightarrow$A1, due to the lack and high uncertainty level of data, the reaction coefficients were estimated, applying empirical rules proposed in [33] to evaluate the activation energy for H-abstraction reactions, *Supplement-2*. The pre-exponential factors were estimated based on the collision theory [34] using the numerical algorithm proposed in Cherny et al. [35].

2.2 Low Temperature Sub-Mechanism

Generally, cyclohexane exhibits low-temperature chemistry very similar to that of normal alkanes [36] with some cyclohexane specific reaction pathways like cyclohexanone and bicyclic ether formation. It was found [8, 9, 37] that the presence of the cyclic ring contributes to the activation energy barriers for some low-temperature reactions. It was considered at the rate coefficients evaluations, which were adopted mostly from investigations [4, 8, 9, 10, 32, 38, 39, 40] after the uncertainty analysis.

The main 14 reaction types were finally included in the scheme, Figure 2:

1. The O_2 addition to alkyl radical;
2. Isomerization of cyclic peroxy to hydroperoxy radical;
3. Decomposition $cyC_6H_{10}OOH\bullet$ radicals to cyclohexene and HO_2;
4. Decomposition $cyC_6H_{10}OOH\bullet$ radicals via ring opening to smaller species and OH radical;
5. Decomposition of $cyC_6H_{10}OOH\bullet$ and formation of cyclohexanone ($cyC_6H_{10}Od$) and 3 bicyclic ethers ($cyC_6H_{10}Oa,b,c$);
6. O_2 addition to $cyC_6H_{10}OOH\bullet$ with formation of $O_2QOOH\bullet$ type radicals;
7. Isomerization of $cyOOC_6H_{10}OOH$ to $cyC_6H_9(OOH)_2$
8. Decomposition of $cyOOC_6H_{10}OOH$ and $cyC_6H_9(OOH)_2$ to cyclic ketohydroperoxides ($cyOC_6H_9OOH$) and OH;
9. H-atom abstraction-cyclic ethers & cyclohexanone;
10. Decomposition of cyC_6H_9O;
11. Decomposition of $cyOC_6H_9OOH$ via ring opening;

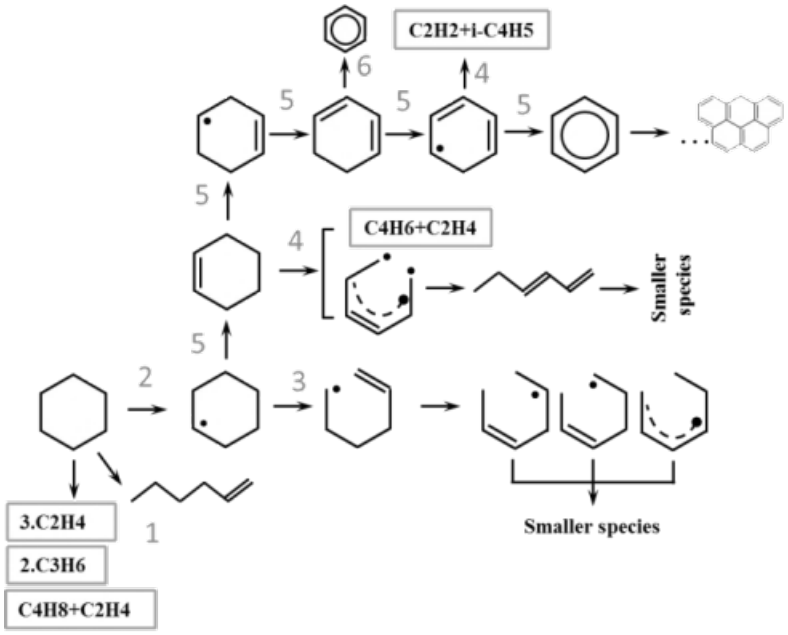

Figure 1 – Principal scheme of the high temperature oxidation of cyC_6H_{12}

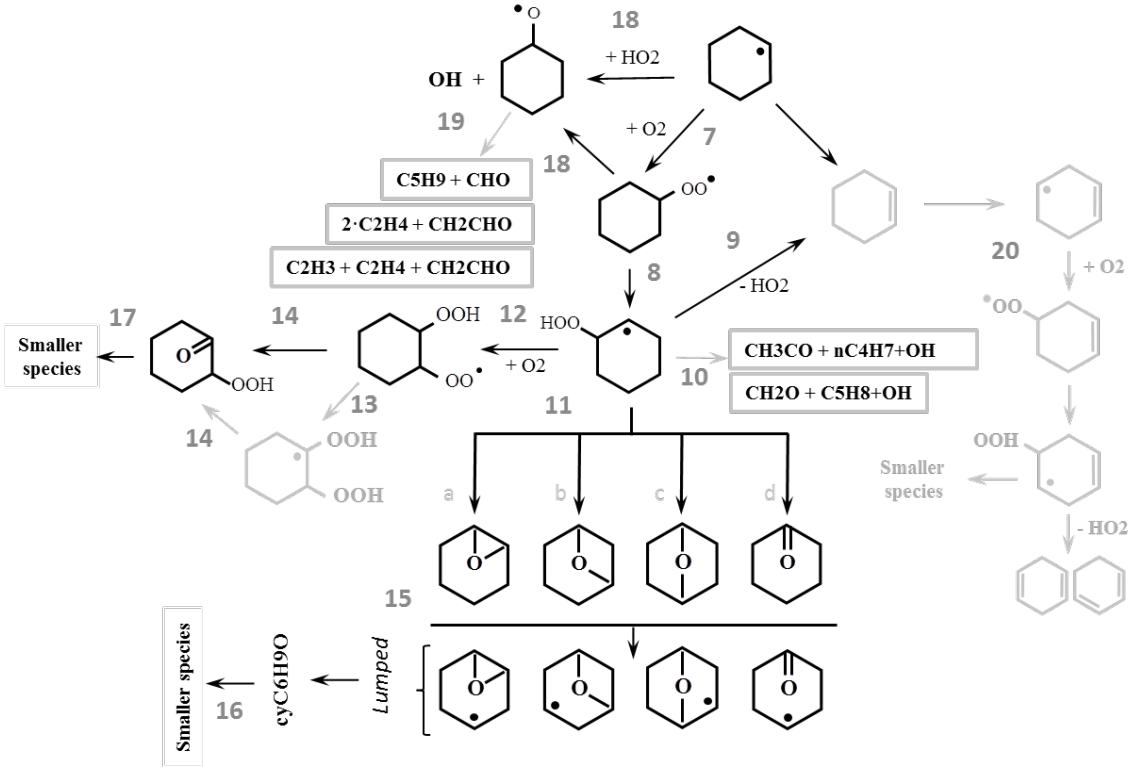

Figure 2 – Principal scheme of the low-temperature oxidation of cyC_6H_{12} with their new extensions (grey)

12. Formation of $cyC_6H_{11}O•$ from $cyC_6H_{11}OO$ and cyC_6H_{11};

13. Decomposition of $cyC_6H_{11}O•$ via ring opening;

14. The O_2 addition to cyC_6H_9.

The low-temperature reaction pathways earlier studied in [23] were revised and extended with the cyclohexenyl peroxy formation and isomerization of hydroperoxy peroxy radical, $cyOOC_6H_{10}OOH$, through the internal hydrogen transfer yielding more stable $cyC_6H_9(OOH)_2$ (type 13, Figure 2). The possible isomers of $cyC_6H_9(OOH)_2$ were grouped in a single lumped component, which dissociates into cyclic ketohydroperoxide and OH. This step was included in the scheme to multiply the chain propagation steps, and to increase the concentrations of less reactive HO_2 and cyclohexanone radicals (through the $cyOC_6H_9OOH$ decomposition) in the intermediate temperature zone.

Cyclohexene is mostly produced at the cascading cyclohexane dehydrogenation and at the HO_2 elimination from cyclohexylperoxy radical. Further that decomposes to cyclohexenyl, cyC_6H_9, which in turn after oxygen addition prolongs the low-temperature cyclohexene oxidation path competitive with the low-temperature hexyl oxidation. These two new added pathways, globally represented in the scheme in Figure 2, were not previously considered in detail in current understanding of low-temperature chemistry of cyclohexane. The related rate constants were evaluated as analogous to those for peroxy radicals, ROO and OOQOOH, applying cyclo-specific rate modification rules studied intensively by [8, 9, 37] (*Supplement_mech*).

2.3 Uncertainty Analysis

The upper f_u and lower f_l uncertainty boundaries of reaction rate coefficients have been evaluated through the statistical analysis of the literature data applying the non-linear weighted least squares method and its numeric realization FUMILI [41].

$$f_u(T) = log\frac{k_{upper}(T)}{k_0(T)}$$
$$f_l(T) = log\frac{k_0(T)}{k_{low}(T)} \quad (1)$$

here, k_0 is the nominal rate value, k_{low} and k_{upper} are lower and upper rate values from the dataset under consideration. This statistical assessment has been carried out, if a number of data sources exceeded 3. Table 1 summarises the clculated uncertainties. Detailed explanations about the applied method are provided in *Supplement-2*. These evaluated uncertainty intervals have been considered in the model improvement procedure. Table S3 reports parameters of the rate coefficients before and after modifications, and estimated uncertainty margins.

Table 1 – The lower and upper uncertainty factors of the rate coefficients of main reaction types

Reaction*	Type	$f_l(T)$	$f_u(T)$
$cyC_6H_{12} \rightarrow 3C_2H_4$	DE (1)	2.33-3.78	0.92-2.37
$cyC_6H_{12} \leftrightarrows aC_6H_{12}$	RN (1)	5.88-6.20	4.85-5.17
$cyC_6H_{12}+O_2 \leftrightarrows cyC_6H_{11} + HO_2$	HABS,INT (2)	2.47-2.65	2.44-2.62
$cyC_6H_{11} \leftrightarrows C_6H_{11}$	RN (3)	2.82-2.92	2.71-2.80
$cyC_6H_{11} \leftrightarrows cyC_6H_{10} + H$	DE (5)	3.38-3.57	3.07-3.26
$cyC_6H_{11}+O_2 \leftrightarrows cyC_6H_{10} + HO_2$	HABS (5)	1.68-1.79	1.66-1.77
$cyC_6H_{10} \leftrightarrows cyC_6H_9 + H$	DE (5)	3.11-3.21	2.82-2.92
$cyC_6H_{11}+O_2 \leftrightarrows cyC_6H_{11}OO$	ADD (7)	6.40-6.83	6.1-6.58
$cyC_6H_{11}OO \leftrightarrows cyC_6H_{10}OOH$	ISM (8)	3.34-3.85	3.31-3.82
$cyC_6H_{10}OOH \rightarrow CH_2O + C_5H_8 + OH$	BSC, RN (10)	4.28-4.73	3.33-3.78
$cyC_6H_{10}OOH \leftrightarrows OH+cyC_6H_{10}Oa$	DE-OH (11)	3.00-3.14	2.84-2.99
$cyOOC_6H_{10}OOH \leftrightarrows OH+ cyOC_6H_9OOH$	DE-OH (14)	2.87-2.92	2.77-2.82
$cyC_6H_{10}Oa+OH \leftrightarrows cyC_6H_9O+H_2O$	HABS (15)	0.89-0.93	0.88-0.93
$cyC_6H_{11}O \rightarrow CH_2CHO + 2C_2H_4$	DE,RN (19)	2.65-286	2.56-2.75

Abbreviations:
DE: Decomposition INT: Initiation HABS: H atom Abstraction RN: Ring-opening BSC: β- Scission ADD: Addition ISM: Isomerization DE-OH: Decomposition to release OH

3 Results and discussion

The performance of the current cyclohexane model was validated and optimized based on various types of experimental data [10-22], Table S4.

3.1 Ignition delay time

Rapid compression machine

The simulations of experimental data obtained in RCMs of [11, 17] revealed that unlike the mechanisms developed by Silke et al. [8] and Serinyel et al. [10], the studied model did not reproduce two stage ignition with NTC behavior.

The additive channels did not improve significantly trends in the ignition simulations, Figure 3, but made faster the ignition at T<800K: the additive O–OH bonds increase the number of OH radicals.

Generally, occurrence of NTC behavior in the hydrocarbon ignition is mainly controlled by the equilibrium of $cyC_6H_{11}+O_2 \leftrightarrows cyC_6H_{11}OO$. The shift in the reaction equilibrium to the $cyC_6H_{11}OO$ production favors the transition of the overall oxidation chemistry to the low-temperature kinetics. According to the used thermochemistry, the cyclohexyl peroxide production dominates on the whole investigated temperatures interval supporting the low-temperature mechanism of the small radical production. The temperature increase favors the reaction types 1-6 and reduces the peroxy radical concentration. That decreases the role of low-temperature reactions, but does not make it negligible. As a consequence, the region of gradient change (RGC) in the cyclohexane ignition behavior can be occurred as a response of the competition between low-and high-temperature reaction pathways. Instead the NTC regime, the smoothed conversion of the high-temperature oxidation to the low-temperature (an increase of reactivity with temperature decrease) is formed. The simulations of ignition delay data obtained in shock tubes support this conclusion.

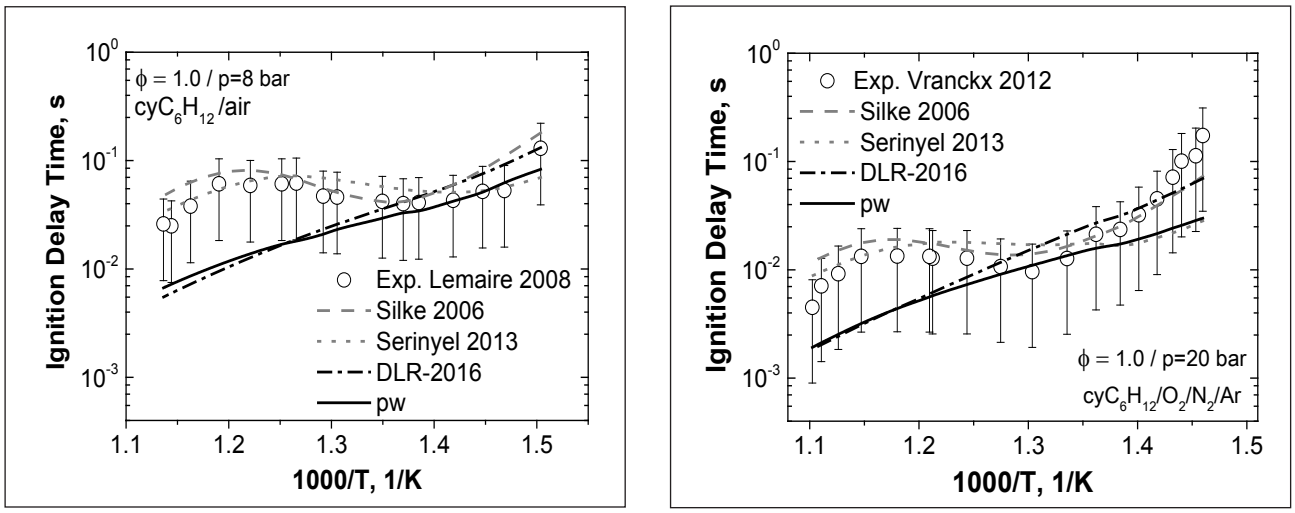

(a) (b)

Figure 3 – Cyclohexane ignition delay time from RCM experiments: a) p=8bar [11] b) p=20bar [17], versus simulations [8, 10], present work (pw)

Shock tube

The shock tube experiments performed by Daley et al. [16] and recently by Naumann et al. [22], Fig.4 and 5, do not demonstrate the NTC region, but the clear increase in reactivity with the temperature decrease, an indication of RGC, at T<900K, Fig. 4b and 5b. At higher pressure, a change in gradient reactivity is more pronounced, Fig.4b. This "slowdown" in ignition delay time gradient is caused by the three main competitive reaction pathways: the high-temperature formation of olefins and β-scission products; the chain branching peroxy- and hydroperoxy-radical reactions; and the cyclohexanone and bicyclic ethers ($cyC_6H_{10}Oa,b,c,d$) production. The reaction flux diagrams, Figure 6, indicate quite clearly these three pathways.

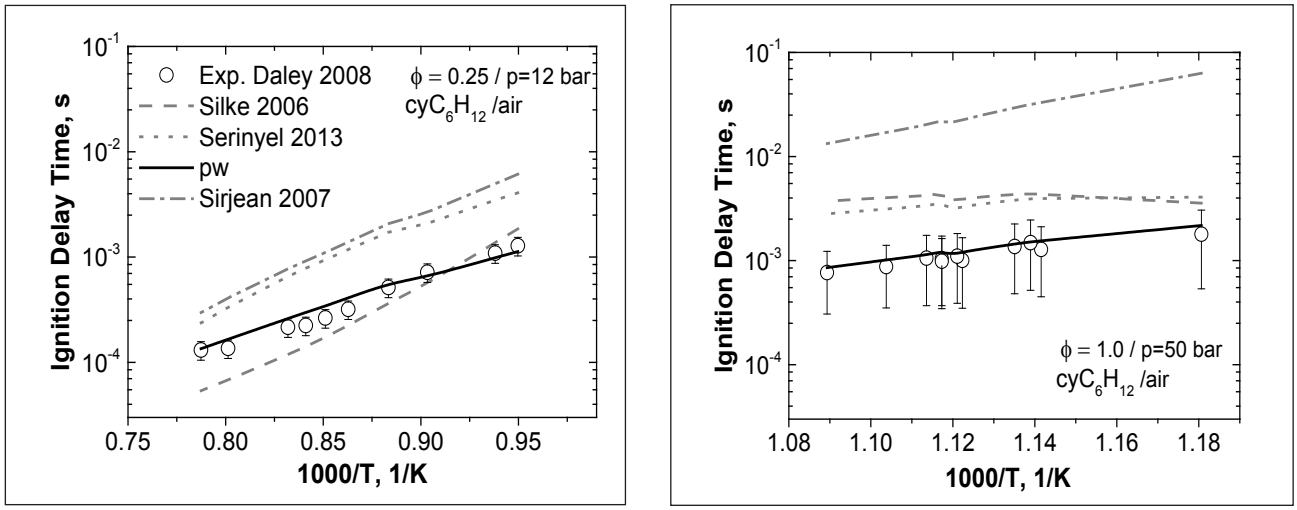

(a) (b)

Figure 4 – Comparison of ST autoignition data [16] with simulations [6, 8, 10], pw at: a) φ=0.25 , p=12bar; b) φ=1.0, p=50bar

At the low-temperature oxidation regime, Fig.6a, the cyclo-ketohydroperoxide chain-branching reaction path (starts with reaction type 12, see Figure 2) dominates and competes with the $cyC_6H_{10}Oa,b,c,d$ /chain-propagation paths (starts with reaction type 11, Figure 2).

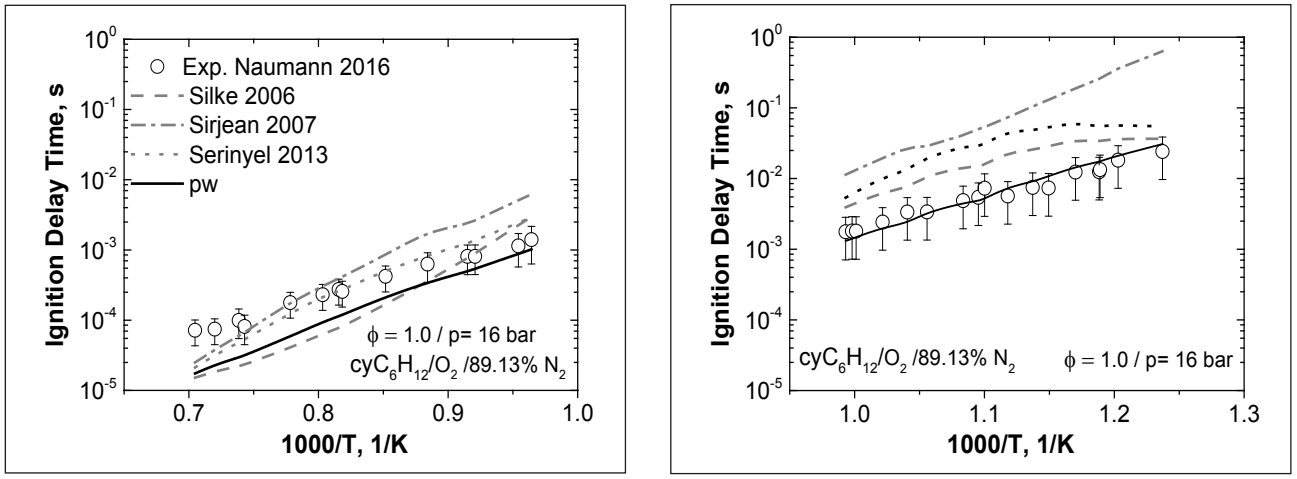

(a) (b)

Figure 5 – Comparison of ST autoignition data [22] with simulations [6, 8, 10], pw at: a)T=800-1010K b)T=1030-1420K

The new added reaction pathway, starting with cyC_6H_9OO formation (type 20, Figure2), influences the overall reaction for both temperature regimes, Fig.6a,b. It was pointed out that with the temperature increase the equilibrium constant of reaction $cyC_6H_{10}OOH \leftrightarrows cyC_6H_{10} + HO_2$ is shifted to the left side. It leads to the chain-propagation of cyclohexanone and bicyclic ethers, but not olefins and HO_2 radicals. As a consequence, cyclohexene starts two typical low-temperature scenarios, which prohibit the olefin accumulation and lead to the smoothed gradient change in the cyC_6H_{12} self-ignition behavior at 800 <T<1100K.

In both regimes, Fig.4 and 5, the experimental targets were perfectly regenerated by the current model. The models [8, 10] and of Sirjean et al. [6] overpre-

dict the ST ignition delay times and do not keep a trend. At higher temperature, T>900 K, models [6, 8, 10] are more successful by simulations, but tend to show a lower reactivity [6, 10]. It can be related to a) possible problems in thermodynamical properties; b) heightened concentrations of olefins, which should be produced in these models in large amount to reproduce the RCM experimental data [11, 17], Fig.3.

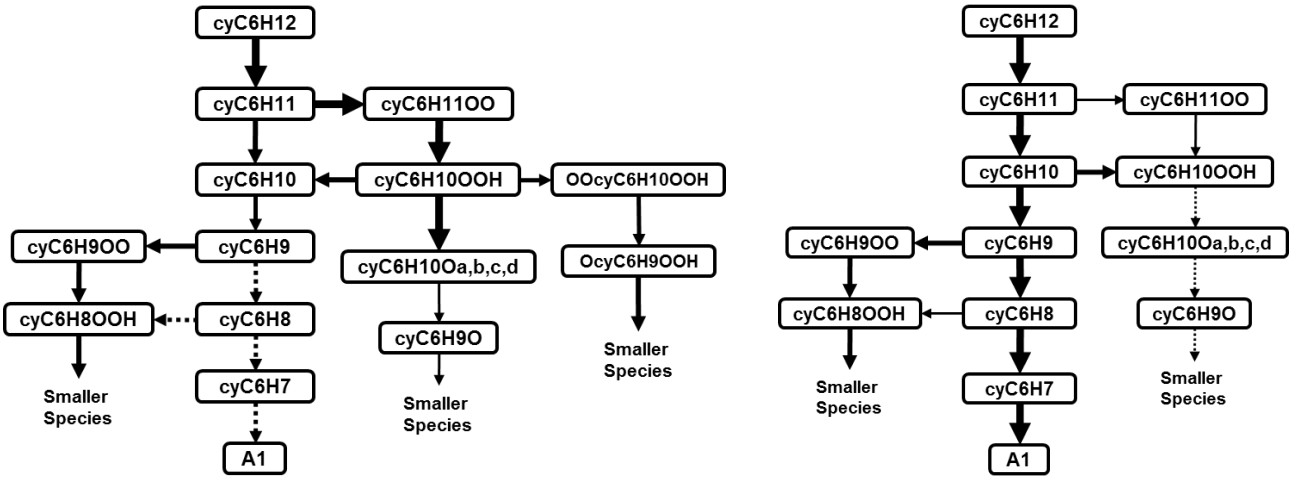

Figure 6 – Rate of production analysis in p = 16 atm and a) T=808 K and b) T=1389K

Laminar flame speed

The current mechanism has been also validated on the flame speed data from [10, 14, 15, 21]. The model demonstrates a good facilities to reflect the heat release in the system, describes datasets at atmospheric pressure and different preheated temperatures with a good agreement, Figure 7.

Flame structure

Figures 8 and 9 show simulations of the stabilized flames studied by Law et al. [13] and Ciajolo et al. [20]. In both cases the concentration profiles of important precursors of the PAH were successfully predicted with the present model.

The sensitivity and rate of production analysis have been carried out at three different temperatures along the given temperature profiles. It can be pointed out, that for T <1600K, the cascading dehydrogenation is the main reaction path to the benzene formation. The secondary ways lead to the substituted mono-aromatics after fuel decomposition to allene and acetylene. At the temperatures > 1600K, at the end of main reaction zone, the propargyl recombination controls the process of benzene formation, Figure 10.

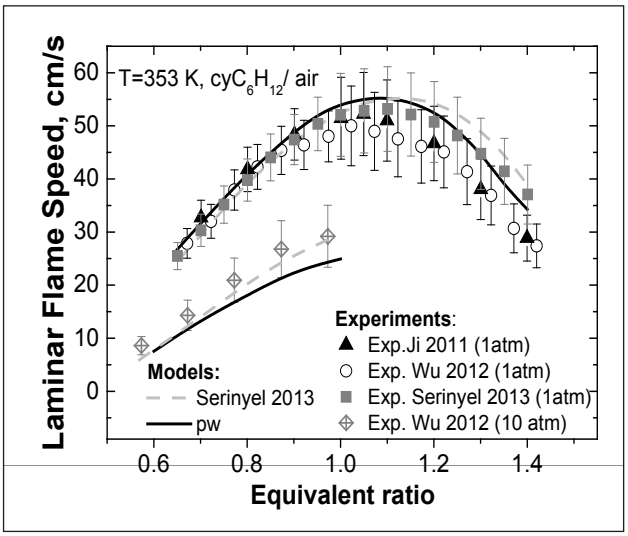

Figure 7 – Laminar flame speed data [10, 14, 15] compared with simulations [10],pw

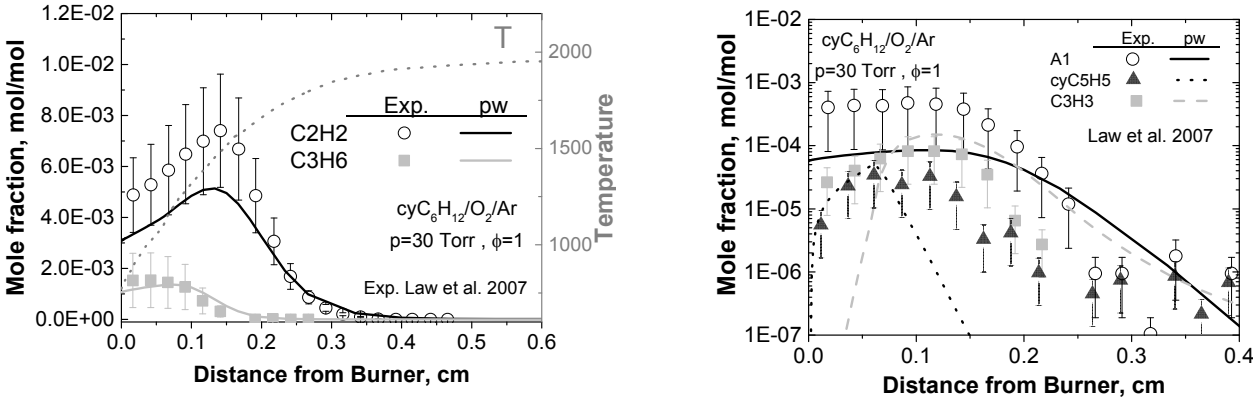

(a) (b)

Figure 8 – Species concentration profiles reported by [13] and the simulation results [pw]

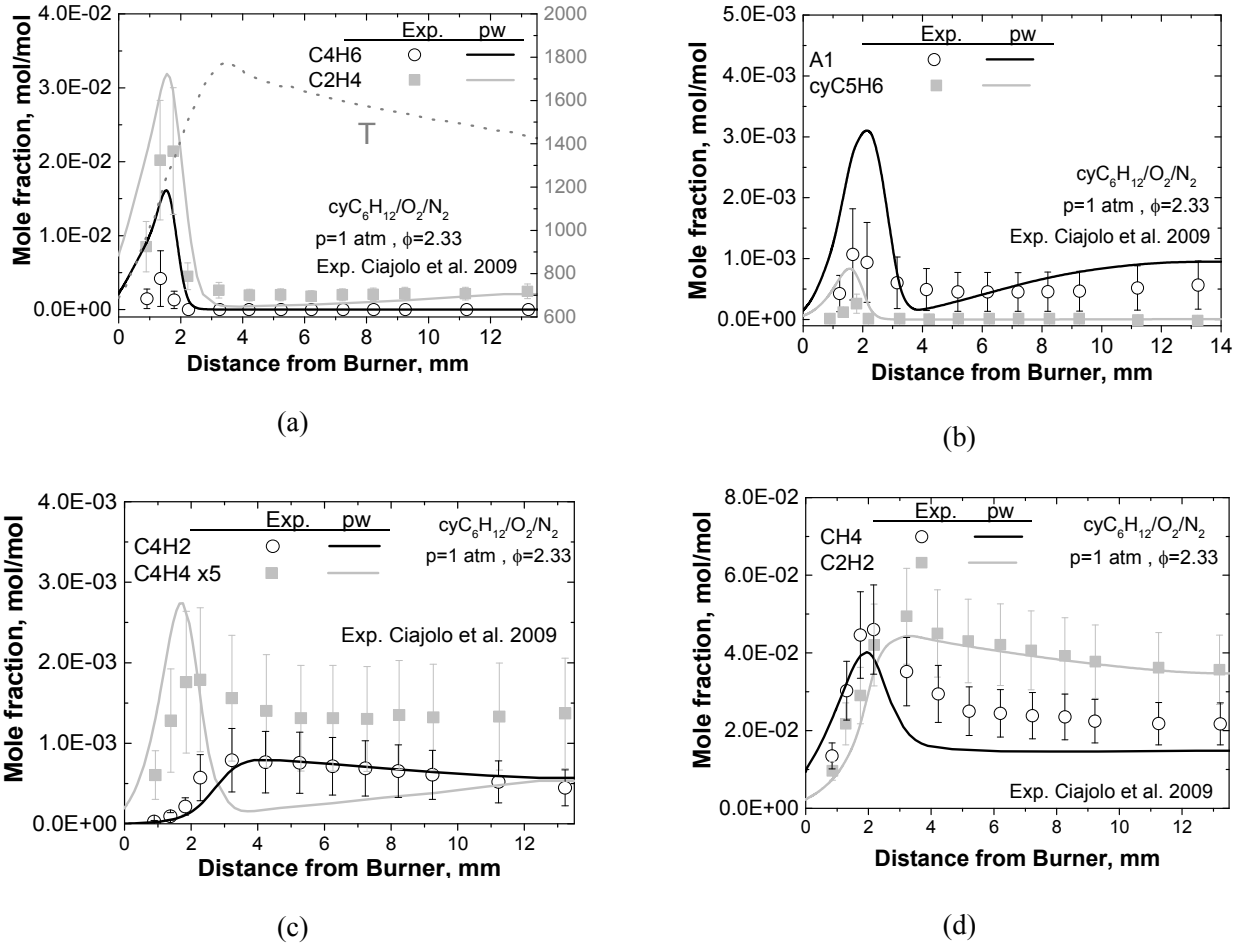

(a) (b)

(c) (d)

Figure 9 – Species concentration profiles reported by [20] and the simulation results [pw]

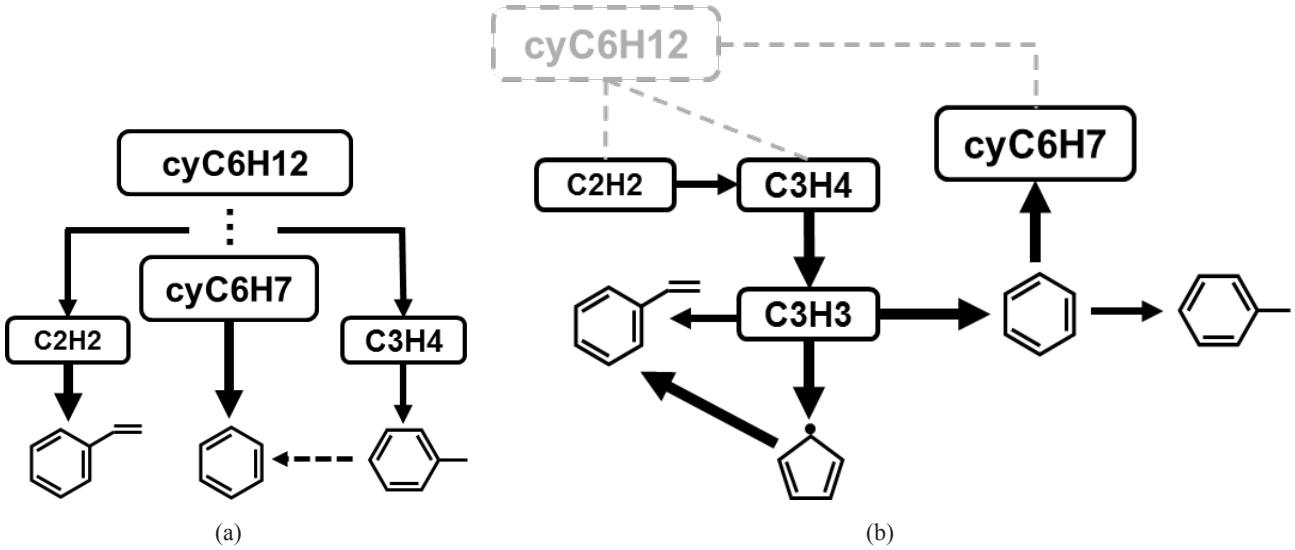

Figure 10 – Schematics of reaction path analysis performed for studied flames at a) temperature flame <1600K and b) temperature flame >1600K

4. Conclusions

This paper presents an updated semi-detailed kinetic mechanism for the cyclohexane oxidation at low, intermediate and high temperature. Two low-temperature reaction paths were newly included in the model: cyclohexenyl peroxy formation and isomerization of hydroperoxy peroxy radical. Special care has been taken to revise of rate parameters specific to cyclic alkanes and to evaluation of uncertainty intervals for the rate coefficients of most important reactions. The developed model satisfactorily reproduces the experimental data for ignition delay times, laminar flame speeds and concentration profiles measured in laminar flames. That makes it the particularly valuable for an explanation of the cyclohexane kinetics.

The equilibrium in the reaction of oxygen addition to cyC_6H_{11} is shifted to cyclohexyl peroxide production on the whole investigated temperatures interval, where three main competitive reaction pathways permanently control the ignition: the high-temperature formation of olefins and β-scission products; the chain branching peroxy- and hydroperoxy-radical reactions; and the cyclohexanone and bicyclic ethers production. The ignition simulations, thermochemistry, flow-rate and sensitivity analyses shown, that the competition of these three paths leads to the smoothed conversion of the high-temperature oxidation to the low-temperature. As the result, instead two stage ignition regime, the region of the gradient change (RGC) in the ignition behavior is occurred at 800<T<1100 K as a response to an increase of overall reactivity initiated by dominance of the chain branching peroxy- and hydroperoxy-radical reactions. Our numerical simulations are in accordance with the shock tube observations and support this conclusion. Further investigation of this matter would be very useful for the development of kinetic mechanisms for larger substituted naphthenes.

For T <1600K, the cascading dehydrogenation is the main reaction path to the benzene formation. The secondary ways lead to the substituted mono-aromatics after fuel decomposition to allene and acetylene. At the T > 1600K, the propargyl recombination controls the process of benzene formation.

References

1 D. Voisin, A. Marchal, M. Reuillon, J.-C. Boettner. Experimental and kinetic modeling study of cyclohexane oxidation in a JSR at high pressure // Combustion Science and Technology. – 1998. – Vol. 138. – P. 137-158

2 El Bakali, M. Braun-Unkhoff, P. Dagaut, P. Frank, M. Cathonnet. Detailed kinetic reaction mechanism for cyclohexane oxidation at pressure up to ten atmospheres // Proceedings of the Combustion Institute. – 2000. –Vol. 28. – P. 1631-1638.

3 Ristori, P. Dagaut, A. El Bakali, M. Cathonnet. The oxidation of n-propylcyclohexane: experimental results and kinetic modeling // Combustion Science and Technology. – 2001. – Vol. 165. – P. 197-228.

4 S. Granata, T. Faravelli, E. Ranzi. A wide range kinetic modeling study of the pyrolysis and combustion of naphthenes // Combustion and Flame. – 2003. – Vol. 132. – P. 533-544.

5 H. R. Zhang, L. Huynh, N. Kungwan, Z. Yang, S. Zhang. Combustion modeling and kinetic rate calculations for a stoichiometric cyclohexane flame.1. Major reaction pathways // J. Phys. Chem. A. – 2007. – Vol. 111. – P. 4102-4115.

6 Sirjean, F. Buda, H. Hakka, P. Glaude, R. Fournet, V. Warth, F. Battin-Leclerc, M. R. Lopez. The autoignition of cyclopentane and cyclohexane in a shock tube // Proceedings of the Combustion Institute. – 2007. – Vol. 31. – P. 277-284.

7 Cavallotti, R. Rota, T. Faravelli, E. Ranzi. Ab initio evaluation of primary cyclo-hexane oxidation reaction rates // Proceedings of the Combustion Institute. – 2007. – Vol. 31.– P. 201-209.

8 J. Silke, W. J. Pitz, C. K. Westbrook, M. Ribaucour. Detailed chemical kinetic modeling of cyclohexane oxidation // J. Phys. Chem. A. – 2007. – Vol. 111.– P. 3761-3775.

9 Buda, B. Heyberger, R. Fournet, P. Glaude, V. Warth, F. Battin-Leclerc. Modeling of the gas-phase oxidation of cyclohexane // Energy & Fuels. – 2006. – Vol. 20. – P. 1450-1459.

10 Z. Serinyel, O. Herbinet, O. Frottier, P. Dirrenberger, V. Warth, P. Glaude, F. Battin-Leclerc. An experimental and modeling study of the low- and high-temperature oxidation of cyclohexane // Combustion and Flame. – 2013. – Vol. 160. – P. 2319-2332.

11 O. Lemaire, M. Ribaucour, M. Carlier, R. Minetti. The production of benzene in the low-temperature oxidation of cyclohexane, cyclohexene, and cyclohexa-1,3-diene // Combust and Flame. – 2001. – Vol. 127.– P. 1971-1980.

12 S. G. Davis and C. K. Law. Determination of and fuel structure effects on laminar flame speeds of C1 to C8 hydrocarbons // Combustion Science and Technology. – 1998. – Vol. 140. – P. 427-449.

13 M. E. Law, P. R. Westmoreland, T. A. Cool, J. Wang, N. Hansen and T. Kasper. Benzene precursors and formation routes in a stoichiometric cyclohexane flame // Proceedings of the Combustion Institute. – 2007. – Vol. 31. – P. 565-573.

14 C. Ji, E. Dames, B. Sirjean, H. Wang and F. Egolfopoulos. An experimental and modeling study of the propagation of cyclohexane and mono-alkylated cyclohexane flames // Proceedings of the Combustion Institute. – 2011. – Vol. 33. – P. 971-978.

15 Wu, A. Kelley and C. Law. Laminar flame speeds of cyclohexane and mono-alkylated cyclohexanes at elevated pressures // Combust and Flame. – 2012. – Vol. 159. – P. 1417-1425.

16 S. Daley, A. Berkowitz and M. Oehlschlaeger. A shock tube study of cyclopentane and cyclohexane ignition at elevated pressures // International Journal of Chemical Kinetics. – 2008. – Vol. 40. – P. 624–634.

17 S. Vranckx, C. Lee, H. Chakravarty and R. Fernandes. A rapid compression machine study of the low temperature combustion of cyclohexane at elevated pressures // Proceedings of combuston institute. – 2012. – Vol. 34. – P. 377-384.

18 Z. Hong, K.-Y. Lam, D. Davidson and R.K. Hanson. A comparative study of the oxidation characteristics of cyclohexane, methylcyclohexane, and n-butylcyclohexane at high temperatures // Combust. Flame. – 2011. – Vol. 158. – P. 1456-1468.

19 S. Zeppieri, K. Brezinsky and I. Glassman. Pyrolysis studies of methylcyclohexane and oxidation studies of methylcyclohexane and methylcyclohexane/toluene blends // Combustion and Flame. – 1997. – Vol. 108. – P. 266-286.

20 Ciajolo, A. Tergrossi, M. Mallardo, T. Faravelli and E. Ranzi. Experimental and kinetic modeling study of sooting atmospheric-pressure cyclohexane flame // Proceedings of the Combustion Institute. – 2009. – Vol. 32. – P. 585-591.

21 S. Richter, M. B. Raida, C. Naumann and U. Riedel. Measurement of the laminar burning velocity of neat jet fuel components // Proceedings of the World Congress on Momentum, Heat and Mass Transfer (MHMT'16). – 2016. – Vol. 115. – P. 1-5.

22 C. Naumann and e. al. InnoTreib – innovative treibstoffe der zukunft // Bundesministerium für Wirtschaft und Energie (BMWi) Interim reports AP 4.2 and AP 6. – 2016.

23 M. Abbasi, N. A. Slavinskaya, U. Riedel. Kinetic modeling of cyclohexane oxidation including PAH formation // Proc. of 55th AIAA Aerospice sciences meeting 08.-13.01.2017. Grapevine, TX, USA – 2017, -P. 0838.

24 N. Slavinskaya, U. Riedel, S. Dworkin, M. Thomson. Detailed numerical modelling of PAH formation and growth in non-premixed ethylene and ethane flames // Combust. Flame. – 2011. – Vol. 159. -No.57. -Pp. 979-995.

25 N. A. Slavinskaya, M. Abbasi, J. H. Starcke, R. Whitside, A. Mirzayeva, U. Riedel, W. Li, J. Oreluk, A. Hegde, A. Packard, M. Frenklach, G. Gerasimov and O. Shatalov. Development of an UQ-predictive chemical reaction model for syngas combustion // Energy&Fuels. – 2016. – Vol. 3. – P. 2274-2297.

26 N.A.Slavinskaya, V. Chernov, R. Whitside, J.H. Starke, A. Mirzayeva, M. Abassi, M. Auyelkhankyzy. A modeling study of acetylene oxidation and pyrolisys // Combustion and Flame (submitted).

27 S. Benson. Thermochemical kinetics // 2nd ed., New Yorck, USA: John Wiley & Sons Ltd. – 1976.

28 K. Joback, R. Reid. Estimation of pure-component properties from group-contributions // Chemical Engineering Communications. – 1987. – Vol. 57. – P. 233-243.

29 R. Kee, F. Rupley, J. A. Miller. Sandia Laboratories Report, Sandia National Laboratories, Albuquerque, NM, 1993.

30 "Chemical Work Bench, Software Package, Ver. 4.1," Kintech Lab, Ltd., [Online]. Available: http://www.kintechlab.com/products/chemical-workbench. [Accessed 2017].

31 B. Sirjean, P. A. Glaude, M. F. Ruiz-Lopez and R. Fournet. Theoretical kinetic study of thermal unimolecular decomposition of cyclic alkyl radicals // J. Phys. Chem. A.– 2008. – Vol. 112. – P. 11598-11610.

32 Dayma, P. A. Glaude, R. Fournet, F. Battin-Leclerc. Experimental and modeling study of the oxidation of cyclohexene // International Journal of Chemical Kinetics. – 2003. – Vol. 7. – P. 273-285.

33 Y. Zhorov. Thermodynamics of chemical processes, petrochemical, synthesis, processing of petroleum, coal and natural gas // 1 ed., Moscow, Russia: Mir. – 1987. – P. 248.

34 M. Trautz, Z. Anorg. Evaluation of Arrhenius frequency factor (A) by simple collision theory // Chemistry. –1916. – Vol. 1. –P.1.

35 Chernyi, S. Losev, S. Macheret, B. Potapkin. Physical and chemical processes in gas dynamics : cross sections and rate constants: American institute of aeronautics & astronautics // AIAA. – 2012.

36 C. K. Westbrook, J. Warnatz and W. Pitz. A detailed chemical kinetic reaction mechanism for the oxidation of iso-octane and n-heptane over an extended temperature range and its application to analysis of engine knock // Proc. Combust. Inst. – 1989. – Vol. 22. – P. 893-901.

37 W. J. Pitz, C. Naik, T. Ní Mhaoldúin, C. Westbrook, H. J. Curran, J. Orme and J. M. Simmie. Modeling and experimental investigation of methylcyclohexane ignition in a rapid compression machine // Proc. Combust. Inst.– 2007. – Vol. 31. – P. 267-275.

38 E. Ranzi, T. Faravelli, P. Gaffuri and A. Sogaro. A wide-range modeling study of iso-octane oxidation // Combustion and Flame. – 1997. – Vol. 108. – P. 24-42.

39 Curran, P. Gaffuri, W. Pitz and C. Westbrook. A comprehensive modeling study of iso-octane oxidation // Combustion and Flame. – 2002. – Vol. 129. – P. 253-280.

40 D. Matheu, W. H. Green and J. Grenda. Capturing pressure-dependence in automated mechanism generation: reactions through cycloalkyl intermediates // Int. J. Chem. Kinet. – 2003. – Vol. 35. – P. 95.

41 V. Kurbatov und I. Silin. // Nuclear Instruments and Methods in Physics Reserach A, Bd. – 1994. – Vol. 345. – P. 346-350.

Supplementary Materials 1

Table S1 – Kinetic mechanisms and their experimental validations [1-20] (ST = Shock tube, RCM = Rapid Compression Machine, PFR = Plug Flow Reactor, JSR = Jet Stirred Reactor)

Model	Validation				
	ST	**RCM**	**PFR**	**JSR**	**Flame Structure**
Voisin et al. [1]				**Concentration profile [1]** **T=** 750-1100 K, **τ** =0.5 s **p=** 10atm, **φ=**0.5, 1.0, 1.5 **Mixture:** 0.1% cyC_6H_{12}/ O_2/N_2	
El Bakali et al. [2]				**Concentration profile [2]** **T=** 750-1200 K, **τ** =0.07-0.5 s **p=** 1, 2, 10atm, **φ=**0.5, 1.0, 1.5 **Mixture:** 0.15% $cyC_6H_{12}/O_2/N_2$	**Flame Speed [12]** **T=** 298 K **,** **p=** 1atm **Mixture:** cyC_6H_{12}/ air
Ristori et al. [3]				**Concentration profile [3]** **T=** 980-1200 K **p=** 1atm, **φ=**1.0, **τ** =0.07 s **Mixture:** 0.15% $cyC_6H_{12}/O_2/N_2$	
Granata et al. [4]		**Ignition delay time [11]** **p=** 7-9 bar **T=** 650-900 K **, φ=**1.0 **Mixture:** cyC_6H_{12}/ air	**Concentration profile [19]** **T=** 1155 K**, P=** 1atm **Mixture (pyrolysis):** 0.166 %cyC_7H_{14} in N_2 **T=** 1160 K**, p=** 1atm **Mixture:** 0.185% cyC_7H_{14}/1.9% O_2 in N_2	**Concentration profile [1,2]** **T=** 800-1200 K **P=** 1-10atm**,** **φ=**0.5, 1.0, 1.5	**Flame Speed [12]** **T=** 298 K **, p=** 1atm **Mixture:** cyC_6H_{12}/ air
Zhang et al. [5]					**Concentration profile [13]** **T=** 1000 K**,** **p=** 30 Torr **φ=**1.0, 2.0
Sirjean et al. [6]	**Ignition delay time [6]** **T=** 1200-1850 K **P=** 7-9 bar , **φ=**0.5, 1, 2 **Mixture:** 0.5% cyC_6H_{12}/O_2/Ar				

Cavallotti et al. [7]		**Ignition delay time [11]** **p**= 7-9, 11-14 bar **T**= 700-1000 K, **φ**=1.0 **Mixture:** cyC_6H_{12}/ air		**Concentration profile [2]** **T**= 800-1200 K **p**= 1-10atm , **φ**=0.5, 1.0, 1.5	
Silke et al. [8]		**Ignition delay time [11]** **p**= 7-9, 11-14 bar **T**= 700-1000 K, **φ**=1.0 **Mixture:** cyC_6H_{12}/ air		**Concentration profile [1]** **T**= 850-1070 K **,** **P**= 2.0 ,10atm **φ** = 0.5, 1.0, 1.5, **τ** =0.5 s **Mixture:** 0 .1% $cyC_6H_{12}/O_2/N_2$ **Concentration profile [2]** **T**= 800-1100 K, **τ** =0.25 s **p**= 5atm, **φ**= 1.0 **Mixture:** 0.15% $cyC_6H_{12}/O_2/N_2$	
Buda et al.[9]		**Ignition delay time [11]** **p**= 0.7-0.9/ 1.1-1.4 MPa **T**= 700-1000 K, **φ**=1.0 **Mixture :** cyC_6H_{12}/ air		**Concentration profile [1]** **T**= 850-1070 K , **p**= 10atm **φ** = 0.5, 1.0, 1.5 , **τ** =0.5 s **Mixture:** 0.1% $cyC_6H_{12}/O_2/N_2$	
Serinyel et al. [10]	**Ignition delay time [5]** **T**= 1200-1850 K **p**= 7-9bar, **φ**=0.5, 1, 2 **Mixture :** 0.5% cyC_6H_{12}/O_2 in Ar **Ignition delay time [17]** **T**= 950-1200 K **p**= 13-15 bar, **φ**=0.5, 1.0 **Mixture:** cyC_6H_{12}/ air **Ignition delay time [19]** **T**= 950-1200 K **p**= 1.5,3 bar, **φ**=0.5, 1.0 **Mixture :** $cyC_6H_{12}/4\%O_2/Ar$	**Ignition delay time [11]** **p**=11-14 bar **T**= 700-1000 K, **φ**=1.0 **Mixture:** cyC_6H_{12}/ air **Ignition delay time [18]** **T**= 600-900K, **φ** = 0.5,1,2 **p** = 12.5, 20, 40 bar **Mixture:** 2.26% $cyC_6H_{12}/O_2/N_2$		**Concentration profile [10]** **T**= 500-1100 K **P**= 1.07 bar , **τ** = 2 s **φ** = 0.5,1.0,2 **Mixture :** 0.667% $cyC_6H_{12}/O_2/N_2$	**Flame Speed [10]** **T**= 298,358, 398 K **p**= 1atm, **Mixture:** cyC_6H_{12}/ air **Flame Speed [12]** **T**= 298 K , **p**= 1atm **Mixture:** cyC_6H_{12}/ air **Flame Speed [14]** **T**= 353 K , **p**= 1atm **Mixture:** cyC_6H_{12}/ air **Flame Speed [15]** **T**= 353 K , **p**= 2,5, 10atm **Mixture:** cyC_6H_{12}/ air

Table S2 – Thermodynamic properties of cyclohexane relevant sub-model species

Species	ΔH^0_f / kJ·mol^{-1}	S^0 / J·mol^{-1}·K^{-1}	$C_p(T)$ /J·mol^{-1}·K^{-1})						
			300	**400**	**500**	**600**	**800**	**1000**	**1500**
cyC_6H_{11}	54.71	314.94	108.93	151.45	187.74	219.29	269.63	303.40	351.87
cyC_6H_{10}	-2.43	312.26	104.90	145.14	178.48	206.48	249.21	278.78	322.94
$cyC_6H_{11}O$	-68.23	331.55	119.54	165.33	204.39	238.41	292.65	327.12	377.29
$cyC_6H_{11}OO$	-83.07	365.14	128.43	175.69	216.32	251.33	305.45	341.77	401.12
$cyC_6H_{10}OOH$	-37.22	398.44	146.93	196.34	236.73	271.05	325.60	361.62	413.25
$cyOOC_6H_{10}OOH$	-179.92	441.33	162.45	214.36	256.87	292.58	347.54	382.68	443.32
$cyOOHC_6H_9OOH$	-136.14	472.73	168.99	218.78	260.29	295.34	349.00	393.86	430.91
$cyOC_6H_9OOH$	-332.26	410.57	150.61	197.32	233.21	263.51	314.66	346.45	404.90
cyC_6H_9OO	35.52	373.69	122.98	165.82	201.03	230.15	273.21	302.46	352.99
cyC_6H_8OOH	26.75	376.78	136.64	180.67	214.31	241.36	282.46	308.52	348.41
a-$cyC_6H_{10}O$	-125.81	284.42	118.94	163.80	201.43	232.90	279.48	311.26	369.62
b-$cyC_6H_{10}O$	-140.38	258.55	115.32	158.71	197.13	229.69	276.23	308.84	368.45
c-$cyC_6H_{10}O$	-220.08	227.65	111.26	155.67	194.99	228.12	274.82	307.84	367.71
d-$cyC_6H_{10}O$	-235.41	334.39	116.59	158.66	192.67	222.26	272.58	305.52	362.85
cyC_6H_9	131.45	313.62	97.80	132.26	163.44	190.17	228.81	257.17	298.06
cyC_6H_8	134.28	274.10	75.33	102.35	126.05	145.68	172.49	191.92	219.07
cyC_6H_7	200.56	305.77	97.56	129.46	156.63	178.98	210.14	232.58	263.86

Table S4 – Experimental data used for validations

Exp.	Validation		
	ST	**RCM**	**Flame Structure**
Law et al. [13]			**Concentration profile** **T=** 1000 K**, p=** 30 Torr**, φ=**1.0 **Mixture:** cyC_6H_{12}/O_2 in 32.5% Ar **MFR**=0.00214 g.cm^{-2}.s^{-1} UNC: ±20 -50%
Vranckx et al. [17]		**Ignition delay time** **T=** 600-900 K, **φ** = 1.0, **p=** 20 bar **Mixture:** 2.26% $cyC_6H_{12}/O_2/N_2$ UNC: ±50% -70%	
Lemaire et al. [11]		**Ignition delay time** **p=** 8 bar, **T=** 650-900 K **, φ=**1.0 **Mixture:** cyC_6H_{12}/ air UNC: ±40% – 60%	

Sirjean et al.[6]	**Ignition delay time** **T=** 1230-1840 K**,** **P=** 8atm **, φ=**0.5, 2.0 **Mixture:** 0.5% cyC_6H_{12}/O_2/Ar UNC: ±30 – 40%		
Ciajolo et al. [20]			**Concentration profile** **T=** 700 K**, p=** 1 atm**, φ=**2.33 **Mixture:** cyC_6H_{12}/O_2/39.4% N_2 **MFR**=0.00283 $g.cm^{-2}.s^{-1}$ UNC: ±20 – 50%
Richter et al. [21]			**Flame Speed** **T=** 473 K**, p=** 1 atm **Mixture:** cyC_6H_{12}/ air UNC: ±10%
Naumann et al. [22]	**Ignition delay time** **T=** 800-1400 K**,** **p=** 16atm**, φ=**1.0 **Mixture:** cyC_6H_{12}/O_2/ 89% N_2 UNC: ±30 – 60%		
Daley et al. [16]	**Ignition delay time** **T=** 950-1200 K **p=** 13-15 bar, **φ=**0.25, 0.5, 1.0 **Mixture :** cyC_6H_{12}/ air UNC: ±20 – 40%		
Wu et al. [15]			**Flame Speed** **T=** 353 K **, p=** 1.0, 10 atm **Mixture:** cyC_6H_{12}/ air UNC: ±10% , ±20
Ji et al. [14]			**Flame Speed** **T=** 353 K **, p=** 1.0 atm **Mixture:** cyC_6H_{12}/ air UNC: ±10%
Serinyel et al. [10]			**Flame Speed** **T=** 358 K**, p=** 1atm, **Mixture:** cyC_6H_{12}/ air UNC: ±10%

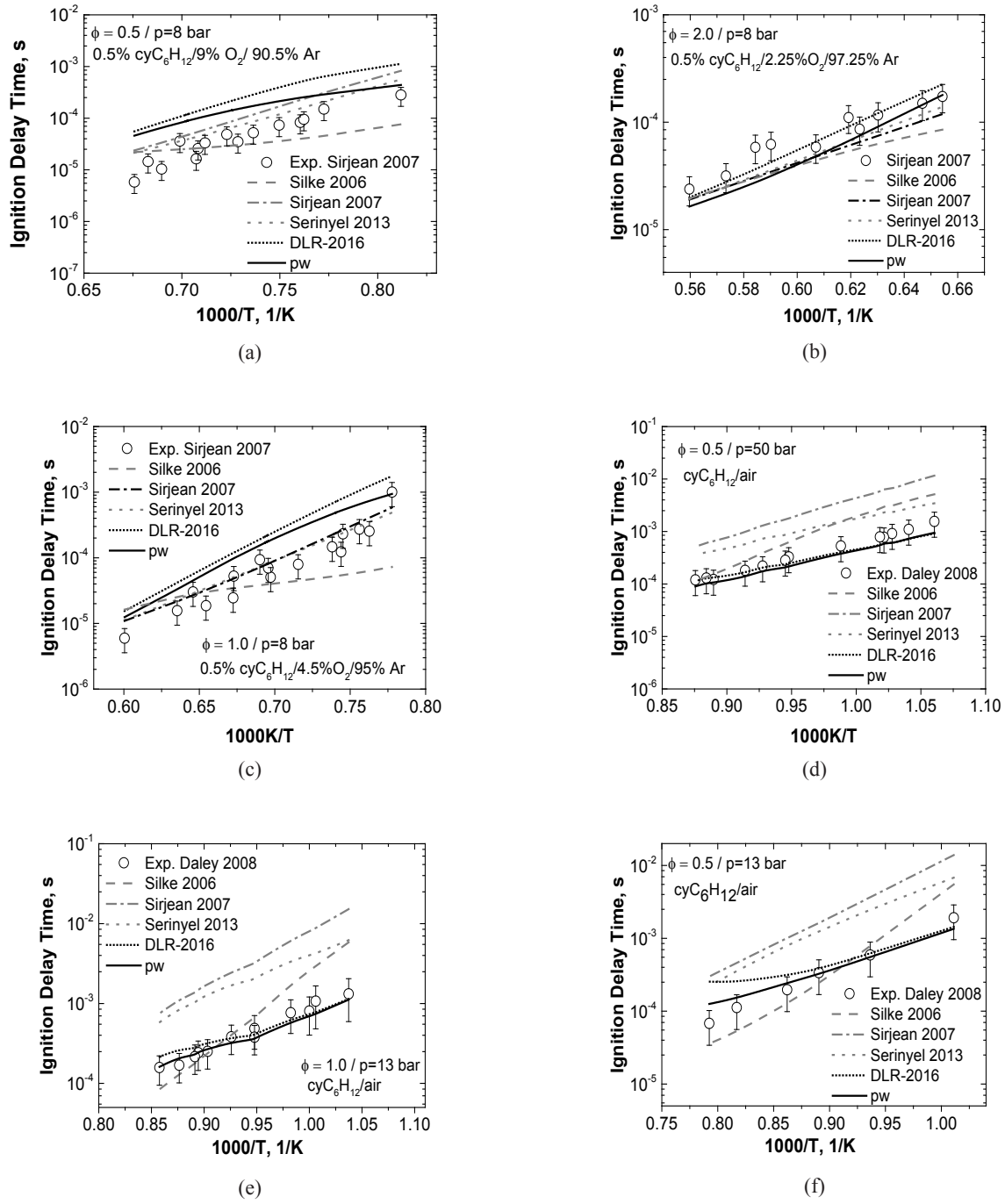

Figure S1 – Comparison of ST autoignition data [6,16] with simulations [6,8,10,23,pw]

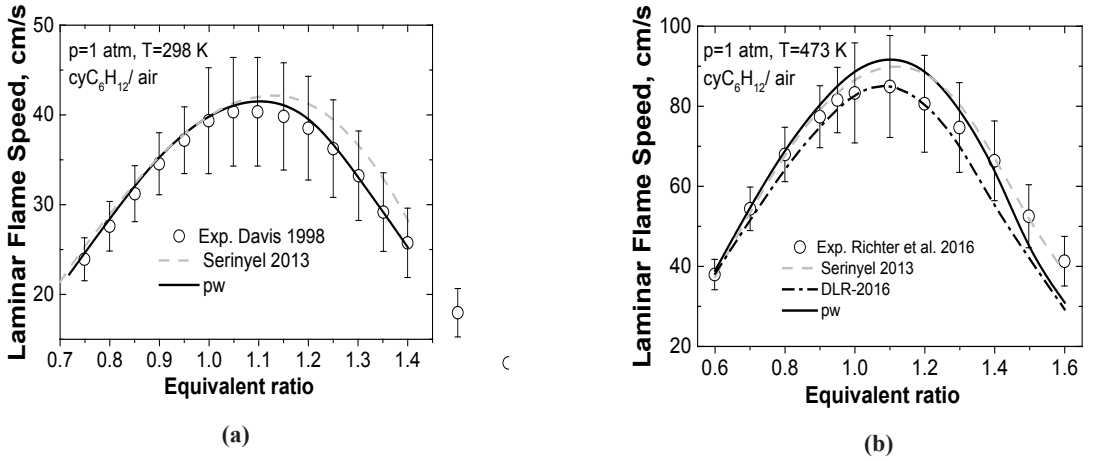

Figure S2 – Laminar flame speed data [12, 21] compared with simulations [10,23,pw].

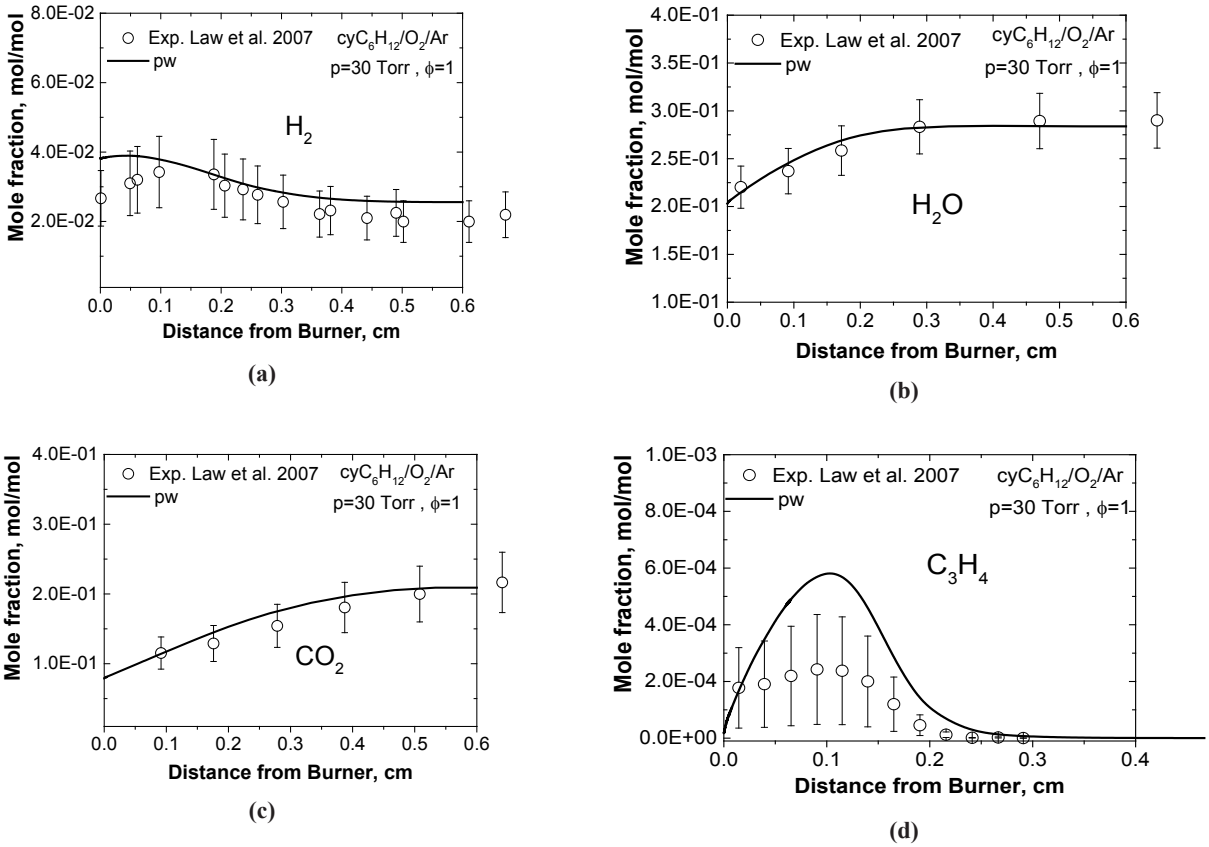

Figure S3 – Concentration profiles of species measured in burned stabilized flame of [13] and the simulation results [pw].

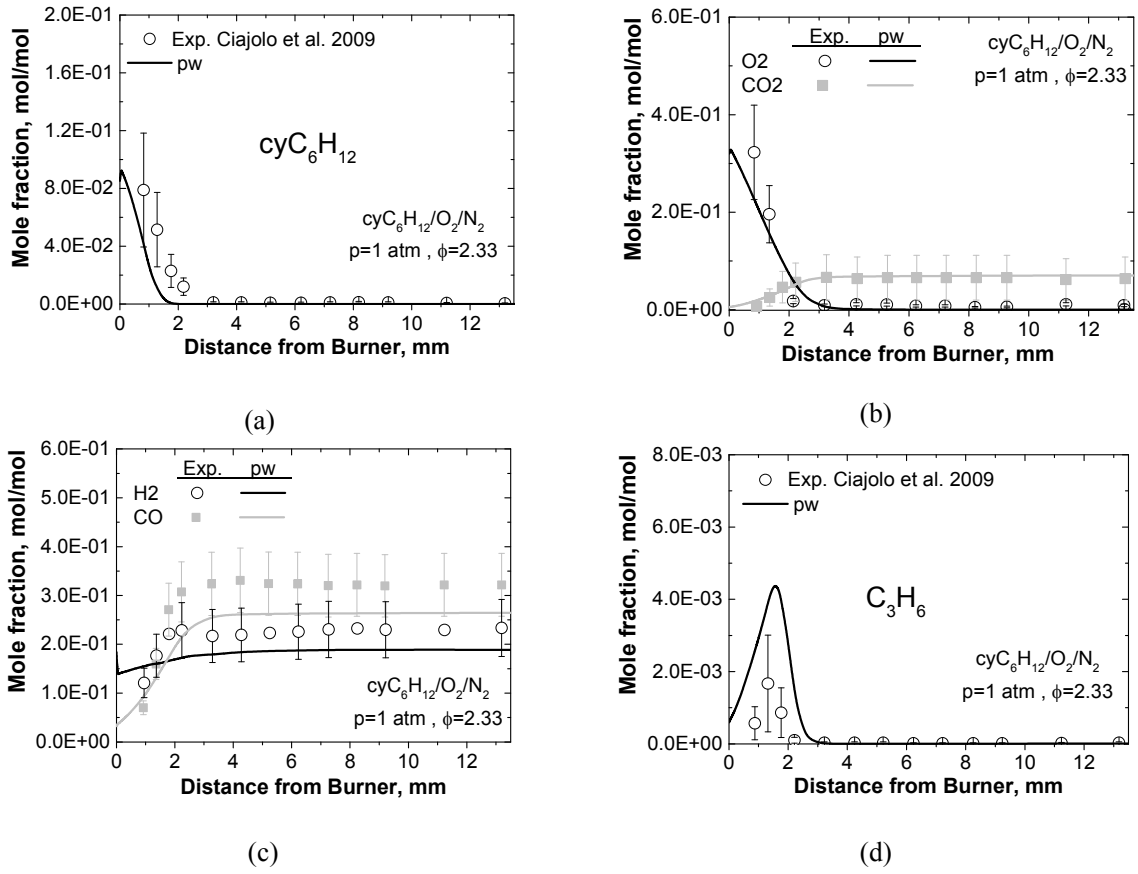

Figure S4 – Concentration profiles of species measured in burned stabilized flame of [20] and the simulation results [pw]

Supplementary Materials 2

Empirical rules for estimation of kinetic parameters of bi-molecular reactions:

The activation energy of a bi-molecular reaction can be approximated using the Polanyi-Semenov equations:

$$E_a = 48.1 - 0.25|\Delta H^0| \quad exothermic\ reactions \quad \text{Eq.(S1)}$$

$$E_a = 48.1 + 0.75|\Delta H^0| \quad endothermic\ reactions$$

where ΔH^0 is standard enthalpy of reaction. For reactions with two radicals as reactants, where the Polanyi-Semenov [1] equation results in negative values, the activation energy was assumed to be zero.

The pre-exponential factors were estimated based on the collision theory [2] using the numerical algorithm proposed in Cherny et al. [3].

Uncertainty analysis of the model rate parameters

Uncertainty of reaction model caused by mainly uncertainty of the chemical kinetics data (reaction rate coefficients, thermodynamic data, transport coefficients data, etc.) and experimental data which will be used for validation and optimization. In the case of the kinetic data, it is not simple to realize using of accurate first principle calculations for each reaction encountered in the kinetical model. The uncertainties for the published reaction rates are often not available or rarely reported [4]. The optimisation of kinetic model follows the reduction of model uncertainty. This could be achieved via minimizing the feasible area of parameters of reaction rate rule, in Arrhenius equation. The error margin for each reaction $\Delta k(T)$ included in the model is determined through the standard deviations of the rate coefficients A, n, E_a. The uncertainty factor $f(T)$ identifies the level of uncertainty of reactions. For lower and upper error boundaries, it will be defined as below [4]:

$$f_u(T) = log\frac{k_{upper}(T)}{k_0(T)}\ ,\ f_l(T) = log\frac{k(T)}{k_{low}(T)} \quad \text{Eq.(S2)}$$

where k_0 is the optimised rate value, known as nominal rate, k_{low} and k_{upper} are lower and upper rate boundaries. However, the statistical assessment of the rate is limited due to number of available data. If adequate sets of data are in access, the simple analysis of k uncertainty can be performed based on the least-squares regression. In this work the non-linear least squares method and its numeric realisation FUMILI [5]. It linearizes model $f(\vec{y},\vec{x})$ and approximates the goal function with modified parameters, which fits the data of m observations with a model of n unknown parameters ($m > n$).

The evaluation of parameters can be obtained through minimisation of objective function $\Phi(\vec{y},\vec{x})$ and linearization by a first-order Taylor series expansion about parameters:

$$\Phi(\vec{y},\vec{x}) = \sum_{j=1}^{m} \omega_j \left[Y_j^{exp} - \left(f_0(\vec{y},\vec{x}^*) + \sum_{k=1}^{n} \frac{\partial f_j(\vec{y},\vec{x})}{\partial x_k} \Delta x_k \right) \right]^2 \quad \text{Eq.(S3)}$$

The $\vec{y}$ is the vector of "coordinates", describing a physical property, such as temperature, pressure, etc. ; $\vec{x}$ is the vector of parameters to be modified, i.e. Arrhenius parameters A, n, and E_a in this case; ω_j is the weight of each set of observation, which directly correlates with experimental uncertainty and the Y_j^{exp} represents experimental set of data. Various sets of rate coefficients including experimental data, or literature data, by quantum chemistry or reaction models are assumed as statistical samplings (Y_j^{exp}). The weight coefficients are normally taken as claimed by the available literature sources. Otherwise an initial error equal to 50% will be prescribed to rate coefficients, which could be reduced or increased depending on the treatment process circumstances [4].

The vector of the parameter corrections Δx_k is obtained from n (from 1 to n_0) differential equations (for each parameter) following from minimisation of $\Phi(\vec{y},\vec{x})$:

$$\sum_{n=1}^{n_0} \left[\sum_{j=1}^{m} \omega_j \left(Y_j^{exp} - f_0(\vec{y},\vec{x}^*) \right) \frac{\partial f_j(\vec{y},\vec{x})}{\partial x_n} = \sum_{j=1}^{m} \omega_j \sum_{k=1}^{n} \frac{\partial f_j}{\partial x_k} \frac{\partial f_j}{\partial x_n} \Delta x_k \right] \quad \text{Eq.(S4)}$$

If we assign the derivative on the right side of the equation as $\Upsilon_{\alpha\beta}$, and on the left side of the equation as Ψ_{α}, as it comes in following (α,β: *1,..,*n_0):

$$\Upsilon_{\alpha\beta} = \sum_{j=1}^{m} \omega_j \frac{\partial f_j}{\partial x_\alpha}\frac{\partial f_j}{\partial x_\beta} \quad ,$$

$$\Psi_{\alpha} = \sum_{j=1}^{m} \omega_j \left(Y_j^{exp} - f_0(\vec{y},\vec{x}^*)\right)\frac{\partial f_j(\vec{y},\vec{x})}{\partial x_\alpha} \quad \text{Eq.(S5)}$$

Therefore, the vector Δx_k can be concluded as following:

$$\Delta x_k = \sum_{i=1}^{n} (\Upsilon^{-1})_{ki}\Psi_i \quad \text{Eq.(S6)}$$

The Υ^{-1} term is assigned as error (co-variance) matrix. This gives us information about parameters such as errors $s(x)$, and deviations of calculated functions (mean values of coefficients k_0), $\Delta f(\vec{y},\vec{x})$. These two are defined as following:

$$s(x_\alpha) = \left[\frac{v\varphi}{m-n} D(x_\alpha)\right]^{1/2},$$

$$f = t_s \left[\frac{\varphi}{m-n}\sum_{\alpha=1}^{n}\ \sum_{\beta=1}^{n}\left(\frac{\partial f}{\partial x_\alpha}\right)\left(\frac{\partial f}{\partial x_\beta}\right) cov(x_\alpha, x_\beta)\right]^{1/2}$$

Eq.(S7)

where φ is the sum of reduced deviations squares; $cov(x_\alpha, x_\beta)$ are the elements of the co-variance matrix $\Lambda\, D(x_\alpha) = \Lambda(x_{\alpha\alpha})$;the term $\left[\frac{\varphi}{m-n}\right]^{1/2}$ estimates the reduced standard deviation for the observations (experimental data); t_s is the coefficient of proportionality for $\Delta f/s(f)$ with a certain confidence probability [4].

The obtained Arrhenius parameters give the mean (nominal) values of the rate constant k_0. Therefore, with the approximated values of the errors vector $s(x_\alpha)$ from Eq.(S7), and the uncertainty degree of rate coefficient parameters, the lower and upper rate boundaries can be described as following:

$$k_{low}(T) = (A - s(A))T^{(n-s(n))}exp(-(E_a + s(E_a))/T)$$

Eq.(S8)

$$k_{upper}(T) = (A + s(A))T^{(n+s(n))}exp(-(E_a - s(E_a))/T)$$

The overall coefficients which characterize correlation of one parameter with others can be obtained via the co-variance matrix Λ as:

$$Q_\alpha = (1 - 1/R_\alpha)^{1/2},\ R_\alpha = \Lambda(x_{\alpha\alpha})\cdot\Lambda(x_{\alpha\alpha})^{-1} \quad \text{Eq.(S9)}$$

Also the pair correlation which characterizes the connection of parameters with each other is defined as below:

$$q_{\alpha\beta} = \frac{\Lambda(x_{\alpha\beta})}{(\Lambda(x_{\alpha\alpha})\cdot\Lambda(x_{\beta\beta}))^{1/2}} \quad \text{Eq.(S10)}$$

Table S3 – Reaction rate and estimated lower and upper uncertainty factors for modified reactions

Reaction*	ΔT, K	Initial rate [6]			Ref.	Modified rate			Ref.	f_l and f_u
		A	β	E_a		A	β	E_a		
$cyC_6H_{12} + O \leftrightarrows cyC_6H_{11} + OH$	500-3000	2.60E+06	2.0	2553	[7]	4.34E+09	1.33	3427.5	generic [a]	4.07-4.25
$cyC_6H_{11}+O_2 \leftrightarrows cyC_6H_{10}+HO_2$	700-3000	1.50E+12	0.0	4251.2	[8]	1.17E+13	0.0	7479.7	EM [b]	1.68-1.77
$cyC_6H_{10} + H \leftrightarrows cyC_6H_9 + H_2$	500-3000	3.97E+13	0.0	6562	EM	6.00E+12	0.0	4445	[9]	2.25-2.56
$cyC_6H_{10}+HO_2 \leftrightarrows cyC_6H_9+H_2O_2$	600-3000	1.14E+13	0.0	10709.5	EM	4.49E+10	0.6	15828	generic	2.39-2.61
$cyC_6H_{11}OO \leftrightarrows cyC_6H_{10}OOH$	800-3000	1.50E+12	0.0	24076	[10] [c]	2.00E+12	0.0	24045	[11] [d]	3.34-3.82
$cyC_6H_{10}OOH \leftrightarrows OH+cyC_6H_{10}Oa$	700-3000	1.00E+12	0.0	10400	[12]	9.31E+09	0.6	8437.08	generic	2.84-3.14
$cyC_6H_{10}OOH \leftrightarrows OH+cyC_6H_{10}Ob$	600-3000	1.50E+12	0.0	23400	[12]	1.25E+10	0.8	21662.2	generic	3.51-3.86
$cyC_6H_{10}OOH \leftrightarrows OH+cyC_6H_{10}Oc$	800-3000	1.90E+12	0.0	20700	[12]	1.08E+12	0.6	23692.3	generic	2.78-2.97

Notes: * Reaction rate constants in cm^3, mol, cal units, $k = AT^{\beta}exp(E/RT)$
a) Estimated average rate coefficients by uncertainty analysis (REAC-UQ) **b)** Estimated using the empirical method [1-3]
c) Analogous with C_8 **d)** The factor A multiplied by 2/3

1. Y. M. Zhorov, Thermodynamics of Chemical Processes; Petrochemical synthesis, processing of petroleum, coal, and natural gas, 1st Edition, Moscow, Russia: Mir Publications, 1987.

2. M. Trautz and Z. Anorg, "Evaluation of Arrhenius Frequency Factor (A) by Simple Collision Theory," Chemistry, vol. 1, 1916.

3. G. Chernyi, S. Losev, S. Macheret and B. Potapkin, Physical and Chemical Processes in Gas Dynamics : Cross Sections and Rate Constants: American Institute of Aeronautics & Astronautics, 20 Jun 2002., Reston, United States: AIAA, 2012.

4. Slavinskaya, N.A.; Chernov, V.; Whitside, R.;Starke, J.H.; Mirzayeva, A.; Abassi, M.; Auyelkhankyzy, M., „A modeling study of acetylene oxidation and pyrolisys," Combustion and Flame, submitted.

5. V. Kurbatov und I. Silin, *Nuclear Instruments and Methods in Physics Reserach A,* Bd. 345, pp. 346-350, 1994.

6. M. Abbasi, N. A. Slavinskaya and U. Riedel, "Kinetic Modeling of Cyclohexane Oxidation Including PAH Formation," Grapevine, Texas, USA, 2017.

7. A. Ristori, P. Dagaut, A. El Bakali and M. Cathonnet, "The Oxidation of N-Propylcyclohexane: Experimental Results and Kinetic Modeling," *Combustion Science and Technology,* pp. 197-228, 2001.

8. H. R. Zhang, L. Huynh, N. Kungwan, Z. Yang and S. Zhang, "Combustion Modeling and Kinetic Rate Calculations for a Stoichiometric Cyclohexane Flame.1. Major Reaction Pathways," *J. Phys. Chem. A,* pp. 4102-4115, 2007.

9. D. Voisin, A. Marchal, M. Reuillon and J.-C. Boettner, "Experimental and Kinetic Modeling Study of Cyclohexane Oxidation in a JSR at High Pressure," *Combustion Science and Technology,* vol. 138, pp. 137-158, 1998.

10. H. Curran, P. Gaffuri, W. Pitz and C. Westbrook, "A Comprehensive Modeling Study of iso-Octane Oxidation," *Combustion and Flame,* pp. 253-280, 2002.

11. Granata, S., Faravelli, T., Ranzi, E., "A wide range kinetic modeling study of the pyrolysis and combustion of naphthenes," Combustion and Flame, Vol. 132, 2003, pp. 533-544.

12. Silke, E. J., Pitz, W. J., Westbrook, C. K., Ribaucour, M., "Detailed Chemical Kinetic Modeling of Cyclohexane Oxidation," J. Phys. Chem. A, Vol. 111, 2007, pp. 3761-3775..

IRSTI 29.27.03; 29.15.19.

Fission fragments and primary electrons' energy distribution in helium-3 plasma irradiated by neutron flux

S.K.Kunakov[1, *] and A. Shapiyeva[2]

[1]*Al Farabi Kazakh National University, 71, al-Farabi Ave., 050040, Almaty, Kazakhstan*
[2]*Moscow Institute of Physics and Technology, 9 Institutskiy per., Dolgoprudny, Moscow Region, 141701, Russia*
**e-mail: Sandybek.Kunakov@kaznu.kz*

Boltzmann kinetic equations governing energy spectra distribution of fast particles in nuclear induced plasma are defined and presented for continuous fissionable plasma interacting with neutrons.
The formation of electrons energy distribution crucially depends on energy distribution of fission fragments and cannot be treated separately and their distributions self consistently affect on electrons energy spectra time evolution and their degradation in space. So the self-consistent system of Boltzmann kinetic equations for both electrons and fission fragments are proposed and discussed for helium-3 plasma. Primary electrons spectra analytical expressions are derived and the first order approximation presented on the assumption that energy spectra of protons and tritium nuclei have monochromatic energy spectra created by helium-3 fissioning in neutron flux. Any gas irradiated by highly energetic particles demonstrates its modified chemical abilities as well as a great variety of energy transformation channels including the selection of some definite chemical reactions leading to innovative transformation in technology [1-5]

Key words: fissioning plasma, Boltzmann equation, helium-3**.**

1. Introduction

Any gas irradiated by highly energetic particles demonstrates its modified chemical abilities as well as a great variety of energy transformation channels including the selection of some definite chemical reactions leading to innovative transformation in technology [1-5]. In some cases when the testing gas contains fissionable component interacting with neutrons like helium-3 or uranium-235 the plasma creates specific physical conditions owing to fission fragments and presents by itself a unique physical object, which in general makes it possible to realize direct transformation their nuclear energy into electromagnetic radiation. In [6] the kinetic Boltzmann equation governing electron energy distribution in plasmas generated by fission fragments is developed. It should be pointed out that the requirements to self-consistency of external electric field are taken into consideration and presented by means of am bipolar diffusion. Recombination processes are also partially included in system of kinetic equation governing electrons energy distribution and confined by boundary conditions [7].

Definition of highly energetic fission fragments energy distribution spectra including primary electrons is the key and not yet solved problem, which reveals how and in what way their transformation might be realized [6,7]. Well-known famous Boltzmann equation was applied to solution of a plenty of physical problems, and was used even in description of gravitational interactions, gravitational redshift and dilation. So, the profound meaning of Boltzmann equation reveals the problems and presents clear understanding of them not only in physics of non uniform gases but practically in all branches of physics and continues to penetrate its applications further on. Plasma generated by fission fragments also might be described by Boltzmann equation which certainly should be mathematically adjusted to that physical conditions for gaseous mixtures containing fissionable components and which set into the

neutron flux, like, for instance, ampulla with helium-3 gas tested in the center on nuclear reactor core.

Since the appearance of outstanding in its importance Theory of Non – Uniform Gases developed by S. Chapman and T. Cowling [8] sufficient number publications devoted to this problem were released. Most of them were focused to modify Boltzmann kinetic equation in different fields of applications. One of the most cited is [9] in which the high frequency gas discharges for slightly ionized plasma are studied within which the following limited conditions assumed. The densities of electrons, ions, and excited molecules are very small compared to the density of molecules of buffer gas, elastic collisions prevail over the inelastic ones, gas has the density when the hydrodynamic approach is reasonable and the frequencies of external electric field is higher the plasma frequencies. The major of [9] devoted to the development of methods for calculating the energy distributions in a gas of low ion density influenced by high frequency a. c. field. Taken assumption that initial and final velocities are very close to each other leads to sufficient number of limitations for definite applications. As it was noted in [10] incident electrons interact with field particles not in the way like rigid spheres, but act with a complex dynamical system of charged particles moving in the state of dynamical equilibrium and actually interact initially with cycling electrons moving on the upper orbits. How the primary electrons were originated also were not discussed and identified in [9]. Further detailed expansions of the function of energy distribution into the series and correspondent results are losing their applicability even in neighboring physical conditions. Electrons energy distribution at high values of external electric field in nitrogen gas from 100 Td up to 3000 Td obtained and discussed in [11] .The ionization coefficients, drift velocity and mean energies in steady state conditions are calculated using simplified secondary electron energy distribution taken from experiments. Rotational excitation and momentum transfer differential cross section for low energy electrons are obtained from mobility and diffusion coefficients by calculating electron energy distribution functions in hydrogen and nitrogen plasma by the authors in [12]. Here Boltzmann equation for electrons was regarded in the way like in [9] without any discussion of primary electrons spectra formation. Calculations of the steady state electron swarm parameters in rare gases and mixtures are reported in [13]. The presence of electron density gradient implies the external electric field to be self-consistent and secondary electrons spectra also is also the subject of Townsend ionization processes which should be initially included in Boltzmann kinetic equation, but not taken as a priori by analytical expression which should be taken into consideration in initial equations. Electrons beam impact nitrogen gas and further electrons degradation spectra taken in energy scale were also studied in [14, 15]. Green's function method was used to obtain ionization coefficients, which made possible to evaluate external electric field breakdown level [15, 16]. Only in [14] the source of ionization by electron beam, which was included reasonably and solved. In [17] the Townsend ionization coefficient and the electron drift velocity were calculated in the cold cathode discharge gap and are in good agreement with experimental data.

Following to [18] in fully ionized plasma in a sufficiently strong electric field so-called runaway electrons are created and the main part of them on the mean free path, receives more energy from the electric field than it loses in elastic and inelastic collisions, and the electrons are continuously should be accelerated. This was declared also in [19, 20] and steady state Boltzmann equation was taken in use without no information about how this processes (bremsstrahlung as a force of friction) were originated.

In weakly ionized plasma the formation of runaway electrons seems to be practically impossible due to very detailed analysis made in [21]. On the contrary the authors [19,21] are sure that for arbitrarily small values of the electric field strength the majority of electrons might be accelerated to the level of energy possible to ionize neutrals forming secondary electrons and the number of ionization events will exponentially rise as well as their average velocity and energy does not depend on the distance from cathode [19]. The equation for mean energy electrons balance is not sufficient to make such strong deductions about formation runaway electrons by some definite reasons. The force of friction also was taken as a key point in formation of run away electrons [19, 21] .It does not give clear answer because of the following reasons.

The identification of fast electrons with energy around Mev region (runaway electron) not discussed or presented as well as the fact that where the radiation (bremsstrahlung) starts and ends and how

the formation of X-rays should be included in kinetic equation. [19]. The X-rays [22,23] also might be treated like electrons (the de Broglie wave length) and the next coming question is that weather or not the absorption of X-ray by electrons leads to rise its kinetic energy lifting them to the MeV level where usually neutrino oscillations connected with presence the beta electrons are existing. [24]

2. Boltzmann equation for continuous plasma irradiated by fission fragments. General case

The system of Boltzmann kinetic equation to define the energy spectra of fission fragments and born as a result of this irradiation primary electrons energy distribution are as follows:

$$\begin{aligned}\partial_{\mu} ff_j = S_j^{ff}(n \to {}^{3}He \to {}_{235}UF_6 \to ff_j) + S_{ff_j}^{PE}(ff_j(\varepsilon') \to bg \to bg^{+} + PE + ff_j(\varepsilon'_{ff} - I - \varepsilon_{PE}) \\ -L_{ff_j}^{PE}(ff'_j(\varepsilon') \to bg \to bg^{+} + PE + ff'_j(\varepsilon'_{ff} - I - \varepsilon_{PE}) + \\ S_{ff_j}^{exc}(ff_j(\varepsilon') \to bg \to bg^{exc} + ff_j(\varepsilon'_{ff} - I^{exc}) - \\ -L_{ff_j}^{exc}(ff'_j(\varepsilon') \to bg \to bg^{exc} + ff'_j(\varepsilon'_{ff} - I^{exc}) + \\ +S_{ff_j}^{el}(ff_j(\varepsilon') + bg \to bg + ff_j(\varepsilon'_{ff} - \Delta E^{el}) - \\ -L_{ff_j}^{el}(ff'_j(\varepsilon') + bg \to bg + ff'_j(\varepsilon'_{ff} - \Delta E^{el}) - \\ -L_{ff_j}^{rec}(ff^{+}{}_j(\varepsilon') + e \to ff^{0}{}_j(\varepsilon'_{ff})\end{aligned} \tag{1}$$

In equation (1) the following notations are used:

Bg-buffer gas, PE-primary electrons, S, L-source and outflow of charged particles in definite phase volume.

For electrons the following coupling equations are to be used:

$$\begin{aligned}\partial_{\mu} f_e = S_{ff_j}^{PE}(ff_j(\varepsilon') \to bg \to bg^{+} + PE + ff_j(\varepsilon'_{ff} - I - \varepsilon_{PE}) \\ +S_{f_e}^{ion}(f'_e(\varepsilon') \to bg \to bg^{+} + e + f_e(\varepsilon'_{f_e} - I - \varepsilon_{se}) + \\ -L_{f_e}^{ion}(f_e(\varepsilon') \to bg \to bg^{+} + e + f_e(\varepsilon_{f_e} - I - \varepsilon_{se}) + \\ +S_{f_e}^{exc}(ff'_j(\varepsilon') \to bg \to bg^{exc} + ff_j(\varepsilon'_{f_e} - I^{exc}) - \\ -L_{f_e}^{exc}(ff'_j(\varepsilon') \to bg \to bg^{exc} + ff_j(\varepsilon'_{f_e} - I^{exc}) + \\ +S_{f_e}^{el}(ff'_j(\varepsilon') + bg \to bg + ff_j(\varepsilon'_{f_e} - \Delta E^{el}) - \\ -L_{f_e}^{el}(f_e(\varepsilon') + bg \to bg + f_e(\varepsilon_{f_e} - \Delta E^{el}) - \\ -L_{f_e}^{rec}(ff^{+}{}_j(\varepsilon') + e \to ff^{0}{}_j(\varepsilon'_{ff_j}) + e'\end{aligned} \tag{2}$$

where [25]:

$$S_{\mu}^{\nu} = \int_{I}^{E\max} \Omega(E_{ff}, \Delta E) g(V' \to V) f_{\mu}^{\nu}(t, r, E_{\mu}) d\Delta E \tag{3}$$

$$\Omega(E_{ff},\Delta E)=\frac{\sigma_0}{(\Delta E_{ff})^2}\frac{1}{E_{ff}}f_{bg}[\frac{I_{bg}}{E_{ff}}+\frac{4}{3}Ln(2.7+\frac{V_{ff}}{\overline{V_e}})]$$

$$f_{bg}=[\frac{\overline{V_e}}{V_{ff}}]^2$$

Due to the experimental measurements [4-5] we take ^{3}He isotope gas in thermal neutral flux and the value of fission fragments energy in its first approximation equal to the delta function from its initial energy is $E0$:

$$f_{pe}(V_i)=6.56*10^{-14}[BG]\sum_{k=1}^{N}Z_{j,k}^2\int_{I}^{E_{j,k}^0}dV_{j,k}*\delta(V_{j,k}-\frac{1}{2}V_{j,k}^0)*$$

$$\frac{8}{m_{j,k}m_e^2V_i^4V_{j,k}^2}\left\{\frac{\sqrt{\frac{2I_{bg}}{m_e}}}{V_{j,k}}\right\}^{22}*[1+\frac{4}{3}Ln(2.7+\frac{E_{j,k}}{I_{bg}})] \quad (4)$$

3. Conclusion

Boltzmann kinetic equations governing energy spectra of fast particles in nuclear induced plasma are defined as a coupled system of fission fragments and electrons which should be treated as self-consistent system and presents sensible approach to detailed description of fissionable plasma interacting with neutrons. This type of Boltzmann kinetic equations system applied and discussed for helium-3 plasma. Major part of primary electrons spectra analytical expressions derived on the assumption that helium-3 isotope fission products have monochromatic energy spectra.

In weakly ionized plasma the formation of runaway electrons seems to be practically impossible due to very detailed analysis made in [26, 27]. On the contrary the authors [19, 21] are sure that for arbitrarily small values of the electric field strength the majority of electrons might be accelerated to the level of energy possible to ionize neutrals forming secondary electrons and the number of ionization events will exponentially rise as well as their average velocity and energy does not depend on the distance from cathode [19]. The equation for mean energy electrons balance is not sufficient to make such strong deductions about formation runaway electrons by some definite reasons. The force of friction also was taken as a key point in formation of run away electrons [19, 21]. It does not give clear answer because of the following reasons.

The identification of fast electrons with energy around Mev region (runaway electron) not discussed or presented as well as the fact that where the radiation (bremsstrahlung) starts and ends and how the formation of X-rays should be included in kinetic equation. [19]. The X-rays [21, 22] also might be treated like electrons (the de Broglie wave length) and the next coming question is that weather or not the absorption of X-ray by electrons leads to rise its kinetic energy lifting them to the MeV level where usually neutrino oscillations connected with presence the beta electrons are existing [24, 26].

References

1 J.C. Guyot, G.H. Miley, J.T. Verdeyen and T.Ganley On Gas Laser Pumping via nuclear Radiations, Symp.research on Uranium Plasmas and Their Technological applications, NASA SP-236, p. 357, National Aeronautics and Space Administration, Washington (1970)

2 G.H. Miley, J.T. Verdeyen, T. Ganley, J. Guyot, P. Thiess. Pumping and Enhancement of Gas Lasers via Ion Beams, Symp. Electron, Ion, and Laser Beam Technologies, University of Colorado, p. 299, San Francisco Press (1971)

3 I. Tomizo, M. Toshimitsu. Monte Carlo calculations of motion of electrons in Helium // Journal of the Physical Society of Japan. – 1960. – Vol.15. – No.9. – P. 1675–1680

4 J.C. Guyot, G.H. Miley, J.T. Verdeyen. Application of a two –region heavy charged particle model to noble-gas plasmas induced by nuclear radiations // Nuclear Science and Engineering. -1972. – Vol. 48. – P. 373-386.

5 S.W. Benjamin, H.M. George. Monte Carlo simulations of radiation–induced plasmas // Nuclear Science and Engineering. – 1973. – Vol.52. – P.130–141.

6 H.A. Hassan, J. E. Deese. Electron distribution function in a plasma generated by fission fragments // The Physics of Fluids. – 1976. – Vol.19. – No.12. – P. 2005-2011.

7 J. E. Deese, H.A. Hassan. Distribution functions in a plasma generated by a volume source of fission fragments // The Physics of Fluids. -1979. – Vol. 22(2). – P.257-262.

8 S. Chapman, T. Cowling. The mathematical theory of non-uniform gases, Cambridge, 1952.

9 T. Holstein. Energy distribution of electrons in high frequency gas discharges // Physical Review. – 1946. – Vol.70. – No.5-6. – P. 367-384.

10 M. Gryzinski. Classical theory of atomic collisions. I. Theory of inelastic collisions // Physical Review. – 1965. – Vol. 138. – No. 2A. – P. A336-A358.

11 S. Yoshida, A.V. Phelps, L.C. Pitchford. Effect of electrons produced by ionization on calculated electron energy distribution // Physical Review. A. – 1983. – Vol.27. – P. 2858-2867.

12 L.S. Frost, A.V. Phelps. Rotational excitation and momentum transfer cross sections for electrons in H_2 and N_2 from transport coefficients // Physical Review. – 1962. – Vol.127. – P.1621-1633.

13 R. Lagushenko, J. Maya. Electron swam parameters in rare gases and mixtures // J.Appl.Phys. – 1984. – Vol. 55 (9). – P. 3293-3299.

14 V.P. Konovalov, E.E. Son. Function of energy distribution of electrons in rare gases Chemistry of plasma. Issue 14. Moscow: Energoatomizdat. 1987, 194 p. (In Russian)

15 V.P. Konovalov, E.E. Son. Transport properties of weakly ionized plasma in rare gases // JTF. – 1980, Vol. 50, - No. 2. – P. 300-310(in Russian)

16 D.R. Suhre, J.T. Verdeyen. Energy distribution of electrons in electron-beam-produced nitrogen plasmas // Journal of Applied Physics. -1976. – Vol.47. – No.10. – P. 4484-4488.

17 H. Dreiser. Electron and ion runaway in a fully ionized gas, part I //Phys. Rev. – 1959. – Vol.115. – P. 238-249.

18 R.A. Roussel-Dupre, A.V. Gurevich, T. Tunnell, G.M. Milikh. Kinetic theory of runaway air breakdown // Physical Review E. – 1994. – Vol.49. – No.3. – P. 123-127

19 A.N. Tkachev, S.I. Yakovlenko. On the mechanism of electron runaway in a gas. The upper branch of the ignition curve of self-discharge for helium, xenon and nitrogen // Letters to JETP. – 2003. – Vol.77. – No.5. – P. 264-269. (in Russian)

20 L.P. Babich. Analysis of a new mechanism for the runaway of electrons achieved in discharges in dense gases // UFN. – 2005. – Vol. 175. – No. 10. – P. 1069-1091. (in Russian)

21 A.V. Gurevich, K.P. Zybin. Runaway breakdown and the mysteries of lightning // Physics Today. – 2005. – P.37-43. – Vol. 7.

22 W.A. Macky. Some investigations on the deformation and breaking of water drops in strong electric fields // Proc.Roy.Soc.A. – Vol.133. – P. 17-21. 2011.

23 L.B. Loeb. The mechanisms of stepped and dart leaders in cloud-to-ground lightning strokes // Geophysical Research. – 1966. – Vol. 71. – No.20. – P. 4711-4721.

24 A.A. Belevtsev. Development of electron impact excitation and ionization in noble gases and liquids in strong electric fields // High Temperature. – 2017. – Vol.6. – P. 1-9.

25 S. Kunakov, E. Son, Zh. Bolatov, N. Kaster. Optical spectra in helium plasma generated by nuclear fission fragments // International Journal of Mathematics and Physics. – 2015. – Vol. 6. – No.1. – P. 75-81.

26 S. Kunakov, E. Son, A. Shapiyeva. Probe diagnostics of $^3He+UF_6$ plasma, generated in the core of nuclear reactor WWW-K // International Journal of Mathematics and Physics. – 2015. – No.1. – P. 69-74

IRSTI 27.35.51

Alkali ions mobility in parent vapor

R.I. Golyatina[1], S.A. Maiorov[1,2,*] and G.B. Raghimkhanov[3]

[1]*Prokhorov General Physics Institute of RAS, Moscow, Russia*
[2]*Joint Institute for High Temperatures, Russian Academy of Sciences, Moscow, Russia*
[3]*Dagestan State University, Makhachkala, Russia*
[*] *e-mail: mayorov_sa@mail.ru*

Certain approximations of mobility coefficients for the metal atoms' ions in parent vapor are investigated, a comparison between experimental data was drawn, and Monte Carlo calculations are performed. In contrast to ions of noble gases, ions and atoms of alkali metals have a number of features that must be considered when building a model of ion-atom collisions. Approximations for mobility coefficients for the alkali ions in parent vapor are given, they are valid not only in the weak electric field limit, but also in strong fields, when ion heating enacts in external electric field. On the basis of the analysis of Monte Carlo calculations and comparing them with experimental data on the mobility of alkali metal ions in noble gases, we obtain approximation formulas for the mobility of alkali metal ions in parent vapors. The parameters found earlier for the approximation of the drift velocity of ions of noble gases are also given as a reference material. The parameters obtained in this work for the approximation of the mobility of alkali metal ions in parent vapors can be used to estimate the characteristics of a gas-discharge plasma.

Key words: gas discharge, ion mobility, alkali atom, Monte Carlo, ion-atom collision, discharge plasma.
PACS numbers: 52.27.Cm, 52.80.Tn.

1. Introduction

At present experimental and theoretical data on kinetic coefficients were obtained mainly 30-50 years ago. That time was the period when gas discharge plasma was very popular, as there were some technological problems in microelectronics, medicinal applications, surface treatment issues, tasks of obtaining plasma light sources, etc. The detailed review of the vast amount of experimental and theoretical results is given in a number of books and reviews [1-5].

Modern technologies often use plasma processes, in which there are metal vapors in the core. They fall into the gas discharge zone or due to the spraying of the structural elements of the gas-discharge chamber, or they are intentionally introduced.

Often the presence of impurities arising, which appeared, for example, due to sputtering of the cathode as a result of ion bombardment, is not taken into consideration while analyzing the results of the experiments. It is well-known that sometimes even very small impurities (ppm) can fundamentally change the discharge characteristics [6-11].

It is necessary to know the kinetic coefficients – mobility, diffusion, viscosity, etc. for the qualitative estimation, for modeling the processes in gas discharge plasma on the basis of multifluid gas flue models. This article is devoted to closing the gap in the part of the alkali ions mobility coefficient characteristics in parent vapor, as the available data are sketchy and differ greatly.

2. Ion mobility in a weak electric field

Let's describe different drift velocity approximations for the case of small field gradients, when the drift velocity is much smaller than the thermal atom velocity and therefore the anisotropy of the ion velocity distribution function can be neglected. A detailed and thorough review of the available experimental and computation data along with different approximations is given in the book [1] and review [2 – 5]. The ion drift velocity in the gas under the influence of constant and uniform electric field is determined by the expression.

$$u = KE, \quad (1)$$

where K – ion mobility coefficient, E – electric field strength. The mobility coefficient in this equation is a function of the density and temperature of the atoms, as well as the field strength.

In the case of small fields, the temperature of the atoms determines the average collision energy and the dominant type of collisions. Consequently, it is the temperature that determines the values of the coefficients of mobility and diffusion of ions in the limit of a weak field. Measurement of the dependence of the mobility of ions on the gas temperature allows us to determine the potential of the interaction of an ion with an atom [1, 12].

When an ion collides with an atom of its own gas, there is a probability of electron transition from atom to ion without changing the internal energy of the colliding particles. Such a process is called resonant charge exchange and usually refers to inelastic collisions, since it has a quantum mechanical nature [1, 12]. Collisions with resonant charge transfer dominate at not very low temperatures .

Then, the solution of the Boltzmann kinetic equation at low electric field strengths in the first approximation of the Chapman – Enskog leads to the following expression for the mobility of ions in its own gas [12]:

$$K_0 = \frac{3\sqrt{\pi}e}{16(m_i T)^{1/2}\sigma_{res}(3v_T)N_0} = \frac{1.342\times10^4}{\sqrt{m_i T}\sigma_{res}}\frac{cm^2}{V\cdot s}. \quad (2)$$

Here K_0 _ mobility at standard gas density $N_0 = 2.686763\times10^{19}$ atoms in cm^3, m_i expressed in proton mass units, atom temperature T – in Kelvin degrees, and the cross section for resonant charge exchange $\sigma_{рез}$ – in 10^{-16} cm^{-2}, thermal velocity of atoms $v_T = \sqrt{T/m_i}$. The numerical factor in the formula (2) $C_{C-E}^{(1)} = 3\sqrt{\pi}/16 \approx 0.332$ corresponds to the first approximation of Chapman – Enskog, in the second order approximation for it is obtained close value $C_{C-E}^{(2)} = 31\sqrt{\pi}/168 \approx 0.327$ which indicates the rapid convergence of the expansion of the distribution function in a series of polynomials.

The probability of electron transfer from atom to ion (charge exchange) drops exponentially sharply with increasing distance between particles. Therefore, with good accuracy, we can assume that after the passage with the distance of the closest approach $r_{\min} > R_0$ the probability of electron transfer is negligible small, where the magnitude R_0 determines the reaction threshold. If an ion approaches an atom close enough, so that $r_{\min} < R_0$ then the electron orbits of the atom and ion overlap. In this case, the electron during the collision will make many transitions from atom to ion and after the collision will remain with equal probability in one of the colliding particles. The charge exchange cross section in this approximation is determined by the relation:

$$\sigma_{res} = \frac{1}{2}\pi R_0^2. \quad (3)$$

As shown by theoretical and experimental data, the resonance charge exchange cross section logarithmically weakly depends on the relative velocity *v12* of the colliding particles and can be approximated by the following relationship:

$$\sigma_{res}(\varepsilon_{12}) = \pi a^2 \ln^2(U_0/\varepsilon_{12}) = \\ = \sigma_{res}(\varepsilon_0)[1 + a\ln(\varepsilon_0/\varepsilon_{12})]^2, \quad (4)$$

or

$$\sigma_{res}(\varepsilon_{12}) = \sigma_{res}(\varepsilon_0) + B\ln(\varepsilon_0/\varepsilon), \quad (5)$$

where $U_0, a, B, \sigma_{res}(\varepsilon_0)$ – positive approximation constants [1, 12]. At collision energies $\varepsilon_{12} = m\,\mathrm{v}_{12}^2/2 < Ry$ cross section $\sigma_{res}(\varepsilon_{12})$ usually several times greater than the gas kinetic cross section (m is the mass of an ion, for the case of collisions in its own gas, equal to the mass of the atom).

At not very low collision energies, the cross section for resonant charge exchange weakly depends on the collision energy (relative velocity of the colliding particles); therefore, in derivaton (2), it was assumed that the mean free path does not depend on the collision energy. Due to the polarization of the atom in the ion field, an attraction arises between them. The diffusion cross section for scattering caused by the scattering of

ions due to the polarization of the atom in the ion field is [1, 12]:

$$\sigma = 1.105\sigma_{cupture} = 2.21\pi\sqrt{\alpha_d e^2 / \mu v^2}\ . \quad (6)$$

Here $\sigma_{cupture} = 2\pi\sqrt{\alpha_d e^2 / \mu v^2}$ – is the capture cross section on the spiral orbit in the polarization potential. Accordingly, the mobility of ions in the polarization limit is determined by the well-known expression [1, 2]:

$$K_{pol} = 13.853\left(\alpha_d \mu\right)^{-1/2}, \quad (7)$$

where α_d – polarizability in cubic angstroms, μ – reduced mass in grams per mole.

To take into account the polarization interaction, the first Chapman – Enskog approximation for mobility in the absence of elastic scattering was corrected in [12] and the following expression was obtained:

$$K_0 = \frac{0.217e}{(m_i T)^{1/2}[R_0^2(3v_T) + \alpha_d e^2 / 4TR_0^2(\sqrt{6T / m_i})]N_0}, \quad (8)$$

The mobility of ions in their own gas, calculated by the formula (8), in the limit of low temperatures, does not differ much from the exact result. Having corrected formula (8) so that in the limit of low temperatures it gives an exact result, the following expression for mobility was obtained in [12]:

$$K_0 = \frac{0.217e}{(m_i T)^{1/2}[R_0^2(3v_T) + \alpha_d e^2 / 4TR_0^2(\sqrt{6T / m_i}) + 0.16\sqrt{\alpha_d e^2 / T}]N_0}\ . \quad (9)$$

3. Ion mobility in a strong fields

When ion drift in a strong field, the drift velocity becomes comparable or even greater than the thermal velocity of the atoms; therefore, the anisotropy of the ion distribution function in velocities cannot be neglected. Note that the criterion of a strong field depends not only on the electric field strength, but also on the gas temperature. Generally speaking, at any field strength, the gas can be of such a temperature that the thermal velocity of the atoms will be less than the drift velocity.Therefore, in cryogenic discharges, even at field strengths of the order of 2 V / cm, which are typical for a gas discharge under reduced pressure, the field can be considered as a strong [13, 14].

Numerous experimental data show that the drift velocity of ions in their own gas is well described by the semi-empirical Frost formula [15], which takes into account the dependence of the drift velocity on the field strength:

$$u = a\left(1 + bE\right)^{-1/2} E\ . \quad (10)$$

This approximation for dependence of the drift velocity on the electric field has two parameters: *a*– mobility in the weak field limit, and $b = 1 / E_{heating}$. Magnitude $E_{heating}$ - this is the value of the electric field strength, in which, due to the heating of the ions, the mobility according to the Frost formula decreases by a factor of two. Both of these parameters depend only on the atomic temperature and density, but do not depend on the electric field intensity.

Let us rewrite Frost's formula (10) as a dependence of the drift velocity on the reduced electric field strength:

$$u = K_0 N_0 \left(1 + (E / N) / (E / N)_{heating}\right)^{-1/2} (E / N). \quad (11)$$

Here are two parameters $(E / N)_{heating}$ and K_0 depend only on temperature: $(E / N)_{heating}$ – is the value of the reduced electric field strength, at which, due to the heating of the ions, the mobility according to the Frost formula decreases by a factor of two.

4. Approximation of mobility in a weak fields

In the literature, the values of ion mobility K_0 are mainly given at room temperature 291~300K. There is also an insignificant amount of experimental data on the characteristics of the drift of helium and neon ions at cryogenic temperatures near the 77 K and 4.2 K points [3 – 5].

Experimental data on the mobility of lithium, sodium, and cesium ions in helium in the atomic temperature range from 20 to 500 K are given in review [4], and data on the mobility of alkali metal ions in inert gases at room temperature are given in book [12]. Experimental data on the mobility of alkali ions in their own vapors for potassium at room temperature and rubidium, cesium at atom temperatures from 620 to 660 K are given in book [12].

In [9], based on the analysis of Monte Carlo calculations of the kinetic characteristics of ion drift in its own gas for all noble gases, an approximation was chosen for the dependence of mobility in a weak field on the gas temperature:

$$K_0 = K_{pol} / \left(1 + T / \varepsilon_0\right)^{1/2}. \qquad (10)$$

Here $K_{pol} \equiv K_0(0)$ is the value of polarization mobility at the standard gas density in the limits of weak field and low temperature. Fitting parameter ε_0 in (10) has the meaning of the characteristic collision energy, upon reaching which the polarization interaction no longer makes the main contribution to the collision frequency and elastic collisions and resonant charge transfer begin to play the role. Table 1 shows the approximation parameters (10) for all noble gases, found in [9]. Parameter $(E/N)_0$, given in this table has the meaning of the upper limit of the electric field strength, at which the effects of a strong field begin to play a role. This parameter is used in constructing an approximation of the dependence of mobility on field strength.

Table 1 – The value of the approximation parameters for the mobility of ions of noble gases in its own gas.

System	K_{pol} см^2/с В	ε_0, *K*	$(E/N)_0$, *Td*
He^+ in He	21.6	90	16
Ne^+ in Ne	6.8	210	34
Ar^+ in Ar	2.42	240	73
Kr^+ in Kr	1.36	330	106
Xe^+ in Xe	0.85	270	122
Hg^+ in Hg	0.61	58	63

In contrast to ions of noble gases, ions and atoms of alkali metals have a number of features that must be considered when building a model of ion-atom collisions. The polarizability of ions of noble gases is not very different from the polarizability of atoms with the exception of the hydrogen-like helium ion. Since polarizability is directly related to some effective atomic radius, it was assumed during the play of ion-atomic collisions of inert gases that the gas-kinetic radius of an ion (hard sphere) is equal to the atomic radius. But for alkali ions, the situation is completely different. The outer electron shell of a single-ionized alkali metal atom is similar to the outer electron shell of the corresponding inert gas atom. But it is in a stronger field than the shell of an inert atom, so its effective size will be smaller. Measurements show that the polarizability of an alkali metal ion is about one and a half to two times less than the polarizability of the atom of the corresponding inert gas, therefore it is quite logical to assume that the radius of the ion of the alkali atom is equal to the radius of the corresponding atom of the noble gas (lithium ion radius is equal to radius of a helium atom, sodium ion radius is equal to radius of neon atom, etc.)

Table 2 – Polarizability of noble gases, alkali and metals and their ions, where α_d – polarizability in cubic angstroms [1]

	α_d		α_d		α_d		α_d
He	0.205	He^+	0.0417	Li	24.0	Li^+	0.0285
Ne	0.395	Ne^+	0.21	Na	24.2	Na^+	0.280
Ar	1.64			K	41.3	K^+	1.09
Kr	2.48			Rb	43.6	Rb^+	1.81
Xe	4.04			Cs	53.0	Cs^+	2.73

There are very few experimental data on the mobility of alkali metal ions in their own vapors, but there is a lot of data on their mobility in the weak field limit in inert gases. In the book [12], experimental data on the mobility of alkali metal ions in inert gases at room temperature are given. In Tab. 3, these data are compared with the calculations performed in this work.

Table 3 – The ratio of the mobility of alkali metal ions in inert gases at room temperature to the polarization mobility calculated by the formula (7). The experimental data is the *exp* line, italicized and bold, the Monte Carlo calculations are the *MC* line.

Ion		*He*	*Ne*	*Ar*	*Kr*	*Xe*
Li^+	*exp*	*1.27*	*1.17*	*1.06*	*1.07*	*1.06*
	MC	*1.05*	*1.06*	*1.05*	*1.08*	*1.07*
Na^+	*exp*	*1.38*	*1.24*	*1.07*	*1.06*	*1.09*
	MC	*1.04*	*1.04*	*1.07*	*1.08*	*1.07*
K^+	*exp*	*1.35*	*1.28*	*1.08*	*1.10*	*1.07*
	MC	*1.01*	*1.05*	*1.06*	*1.05*	*1.06*
Rb^+	*exp*	*1.29*	*1.26*	*1.08*	*1.08*	*1.07*
	MC	*0.94*	*1.04*	*1.07*	*1.06*	*1.06*
Cs^+	*exp*	*1.19*	*1.18*	*1.07*	*1.08*	*1.07*
	MC	*0.92*	*1.02*	*1.08*	*1.08*	*1.04*

Note that for all the experimental data given in the table there is a pronounced effect of exceeding the ion mobility as compared with the polarization mobility. This effect is discussed in detail in many papers, and is usually associated with the competition between the attractive and repulsive parts of the interaction potential of an ion with an atom. A more detailed study of this effect will be given in a separate paper.

5. Approximation of mobility in a strong fields

To approximate the mobility of ions in a strong field, we use the Frost formula in the form (9). Based on the analysis of a large number of Monte Carlo calculations, it was found that the value of the parameter $(E/N)_{heating}$ can be very well approximated by the dependence on the same parameter ε_0 for that obtained for approximating the mobility in the weak field limit.

Let us find the dependence of the value of the parameter $b^{-1} = (E/N)_{heating}$ on gas temperature. From the analysis of drift velocity calculations using the Monte Carlo method, we assume that the approximation formula is:

$$1/b = (E/N)_0 \left(1 + 1.5 T_{atom}/\varepsilon_0\right). \qquad (11)$$

Here $(E/N)_0$ – is the value of the heating field at zero gas temperature. We introduce a new parameter

$$< \varepsilon >_{pol} = \frac{1}{2} m \left[1.5 (E/N)_0 K_{pol} N_0 / N\right]^2 \qquad (12)$$

this is the average energy of the directional motion of an ion in a field with a reduced intensity $1.5\,(E/N)_0$ at zero atomic temperature and polarization mobility of ions (3). With an accuracy of about 1%, the values of $<\varepsilon>_{pol}$ and ε_0 coincide, i.e. the parameter $(E/N)_0$ is not independent, but can be determined from the relation $<\varepsilon>_{pol}=\varepsilon_0$:

$$\left(\frac{E}{N}\right)_0 = \frac{(\varepsilon_0/2m)^{1/2}}{3K_{\text{pol}}N_0}. \qquad (13)$$

Slightly more complex than (11), the approximation of the form

$$1/b = (E/N)_0[\left(1+(1.5T_{atom}/\varepsilon_0\right)^{0.8}]^{1.2} \qquad (14)$$

gives a slightly better agreement with the results obtained from the analysis of the calculations of mobility by the Monte Carlo method. Tabl. 4 shows the values of the parameter ε_0, the polarization mobility K_{pol} and cross section parameters for alkali metal ions.

Table 4 – Parameter ε_0, the polarization mobility K_{pol} and cross section parameters for alkali metal ions

	ε_0, K	K_{pol} см^2/с В	$(E/N)_0$, Td	r_{gas}, 10^{-8} cm	$\sigma_{rez}(\varepsilon)$ 10^{-16} cm^2	b
Li	130	1,52	205,08	1,05	230,0	0,11
Na	110	0,83	188,65	2,234	260,0	0,11
K	100	0,48	239,32	2,77	350,0	0,10
Rb	410	0,31	497,63	2,48	247,0	0,024
Cs	370	0,23	533,37	2,68	295,0	0,025

Thus, we have the following approximation for the drift velocity:

$$u = \frac{K_{\text{pol}}N_0}{\left(1+T_{\text{atom}}/\varepsilon_0\right)^{1/2}}\left(1+\frac{3K_{\text{pol}}N_0}{\left(\varepsilon_0/2m\right)^{1/2}\left(1+1.5T_{\text{atom}}/\varepsilon_0\right)}\frac{E}{N}\right)^{-1/2}\frac{E}{N}. \qquad (15)$$

For the drift velocity, formula (15) gives values that almost coincide with the available experimental data [3-6].

6. Conclusion

The available experimental data are fragmented and cannot serve as a reliable basis for a comprehensive analysis of a wide variety of processes and phenomena in a gas-discharge plasma. Previously obtained approximations for the mobility of ions in parent vapors, given, for example, in the book [12], have a large error due to the fact that they are based on the assumption of the decisive influence of collisions with charge exchange.

In the present work, on the basis of the analysis of Monte Carlo calculations and comparing them with experimental data on the mobility of alkali metal ions in noble gases, we obtain approximation formulas for the mobility of alkali metal ions in parent vapors. The parameters found earlier for the approximation of the drift velocity of ions of noble gases are also given as a reference material. The parameters obtained in this work for the approximation of the mobility of alkali metal ions in parent vapors can be used to estimate the characteristics of a gas-discharge plasma.

The original purpose of the calculations was to demonstrate the paramount importance of the effect of gas temperature on the heating of ions under conditions of a cryogenic discharge, namely, in experiments with dusty plasma [6, 7]. But the results of calculations are much more general in nature, and in addition to cryogenic discharge can be used in the analysis of processes in gas-discharge plasma in installations of ion and plasma-chemical etching, deposition, sputtering in magnetron installations, in which the gas temperature can significantly exceed room temperature.

Generally speaking, the drift of ions in a gas discharge has a very significant effect on the

characteristics of a gas discharge. For example, a small fraction of mercury vapors in argon leads to a change in the ionic composition, a significant decrease in the electron temperature and a change in the radiative plasma characteristics [10].

The obtained parameters of the approximation of the drift rate of alkali metal ions in parent vapors can be used to estimate the characteristics of a gas-discharge plasma, when analyzing and planning experiments with dusty plasma under cryogenic discharge conditions, when considering discharge in a mixture of heavy and light gases [6, 7], when analyzing experiments with the scattering of ultracold ions into the surrounding gas. For the drift velocity, formula (10) gives values that almost coincide with the available experimental data [1–5, 16-22].

References

1 E.W. McDaniel, E. A.Mason. The mobility and diffusion of ions in gases – New York: Wiley – 1973.

2 H. W. Ellis, R. Y. Pai, E. W. McDaniel, E. A. Mason, L. A. Viehland. Transport properties of gaseous ions over a wide energy range. Part III // Atom. Data Nucl. Data Tabl. – 1976. –Vol. 17. – P. 177-210.

3 H. W. Ellis, E. W. McDaniel, D. L. Albritton, L. A. Viehland, S. L. Lin, E. A. Mason. Transport properties of gaseous ions over a wide energy range. Part II // Atom. Data Nucl. Data Tabl. – 1978. –Vol. 22. – P. 179-217.

4 H.W. Ellis, M.G. Thackston, E.W. Mc Daniel, E.A.Mason. Transport properties of gaseous ions over a wide energy range. Part III // Atom. Data Nucl. Data Tabl. – 1984. –Vol. 31. – P. 113-151.

5 L.A.Viehland et al. Transport properties of gaseous ions over a wide energy range, IV // Atom. Data Nucl. Data Tabl. – 1995. –Vol. 60. – P. 37-95.

6 S. A. Maiorov, T. S. Ramazanov, K. N. Dzhumagulova, A. N. Jumabekov, and M. K. Dosbolayev, Investigation of plasma-dust structures in He-Ar gas mixture // Physics of Plasmas – 2008. –Vol. 15. – P. 093701.

7 S. N. Antipov, É. I. Asinovski, A. V. Kirillin, S. A. Maiorov, V. V. Markovets, O. F. Petrov , V. E. Fortov, Evolution of Dust Structures from Room to Cryogenic Temperatures // Journal of Experimental and Theoretical Physics – 2008. –Vol.106 (4). – P. 830 – 837.

8 S. A. Maiorov. Ion drift in a gas in an external electric field // Plasma Phys. Rep. – 2009 –Vol. 35. – P. 802.

9 R. I. Golyatina, S. A. Maiorov. Approximation of the characteristics of ion drift in parent gas // Plasma Physics Reports. – 2017 – Vol. 43(1). – P. 75–82.

10 R. I. Golyatina, S. A. Maiorov. Characteristics of electron drift in an Ar-Hg mixture // Plasma Physics Reports. – 2018. – Vol. 44 (4). – P. 453–457.

11 R.I. Golyatina, S.A. Maiorov. Ion drift in parent gas for cesium, rubidium, and mercury // Physical Sciences and Technology – 2016. – Vol. 3, No. 2. - P. 12-19.

12 B.M. Smirnov. Ions and excited atoms in a plasma – Moscow: Atomizdat –1974.

13 R.I. Golyatina, S.A. Maiorov. Charging of a rodlike grain in plasma flow // Physical Sciences and Technology. 2017. - Vol. 4. -No. 2. – P. 4-14.

14 T. S. Ramazanov, S. K. Kodanova, N. Kh. Bastykova, and S. A. Maiorov, Investigation of hydrodynamic Properties of hot dense plasma // Phys. Wave Phenom. – 2018 – Vol. 26(4). – P. 327-333.

15 L. S. Frost. Effect of variable ionic mobility on ambipolar diffusion // Phys. Rev. – 1957. – Vol.105. – P. 354.

16 P.H. Larsen, M.T. Elford. The mobilities of xenon ions in xenon and the derived charge transfer cross section for Xe+(2P3/2) ions in xenon // Journal of Physics B: Atomic and Molecular Physics. – 1986. – Vol. 19(4). – P. 449.

17 S. A. Khrapak. Practical expression for an effective ion-neutral collision frequency in flowing plasmas of some noble gases // J. Plasma Phys. – 2013. – Vol. 79 – P. 1123.

18 Z. Ristivojevic, Z. L. Petrović. Axial light emission and Ar metastable densities in a parallel plate dc microdischarge in the steady state and transient regimes // Plasma Sources Sci. Technol. – 2012. – Vol. 21. – P. 035001.

19 J. B. Hasted. Physics of atomic collisions – London: Butterworths – 1964.

20 E. W. McDaniel. Collision Phenomena in ionized gases – New York: Wiley – 1964.

21 T. Dote, M. Shimada. Derivation of modified frost formula for drift velocity and swarm characteristics of positive ions in their parent rare gases // J. Phys. Soc. Jpn. – 1992.– Vol. 61. – P. 4009.

22 H. Wang, I.D. Kaganovich, V.S. Sukhomlinov, A.S Mustafaev. Simulations of ion velocity distribution functions taking into account both elastic and charge exchange collisions // Plasma Sources Science and Technology. – 2017.– Vol. 26 (2). – P. 024002.